universität wien

MASTERARBEIT / MASTER'S THESIS

Titel der Masterarbeit / Title of the Master's Thesis

„Field- and microscopic investigation of iron oxide and calcite coated fractures in glauconitic sandstones, quarry Strombauamt, Greifenstein, Lower Austria“

verfasst von / submitted by

Lisa Maria Rücklinger, BSc

angestrebter akademischer Grad / in partial fulfilment of the requirements for the degree of

Master of Science (MSc)

Wien, 2021 / Vienna 2021

Studienkennzahl lt. Studienblatt / degree programme code as it appears on the student record sheet:	A 066 815
Studienrichtung lt. Studienblatt / degree programme as it appears on the student record sheet:	Masterstudium Erdwissenschaften
Betreut von / Supervisor:	ao. Univ.-Prof. Mag. Dr. Susanne Gier
Mitbetreut von / Co-Supervisor:	Dr. Kurt Decker

Diese Arbeit wurde außerdem mitbetreut von Mag. Dr.rer.nat. Stephanie Neuhuber, Universität für Bodenkultur, Wien. // This work was also co-supervised by Mag. Dr.rer.nat. Stephanie Neuhuber, University of Natural Resources and Life Sciences, Vienna.

Ich habe mich bemüht, sämtliche Inhaber der Bildrechte ausfindig zu machen und ihre Zustimmung zur Verwendung der Bilder in dieser Arbeit eingeholt. Sollte dennoch eine Urheberrechtsverletzung bekannt werden, ersuche ich um Meldung bei mir.

INDEX

ACKNOWLEDGEMENTS

This part is composed in German, because I want all my loved ones to be able to read it.

Die zugegebenermaßen mehr als drei Jahre, in denen diese Masterarbeit entstanden ist, waren bestimmt die herausforderndsten meines noch jungen, aber immerhin schon fast drei Jahrzehnte dauernden Lebens. Ich durfte erfahren, was es heißt, an seine mentalen und psychischen Grenzen zu kommen, mal ziemlich neben sich zu stehen und nicht wirklich voranzukommen. Ich durfte aber auch erfahren, was es heißt, auf sich selbst Acht zu geben, ehrlich zu sich zu sein, dass das Leben sich oft wie Puzzleteile zusammenfügt und vor allem, was es heißt, wenn Menschen in so einer Zeit zu einem stehen und für einen da sind. Auf diesem Wege möchte ich allen dafür danken, insbesondere den Menschen, die mir dabei geholfen haben, diese Masterarbeit zu Papier zu bringen.

Allen voran danke ich natürlich meinen Betreuern, Susi, Kurt und Stephanie, die mit viel Geduld und Zuspruch, guter Expertise und wissenschaftlichem Rat zum Gelingen dieser Arbeit beigetragen haben. Weiters bedanke ich mich bei allen anderen Professoren und Studienkollegen unseres Instituts für alle Gespräche, Tipps und Ratschläge rund um meine Diplomarbeit oder auch für die Hilfe bei der Benutzung diverser Geräte in Laboren. Besonderer Dank gilt auch Richard Worden (University of Liverpool) für seine Ideen zur Entstehung der Eisenkruste. Unzählige Stunden verbrachte ich vor dem Rasterelektronenmikroskop. Hier gilt ein herzlicher Dank Herrn Prof. Baal und Hugh Rice für die Expertise bei der Benutzung des Geräts.

Der Steinbruch Strombauamt, um den sich meine Arbeit dreht, ist im Besitz der Firma *Erdbau Karner GmbH*. Dass wir den Steinbruch immer ohne weiteres betreten durften, ist für mich keine Selbstverständlichkeit und dafür möchte ich mich herzlichst bei der Fa. Karner bedanken!

Besonders meine Familie stand in dieser Zeit immer hinter mir, sie gaben mir die Zeit, die ich hierfür brauchte und das ohne jeden Vorwurf. Dafür bin ich wirklich dankbar. DANKE Mama, Papa, Doris und Mario! Danke auch all meinen großartigen Freunden!

Abschließend möchte ich mich auch noch bei meiner Psychotherapeutin bedanken. Ohne sie hätte ich diese Masterarbeit bestimmt noch nicht abgeschlossen. Psychotherapie ist ja nichts anderes als Hilfe zur Selbsthilfe. Und deshalb möchte ich diese Arbeit auch dem Thema der psychischen Gesundheit widmen und gern dazu beitragen, dass psychische Probleme und Psychotherapie ein bisschen enttabuisiert werden. Weil es völlig ok ist, wenn es einem Mal nicht gut geht und man Hilfe braucht.

ABSTRACT

In the quarry *"Strombauamt"* at Greifenstein, Lower Austria, iron oxide coatings occur on structural discontinuities in massive sandstones. The mineralogy, chemical composition and (micro-) structures were analysed to assess the origin and formation mechanism of these crusts. The sandstone belongs to the Greifenstein Formation of the Rhenodanubic Flysch Zone and was deposited during the Upper Palaeocene to Lower Eocene. The iron crust bearing beds are up to 10 m thick massive sandstones of a channel fill in a classical turbidite succession. Since these sandstones are outcrop analogues of hydrocarbon reservoir rocks in the subcrop of the Vienna Basin, their impact on reducing permeability was investigated.

A 250 m E-W section at the southern wall of the quarry exposes the deposits, which are partly dissected by faults. Some of the faults are encrusted with iron oxides. The red to orange crusts are prominent features within the thick-bedded (1 m - 10 m) sandstones at the base of the southern wall, but do not continue into the overlying thin-bedded sandstones. Occasionally, the crust is covered by synkinematic calcite fibres that formed on the fault planes, and/or idiomorphic calcite and quartz. Structural evidence indicates that at least some of the iron precipitates formed on deformation bands, which only form soon after sediment deposition in yet unlithified deposits. The iron crust appears on all occurring fracture sets.

The sandstones are glauconite-rich quartz arenites, with some beds cemented by calcite. X-ray diffraction used to determine the mineralogical composition of the crust identifies mainly quartz, K-feldspar, calcite, muscovite, glauconite and traces of goethite as evidence of a *"crust-building"* iron mineral. The iron coating that encrusts some joints affects the outermost 0.5mm up to 5mm of the sandstone, forming a macroscopically distinct red zone. SEM microscopy combined with EDAX shows that the iron mineral is an iron oxide that either forms thin coatings around most of the grains or crosscuts through minerals in the form of veins. Broken grains that are later cemented by the iron oxide also show evidence of tectonic influence.

Based on the present results, it is concluded that iron-rich fluids that filled the fractures in the compacted sediment induced the precipitation of iron oxide on grain boundaries, possibly twice. Some of these fractures were later filled with secondary calcite, indicating shear along the fractures. The source of iron can either be external or from within the sandstone itself. Although the sandstone contains abundant glauconite and some pyrite, an external source is more likely. The lower conglomerates of the quarry revealed iron-rich rip-ups and intercalations of autochthonous sediments. Their iron-red rims make them likely sources of iron. Nonetheless, another external source, such as iron-bearing minerals from underlying formations, could also be considered possible sources.

1. Introduction

The sandstones of the quarry "*Strombauamt*" in Greifenstein, Lower Austria, are the type locality of the Greifenstein Formation, a part of the Rhenodanubian Flysch Zone (RFZ). The Lower Palaeocene to Middle Eocene quartz sandstones represent good outcrop analogues for hydrocarbon reservoirs in the Vienna Basin. During fieldwork for an OMV Project about Flysch in the Vienna Basin, iron oxide coatings on structural discontinuity planes of massive sandstone beds were found. Since these sandstones are important reservoir rocks in the Vienna Basin, the origin of the iron crusts and their impact on the reduction of permeability was of interest and investigated in this study.

Besada (1996) described a profile of the quarry in detail. He reported on iron oxides in the groundmass and around clay clasts occurring on the *"psephites"* (=conglomerates) and *"psammites"* (=sandstones) in the quarry. He found limonite grain coatings around glauconites in sandstones. Red brown colours on fractures and weathering surfaces on sandstones and/or in the middle section are described.

There are published examples of the occurrence of various iron mineral precipitates on clastic sedimentary rocks from all over the world. Several studies of iron concretions of different sites of the aeolian Navajo Sandstone in south-eastern Utah have been made. Early diagenetic hematite grain coatings were dissolved by reducing fluids: there, the sandstone was bleached, and iron oxides were precipitated when the fluids came into contact with oxidizing (meteoric) waters (e.g., Chan, et al., 2000; Beitler, et al., 2005; Eichhubl, et al., 2009; Potter-McIntryre, et al., 2013). Similar processes occurred in the case of the Aztec Sandstone, Valley of Fire, Nevada (Eichhubl, et al., 2004).

The continen tal to shallow marine deposits of the Bahariya Formation in the Western Desert of Egypt show abundant ironstone crusts. The sandstone and shale sequences are separated by cm-thick concretionary iron stone (goethite and hematite) horizons. A complex diagenetic history and the presence of reducing fluids, which dissolved iron from the basement rocks, account for these concretions (Afify, et al., 2014).

Another example of *"iron oxide deposits*" can be found in the Paraíba Basin, Brazil, where poorly lithified sandstones bear structurally-driven iron impregnations, concretions and mineral masses that formed along interfaces between fault cores and mixed zones due to diffusion of pore-water-oxygen into advective iron-rich fluids (Balsamo, et al., 2013). One last example consists of lens-shaped hematite and goethite concretions in the Härma Beds, Estonia. They are thought to be of diagenetic origin and were most probably precipitated

from iron-rich groundwater migrating along bedding planes and joints (Shogenova, et al., 2009).

1.1. Rationale/Research Questions

The iron crusts of the *"Strombauamt"* are a unique feature found only in the Greifenstein area of the Rhenodanubian Flysch Zone. They were investigated in detail in the field and laboratory to determine

(1) the mineralogical, chemical and petrographic properties of the iron precipitates;
(2) the history of sandstone and iron crust formation, sequence of cementation and fracturing within the sandstones;
(3) the history of fluid flow;
(4) the origin of the iron crust and/or source of iron rich fluids;
(5) the effects of iron crusts on permeability, porosity and other rock features such as chemistry and texture.

2. Geology and outcrop

2.1. Geological overview

The investigated quarry (the *"Strombauamt"* in Greifenstein) is located north-northwest of Vienna and belongs to the Rhenodanubian Flysch Zone (RFZ). The sediments of the quarry represent the type locality of the Greifenstein Formation, which is part of the Greifenstein Nappe, one of the tectonic units of the "*Wienerwald Flysch*". Hösch (1985), Besada (1996), Faupl (1996) and Wessely (2006), as well as some other authors, have already given a detailed geological description of the location. The RFZ is part of the Penninic tectonic units and makes up the northern part of the Eastern Alps. It extends in a narrow belt for about 500 km from Vorarlberg in the West to Vienna in the East, where it continues beneath Neogene sediments of the Vienna Basin into the Carpathians (Fig. 1).

From the Jurassic to the Paleogene, the Penninic Ocean extended from the Atlantic towards the East. Sediments deposited in this ocean later formed the Penninic units. Terrigenous clastic sediments periodically collapsed and slipped down continental slopes as turbidity currents or other gravitational mass flows (= resedimentation or *"mass-gravity"* transport) and were partly deposited below the calcite compensation depth (CCD) in about 3500-5000m (Faupl, 1996). They appear today, overprinted by the alpine orogeny, as the flysch sediments of the RFZ. In the Wienerwald region, where it has its widest N-S extent (about 20 km), the RFZ is subdivided into four Nappes (Fig. 2), from bottom to top:

(6) Northern Margin Zone

(7) Greifenstein Nappe

(8) Laab Nappe

(9) Kahlenberg Nappe

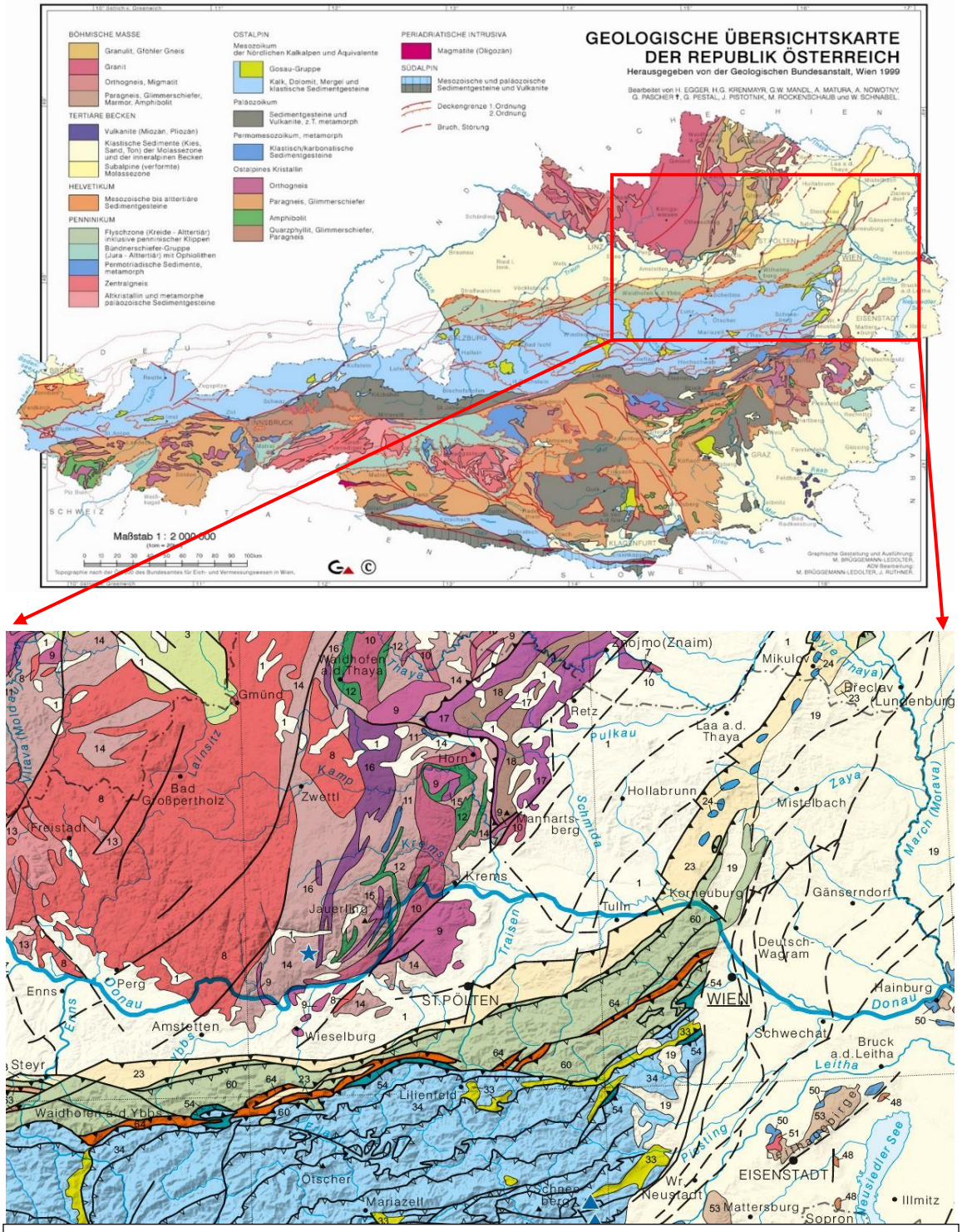

Fig. 1 Map of the Geology of Austria (Egger, et al., 1999), the red box marks the area around Vienna and shows the Flysch Zone of the Wienerwald area (in green) (cut-out of the Poster map *"Geologie von Österreich"*, (Schuster, et al., 2013))

The paleogeographic position of each unit has been debated in the past, and several interpretations are given by different authors:

However, Egger (2013) proposed to drop the concept of the Kahlenberg Nappe and interpreted this nappe as a southern imbricate of the Greifenstein Nappe, as there are no big thrust distances. This was a result of the project *"Mapping the northern rim of the Eastern Alps"*, which investigates in more detail the geological and structural relationship of the nappes and sequences of the RFZ.

Apatite fission-track data indicate that the Kahlenberg- and Laab Nappes were buried beneath the apatite partial annealing zone between at least 6km and less than 11km. Exhumation was initiated during the Late Oligocene to Early Miocene. The Greifenstein Nappe underwent a different thermal history, only reached the apatite partial annealing zone (~100°C and 5-6km deep), and exhumation started in the early to middle Miocene. A paleogeographic reconstruction asserts that the Kahlenberg and Laab Nappes were positioned on top of the Greifenstein Nappe by an out-of-sequence thrust (Trautwein, et al., 2001).

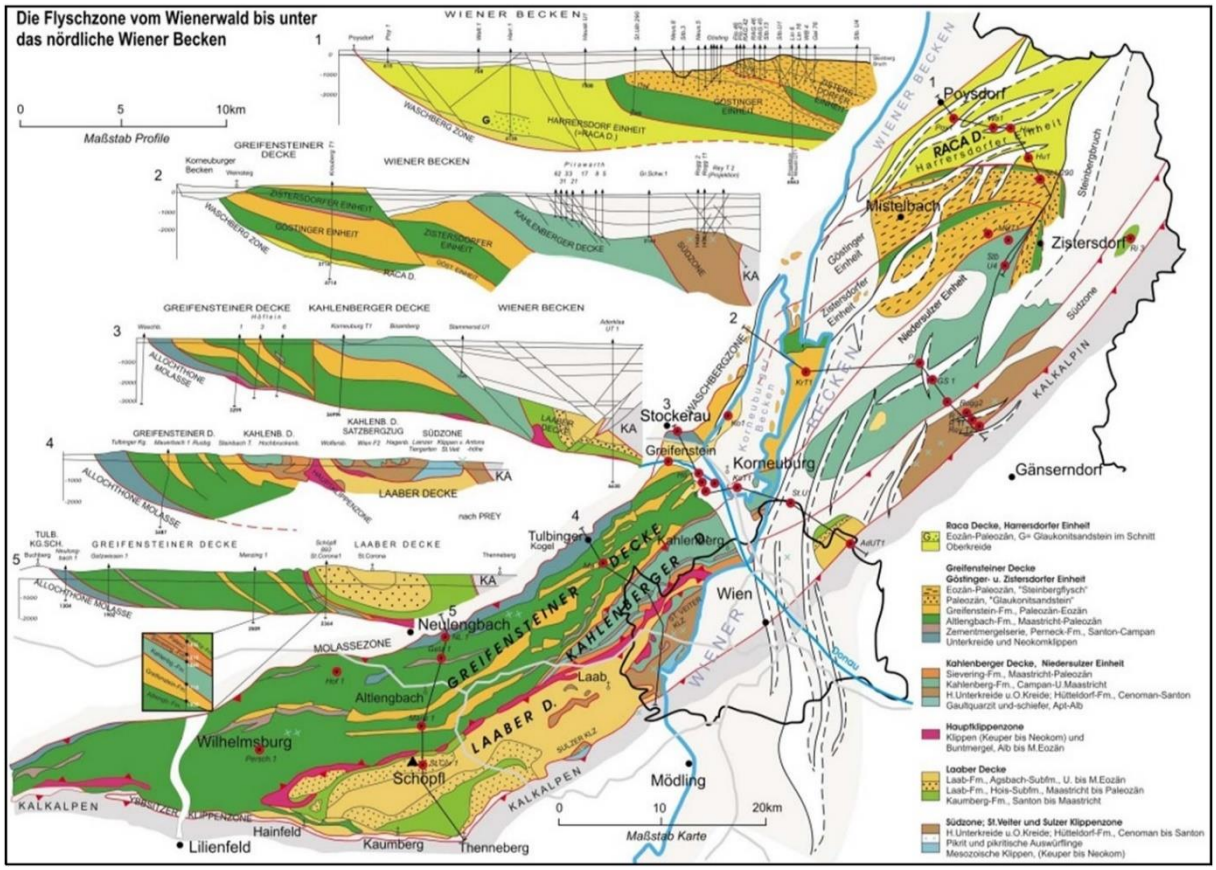

Fig. 2 A detailed map and cross sections of the RFZ in the Wienerwald area and the subcrop of the Vienna basin. Section 3 shows the situation around Greifenstein. (Wessely, 2006)

2.1.1. The Greifenstein Nappe

As the rocks of the quarry belong to the Greifenstein Nappe, this unit is explained in more detail.

Sediments of the Greifenstein Nappe are of (Late) Cretaceous to middle Eocene age. Within the Greifenstein Nappe, there are four main lithostratigraphic units, from bottom to top:

(1) The Röthenbach Subgroup, which was newly defined by Egger & Schwerd (2008). Formerly known as the *"Zementmergelserie"*, the Subgroup ranges stratigraphically from the Coniacian to the Campanian. It contains sandy limestones, grey to pale marls and claystones that were formed by distal turbidity currents.
(2) The Perneck Formation (*"Oberste Bunte Schiefer"*) was deposited in the Late Campanian and is characterized by thinly-bedded shales and siltstones and red hemipelagic claystones (Wessely, 2006).
(3) The Altlengbach Formation (Maastrichtian to Palaeocene) is described as siliciclastic-rich flysch. It contains thick-bedded quartz- and mica-rich sandstones that characteristically show *"crumbly"* weathering due to their high clay concentration (*"Mürbsandsteine"*) (Egger, 1995).
(4) The Greifenstein Formation, which is the uppermost and youngest unit, ranges from the late Palaeocene to the middle Eocene and consists of glauconite-rich flysch sediments, i.e., conglomerates, sandstones, and mudstones. This unit is described in detail in the next chapter.

2.1.2. The Greifenstein Formation

The Greifenstein Formation extends from Traisen to Klosterneuburg in Lower Austria and was deposited from the Palaeocene to the middle Eocene (Fig. 2). It is the northernmost and most proximal formation within the Greifenstein Nappe and was deposited on the upper part of a deep-water fan.

It was divided into three main lithofacies by Hösch (1985):

(5) Graded and ungraded conglomerates with an average bed thickness of more than ten metres, which can be classified as clast-supported conglomerates after Walker (1978). They are only present in the northern most section of this formation and represent channel-fill deposits.
(6) Massive sandstones without grading. They bear clay clasts and make up more than 50% of the Greifenstein Formation, also representing channel-fill deposits.

(7) Classic turbidites. The interchannel sediments consist of conglomeratic sandstones, sandstones and claystones deposited in a partially incomplete Bouma (1962) cycle.

The rocks of the Greifenstein Formation contain a considerable amount of glauconite that gives the sandstones a typical greenish colour and is eponymous for the formation's name in the underground of the Vienna Basin: Glauconite Sandstone Series.

2.2. The quarry *"Strombauamt"*

2.2.1. Background information

The investigated quarry is located on the southern side of the Danube in the municipal area of St. Andrä-Wördern, village Greifenstein, near the city of Klosterneuburg. The coordinates are 48.35° northern latitude and 16.25° eastern longitude.

The sandstones enjoyed great popularity as a construction material (e.g., for buildings in Vienna) in recent centuries and were mined in several quarries around Greifenstein. The biggest and longest operating quarry serves as the focus of this study, formerly known as the *"Hollitzer-Steinbruch"*. In the previous century, the quarry was tightly linked to river engineering (in German: *"Strombau"*), in particular for the regulation of the Danube river. After the quarry was nationalized in 1927, it was renamed *"Strombauleitung Greifenstein"* (Heilinger, et al., 2006). Due to its history and its location near the former administrative building for *"Strombau"*, the *"Strombauamt"* (nowadays used as an event location), the quarry is commonly referred to as *"Strombauamt"* (e.g., in scientific work).

After a long history of quarry work, mining was stopped in 1993. The quarry was bought by the *"Erdbau Karner GmbH"* in 2000 (source: http://www.karner-gmbh.at/). As of today, the quarry is still used as a landfill: the area serves as a deposit for excavated soil and is being recultivated. Subsequently, the outcrops are constantly changing. This can be both an advantage and a disadvantage. Some locations investigated in this study are no longer exposed, while at the same time new parts of the rock face are now accessible.

2.2.2. Lithology

Hösch (1985) and Besada (1996) have undertaken a thorough description of the lithologies of the quarry *"Strombauamt"* and have created a detailed, continuous profile. Further investigations concerning the reservoir properties of the rock were undertaken by Löffler (2013).

When Besada investigated the quarry in 1996, a section of about 120m (vertically) was exposed, and the face extended about 200m in a semicircle. Grain sizes and bed thicknesses generally decrease from bottom to top (fining and thinning upwards). Besada (1996) described an overall section of the quarry, which was divided in three parts, with conglomerates at the bottom, thick, lenticular shaped, massive sandstone beds in the middle and thinner, alternating beds of sandstones and pelites on top of the section.

The thick conglomerates of the lower section are generally clast-supported and show an even bedding, with amalgamation planes and grain orientation. The massive sandstones of the middle section are not graded and are of medium to coarse grain size. Its thick-bedded, grey-green, yellow-brown, weathered quartz sandstone is the type rock of the Greifenstein Formation. The lower sections of some beds are conglomeratic sandstones. Thinner beds of up to 1 metre can be classified as classical turbidites after Bouma (1962). The lithologies of the hanging section are finely-grained, thinly-bedded turbiditic sandstones.

Löffler (2013) logged the freshly exposed eastern wall and re-visited Besada's south face.

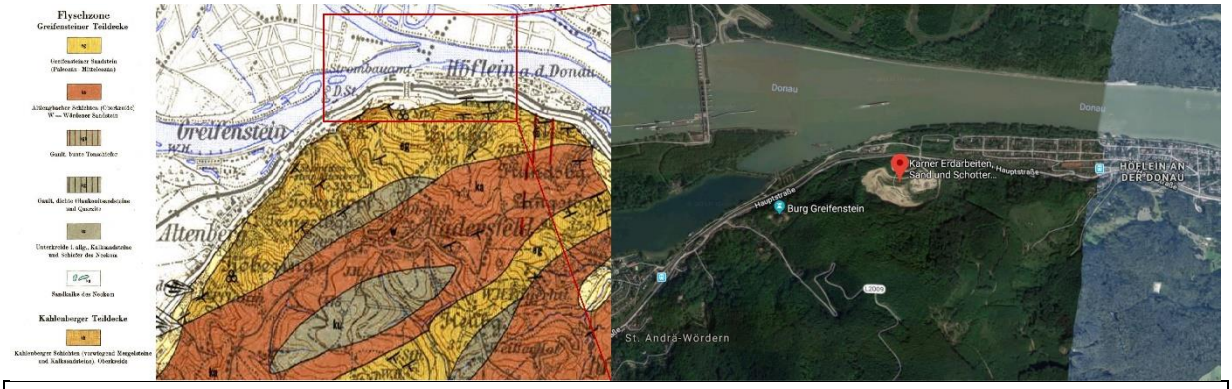

Fig. 3 Left: Geological Map of the Greifenstein area, part of the "Geologische Karte der Umgebung von Korneuburg-Stockerau 1:50.000" (Grill, et al., 1957), source: GBA-Website. The red box indicates the area of the map on the right side, the quarry "Strombauamt" is marked. (source: maps.google.at)

3. Materials and Methods

3.1. Field work and samples

Five separate days (07/2017, 10/2017, 06/2018, 10/2018 and 06/2019) were spent in the quarry *"Strombauamt"* to examine the structural and sedimentological features of the outcrops with iron-encrusted sandstones and to collect samples for further investigations (described in 3.2ff). On the first three visits, the so-called *"south wall"* (Besada, 1996) was investigated, and structures were logged/mapped. Seven samples were collected. The fourth and fifth visits were used to map and record structures of the south wall and a newly accessible western part of the quarry, here called the *"southwest wall"*. Nineteen samples were collected: 5 from the south wall and 14 from the southwest wall (Fig. 4, Table 3).

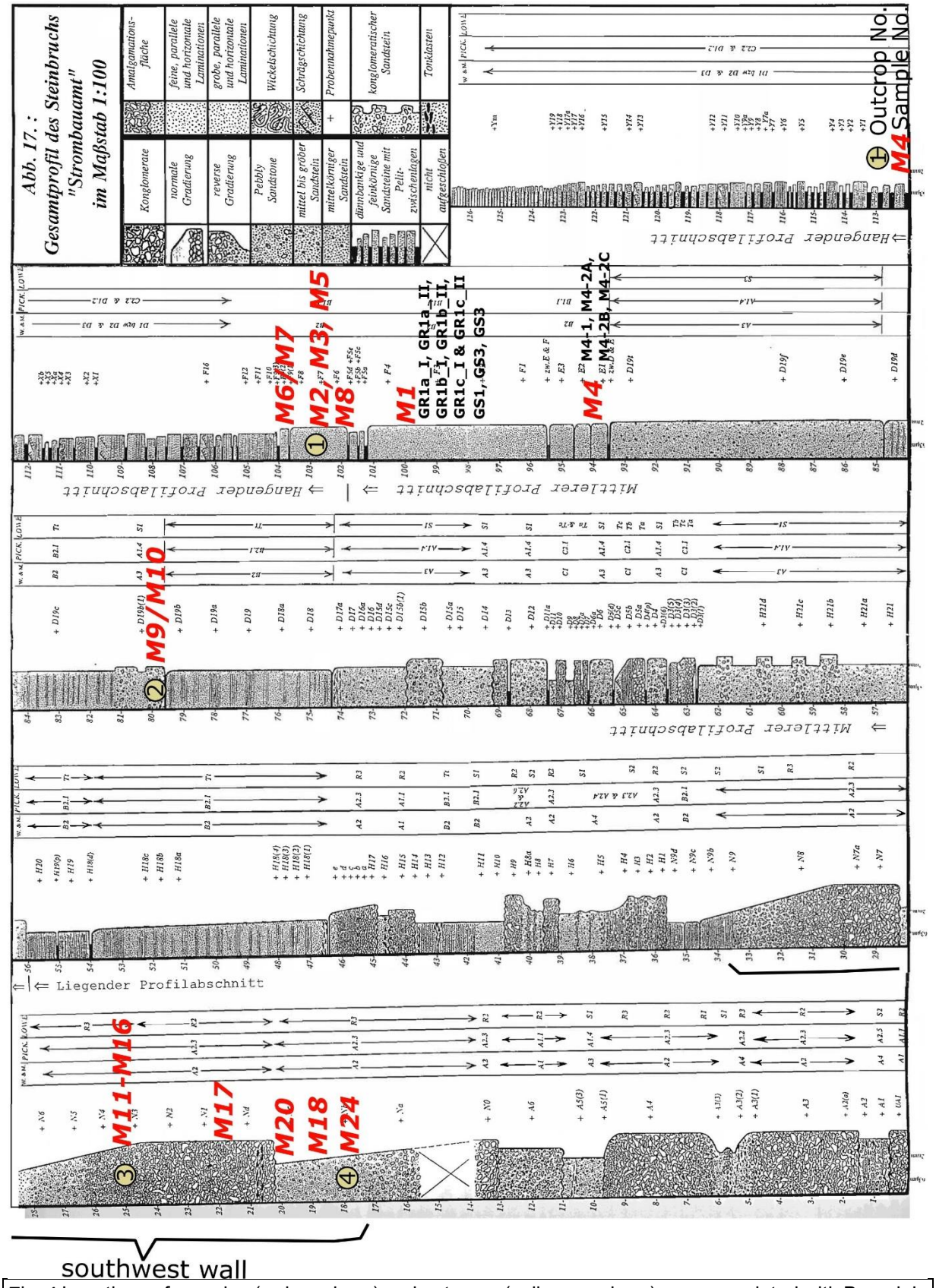

Fig. 4 Locations of samples (red numbers) and outcrops (yellow numbers) were correlated with Besada's (1996) profile. Numbers of thin sections and plugs, if different from the hand samples, are written below sample numbers in black. Samples M1 to M10 were located at the upper part of the middle profile section, with the uppermost samples even being part of the upper section. Samples M11 to M24 are part of the middle lower section containing massive, graded conglomerates.

3.2. Sandstone analyses

The samples were analysed with various petrographic methods for characterization of the sandstones. Sedimentological and structural features like colour, grainsize, sorting, lamination and lineation were determined macroscopically with the samples and in the field. For microscopic analyses, thin sections were made from samples M1 to M4, M8 and M10, which are iron-encrusted sandstones and a conglomeratic sandstone. If the thin section was made of an area with iron crust, it was taken perpendicular to the crust. The ones that were used for SEM or CL were coated with carbon for better conductivity. Samples M6 to M24 were powdered to determine their mineralogical and chemical composition. Encrusted and non-encrusted sandstones, conglomerates, silty sandstones and claystones were selected. A list of samples is found in the Appendix.

3.2.1. Transmitted-light microscopy (TLM)

A *"Nikon Optiphot 2-Pol"* (Fig. 5) transmitted-light microscope was used for mineralogical investigation of the iron-encrusted sandstones. Pictures were taken with the program LAS (Leica Application Suite) version 4.9.0 and the *"Leica DM4500P"* transmitted-light microscope. As there already are data about these sandstones from prior work (see Besada 1996, Löffler 2013), these data were only verified; and no further investigations concerning sandstone classification were carried out.

Fig. 5 *"Nikon Optiphot 2-Pol"* transmitted-light microscope and thin sections of samples M1, M2, M3, M4, M8 and M10

3.2.2. Scanning Electron Microscopy (SEM)

Pictures with 50 to 2000 times magnification and information on the bulk chemical composition of single grains were obtained with a scanning electron microscope (SEM). This allowed for the study of microstructures and cementation at a much higher resolution. Carbon-coated thin sections (30 micrometres thick) were analysed with an electron beam using the *"FEI Inspect S"* SEM (Fig. 6) at the Department of Geology (UZA 2, University of Vienna). The *"FEI Inspect S"* uses a tungsten hairpin electron gun. Images can be produced by a secondary electron (SE) and a backscattered electron (BSE) detector. For this work, the backscattered electron (BSE) detector was used, which allows Z-contrast imaging (distinction and spatial distribution of mineral phases) and imaging of 2D microstructures. For optimal resolution, a voltage of 10

kV and spot size 7 was used. For chemical analyses with EDX, a voltage of 15 kV was used (cf. chapter 3.3.1).

Fig. 6 Photos of the *"FEI Inspect S"*
SEM at the Department of Geology. Left: opened sample chamber with a fixed thin section on the sample table. Right: SEM and monitor.

3.2.3. X-ray diffraction (XRD)

The mineral composition of powdered samples was obtained by way of X-ray diffraction (XRD). Analysis was carried out with the *"Panalytical PW 3040/60 X'Pert PRO"* X-ray diffractometer (CuKα radiation, 40 kV, 40 mA, step scan, step size 0.02°, 5s per step) at the Department of Geology (Fig. 7). The programs *"X'Pert Data Viewer"* (Version 1.2f) and *"X'Pert HighScore Plus"* (Version 2.2e) were used for interpretation. The diffractograms were interpreted according to Moore and Reynolds (1997).

XRD peaks are produced by constructive interference of a monochromatic beam of X-rays scattered at specific angles (2θ angles referring to Bragg's law) from each set of lattice planes in a sample. The peak intensities are determined by the distribution of atoms within the lattice. The interaction of the incident rays with the sample produces constructive interference (and a diffracted ray) when conditions satisfy Bragg's law:

$$n\lambda = 2\,d\,sin\,\theta \qquad \text{Eq. 1}$$

Fig. 7 The *"Panalytical PW 3040/60 X'Pert PRO"* XRD at the Department of Geology

Conversion of the diffraction peaks to d-spacings allows identification of the compound because each compound has a set of unique d-spacings (Bunaciu, et al., 2015).

3.2.4. Cathodoluminescence (CL)

Cathodoluminescence was mainly used to distinguish the calcite cements. For this method, carbon-coated thin sections (15 micrometres thick, polished) were analysed with the Cathodoluminescence microscope *"HC5-LM"* model at the Department of Geology.

A vacuum of approximately 1^{-4} kbar and 0.2 mA are obligatory for this analysis. The *"HC5-LM"* is capable of transmitted light, polarized transmitted light and cathodoluminescence photography with the programme Kappa Camera Control.

CL occurs when a crystal is bombarded by a stream of high-energy electrons. Excited electrons that were elevated into the conductive band (higher energy) may get shortly trapped because of structural defects or impurities when returning to the valence band (low energy), and the lost energy when leaving the trap may result in luminescence. Thus, CL provides general information on the trace elements contained in minerals or defects in the crystals. This can be used for, e.g., recognition of zonation of crystals or provenance analysis of sandstones and diagenesis of both siliciclastic and carbonate sediments (Boggs & Krinsley, 2006).

3.3. Element analysis

3.3.1. Energy dispersive X-ray spectroscopy (EDX)

Energy dispersive X-ray spectroscopy (EDX) was used for chemical analysis of minerals in combination with SEM. The software *"Genesis Spectrum"* (Version 6.34) from the company EDAX Inc. was used for EDX measurements and interpretation on spot, as well as on area size (mapping).

EDX measures the intensity and energy of x-ray lines that are emitted from the specimen due to excitation mostly by high-energy electrons. The energies of the lines are characteristic for specific elements, while the intensities are related to the element concentrations. (Goldstein, et al., 2003)

3.3.2. Electron micro probe (EMP)

The model *"Cameca SX Five Fe"* electron micro probe from Ametek Material analysis division at the Department of Lithospheric Research was used for analysis. It has BSE & SE detectors, an absorption spectrometer, a reflected and a transmitted light camera. Two samples fit in the machine. They are analysed by an electron beam (15 kV and 20 nA) in a vacuum chamber.

Four of the thin sections also used for SEM (30-35 micrometre thick and carbon-coated) were analysed. At first, a dolomite-standard was measured for calibration. Results are reported in oxide %. Beam size at each measurement point was 1 micrometre, 6 micrometres when glauconite and 8 micrometres when calcite was measured.

The electron microprobe was used to assess the chemical composition of calcite cements, calcite fibres, glauconites (in *"iron-encrusted area"* vs. in the *"host rock"*) and iron oxides.

3.4. Porosity and Permeability

Since the sandstones of the quarry *"Strombauamt"* are outcrop analogues of hydrocarbon reservoir rocks in the sub crop of the Vienna Basin, the porosity and permeability of a sample with and without iron crust was measured for comparison.

The measurements were made with the automated Gas-Permeameter-Porosimeter *"Coreval 700"* from the French company *"Vinci Technologies"* at the Department of Geology (Fig. 8). The device is equipped with a data acquisition software and calculating computer station. It can measure and calculate the properties of a cylindrical test specimen, so-called plugs, under different confining pressure conditions. Using N_2 gas, different confining pressures can be applied at the Coreval 700, starting at 400 Psi (pounds per square inch, 1 Psi = 0.0689476 bar) up to 10,000 Psi (689.476 bar) and back to get an idea of the samples' compressibility behaviour. Plugs drilled for measurements must have a standard diameter of 38.1mm (1.5 inches) and a length between 26mm and 76mm (Penz-Wolfmayr, 2018).

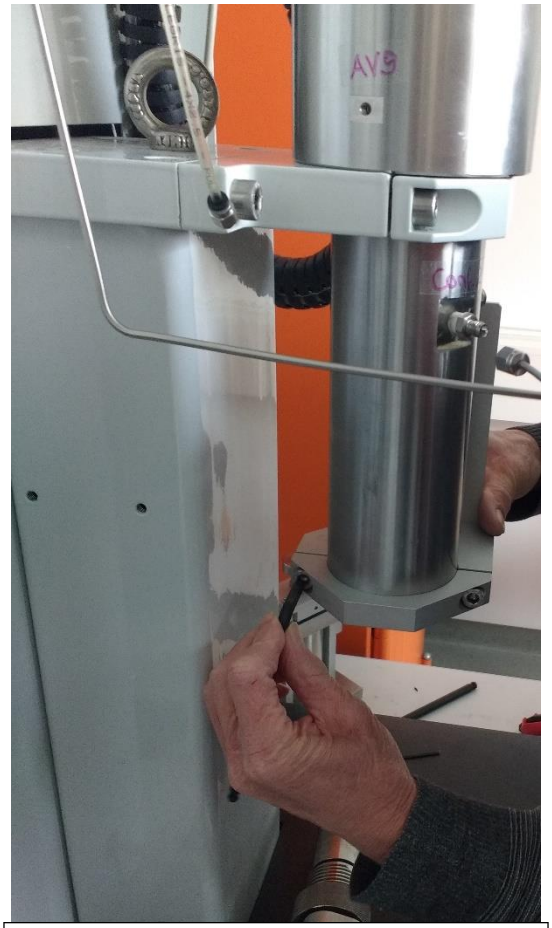

Fig. 8 The Gas-Permeameter-Porosimeter *"Coreval 700"* at the Department of Geology

Three plugs were drilled out of sample M1 at the Department of Geology and given the name GS1, GS2 and GS3 (with GS standing for Greifenstein).

A detailed description of the *"Coreval 700"* and how calculation works is found in the thesis of Penz-Wolfmayr (2018) and in the device's user manual.

3.4.1. Porosity

Cone and Kersey (1992) define porosity as the ratio of void space (pore volume) to bulk volume and report it either as a fraction or a percentage. Total porosity includes all void space regardless of whether the pores are interconnected or isolated. Effective porosity includes just the void spaces of interconnected pores.

The *"Coreval 700"* calculates porosity using the ideal gas law and other physical/ mathematical relations with the following equations:

Total Porosity

The total porosity considers isolated as well as open (in sense of fluid transport and storage) pores and can be calculated by dividing the total pore volume by the bulk volume:

$$pr = \frac{T_P V}{vb} \qquad \text{Eq. 2}$$

Open Porosity

The open porosity, which considers only those pores where fluid transport is possible, is calculated by dividing only the effective pore volume by the bulk volume:

$$pe = \frac{Pve}{vb} \qquad \text{Eq. 3}$$

(Penz-Wolfmayr, 2018: page 31)

3.4.2. Permeability

Permeability is a property of porous media that characterizes the ease with which fluid can flow through the media in response to an applied pressure gradient. It is a measure of fluid conductivity of porous material (Ohen & Kersey, 1992: page 210).

The SI-Unit of permeability is m², but Darcy (D) or Millidarcy (mD) are more commonly used ($1D=9.86923*10^{-13}$ m²).

The basis for permeability calculation is Darcy's law:

$$q = KA\frac{\Delta h}{L} \qquad \text{Eq. 4}$$

(Penz-Wolfmayr, 2018)

4. Results

4.1. Outcrop sedimentology and structural geology

Two walls in the quarry *"Strombauamt"* were investigated in detail (Fig. 9). The south wall and the southwest wall.

Fig. 9 Satellite image of the quarry taken in summer 2019. Outcrops are marked and labelled. The south wall and the southwest wall were investigated in this work. The locations of structural investigations are marked with numbers.

The south wall exposed sandstone beds of over approximately 30m height and 120m width in June 2019 (Fig. 10). In the middle and at the bottom of the outcrop are massive sandstone beds with thicknesses of up to eight metres, sometimes interbedded with silt-/mudstone or not fully lithified sandy to silty layers. These beds correspond to the middle section of Besada's profile (Fig. 4). The rocks are finely-grained to conglomeratic sandstones of a light grey to middle grey colour, which can be classified as glauconite bearing quartz arenites (Besada, 1996). The glauconites give the rocks a greenish complexion. Beds are stained a reddish colour due to glauconite (iron) oxidation during weathering and abundant iron crusts that appear on the fracture surfaces in this sequence. These are the crusts investigated in this work. They are described in detail in chapters 4.1.1 and 4.2. The massive sandstone beds show classical sedimentary structures of deep-marine mass flows like cross-stratification, amalgamation, normal-grading or BOUMA-sequences. Small rip-up-clasts of clay occur infrequently.

The top layers of this wall consist of thinner sandstone layers (Fig. 10). They make up the upper part of the quarry wall as described in Besada (1996). As far as observable, they show

no iron crusts. Outcrop conditions, however, prevented detailed analyses of this thin-bedded succession.

Fig. 10 The south wall in June 2018. The locations of outcrops from which structural data were acquired are marked with numbers. See Fig. 9 for location.

To the west and to the bottom of the south wall, other lithologies are exposed *("southwest wall",* Fig. 11). This section forms the stratigraphic continuation below the sandstones described above. It extends 30 metres from southeast to northwest and approximately 20 metres high and consists of conglomerate beds. Correlated with Besada's profile (Fig. 4), the outcropped wall resembles beds from metre 17 to metre 34. Beds have a thickness of about 3 to 5m and are not always delimited by clearly visible discontinuities but encompass at least two fining upward-sequences. The conglomerates are of a beige to light grey colour. Grain sizes vary from 3 to 15mm. More finely-grained conglomerates are rather matrix dominated. The coarsest conglomerates examined are clast-supported with well-rounded quartz grains and a uniform grain size (5-10mm) (like sample M17). At the bottom of the outcrop, a coarsely-grained strongly-weathered friable sandstone *("Mürbsandstein")* is exposed, which shows a thickness of more than 10m in the west. It is cut by a reverse fault from a similar sandstone at its western side. The conglomerates have a reddish colour because of iron weathering. They lack prominent iron crusts, but some fractures have small rims (coating) of iron (cf. chapter 4.1.1).

The lower beds of the southwest wall contain abundant rip-up clasts. These are a few centimetres to several decimetres in diameter and mostly rounded and all show thin red to black rims of about 1 to 2mm (Fig. 14). The clasts consist of greenish fine-grained sandstone. This sandstone is only preserved within the clasts as a very thin layer of smaller than one millimetre, the rips-ups are rather hollowed/eroded, thus it was not possible to take any samples of it. Finely-grained intercalations of a greenish sandstone to silt-shale of about one metre in width and one to two decimetres in height, which are cut sharply by the conglomerates, constitute a rare, but prominent feature of the lower section of this wall. One

of these layers is surrounded by a centimetre-thick rim of an iron-enriched sediment (see Outcrop 3, Fig. 28).

Fig. 11 The right picture shows the southwest wall in June 2019. The south wall described before and in Löffler (2013) is marked with the red ellipse on the left picture. The locations of acquired structures are marked with numbers.

Structural measurements confirm that the beds dip at an angle of approx. 20° towards SE (Fig. 12; Besada, 1996). The mean value of the measurements was (129/26). The majority of beds of both walls are fractured. In the field, four distinct fracture sets were measured, which all dip quite steeply (around 70°). The prevalent fracture set dips steeply to the north (350/70), the others to northwest, east (095/80) and northeast (310/70). Features found on different fractures were Riedel shears, hackle marks, halos, iron crusts, idiomorphic calcite crystals or calcite crusts (cf. chap. 4.1.1). Fractures in the conglomerates of the southwest wall are less systematic than those recorded on the south wall. Although they evidence similar directions, there are no sharp boundaries between the beds, and the conglomerates are more massive and not fractured as thoroughly.

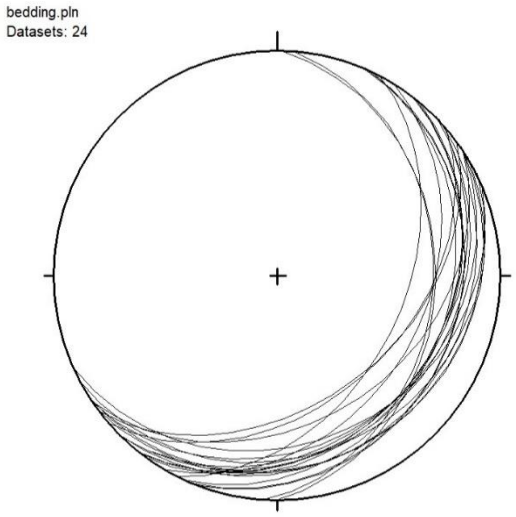

Fig. 12 The dip angle and direction of the bedding is approx. 20° towards SE, which agrees with Besada's measurements in 1996.

4.1.1. Field and macroscopic investigation of the iron crust

The greenish grey to brown quartz arenites of the quarry *"Strombauamt"* frequently show red to dark orange colours on their fracture surfaces with a thickness of about 1-2mm. With the appearance of a red crust on the surfaces of the sandstone, it macroscopically completely

differs from the original lithology. The red colour indicates iron mineral precipitations, which was confirmed by investigations with XRD and EDX, thus these red layers are referred to as *"iron crust"* in this work. The crust macroscopically seems harder and more cohesive than the often quite weathered sandstone; but because of its thin structure of about 2mm, it flakes off

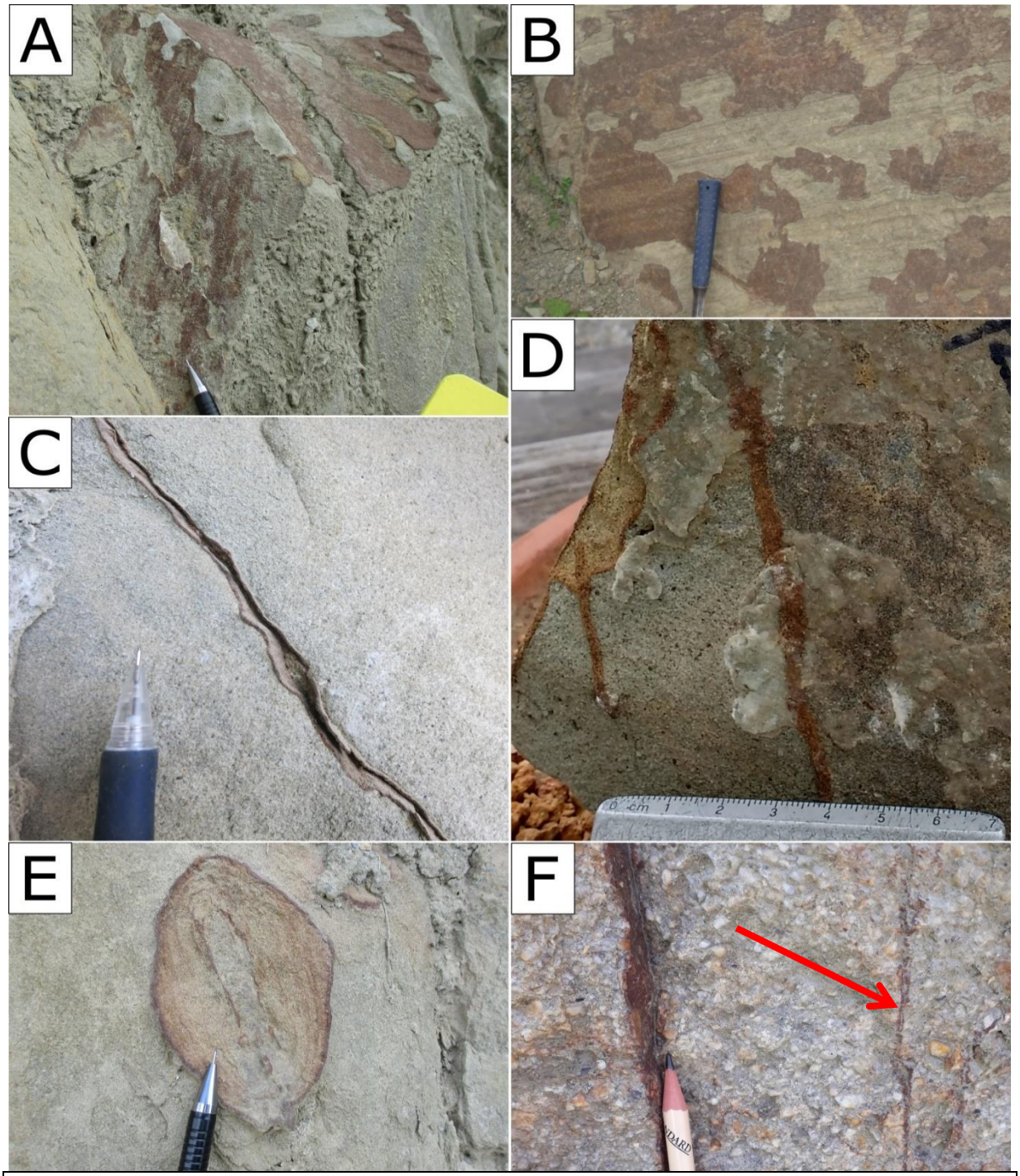

Fig. 13 **(A):** Typical habitus of iron crusts. Crusts are present on two fracture surfaces (350/50 and 171/88) and form a patchy cover of the host rock. **(B):** Lamination is still visible through the crust. **(C):** On both sides of the fracture, the rock is encrusted with the iron oxide. The partly open facture is filled with weathering products. **(D):** An iron vein cuts the sandstone. **(E):** Iron concretion forming Liesegang-type concentric diffusion rings. **(F):** The conglomerates in the west are stained red and show thin iron crusts on joint surfaces. On the right side of the picture, an iron vein cuts through the conglomerate (marked by an arrow).

easily at beds where the sandstone is more friable, whereas on other beds it is tightly connected to its host rock. The iron crust is a prominent feature of the massive sandstone beds of the south wall; and it continuously or patchily covers the fracture planes in this outcrop. Occasionally, the iron forms veins within the rock where the fractures were not open (Fig. 13D&F). The lamination of beds is still visible through the iron crust Fig. 13B). The iron precipitates also sometimes diffuse into the sandstone up to tens of centimetres and form concentric diffusion shapes or halos (Fig. 13E). Weathering evidently changed the appearance of the sandstones over time, forming red to dark brown surface coatings which superficially may resemble the iron-rich incrustations described in this chapter. Weathering-derived features, however, are readily discerned from the structures under consideration. The conglomerate beds in the west have fewer and thinner crusts (Fig. 13F), all of them occurring on joint set number 4. The conglomerates are a spottily-coloured light red. As already mentioned, their abundant rip-up clasts generally have thin dark red to black fringes (Fig. 14).

Fig. 14 The abundant rip-up clasts in the conglomerate beds have typically thin (about 1mm) dark red rims.

The crusts occur on the sandstones on both sides of a fracture (Fig. 13C-D) and are neither restricted to individual beds, nor to a specific group of fractures or a fracture set. Iron oxide precipitations may be found on each of the four differently-oriented fracture sets and on bedding planes (Fig. 13A, Fig. 16). Fracture planes, with and without crusts, are sporadically overgrown by fibrous calcite. (Fig. 15A). Other fractures expose iron crusts that were striated by slips on the surface after incrustation (Fig. 15B), and other crusts are overgrown by idiomorphic calcite or quartz (Fig. 15C, D). Iron crusts occur frequently in massive sandstone beds, but can also be found on more thinly-bedded layers.

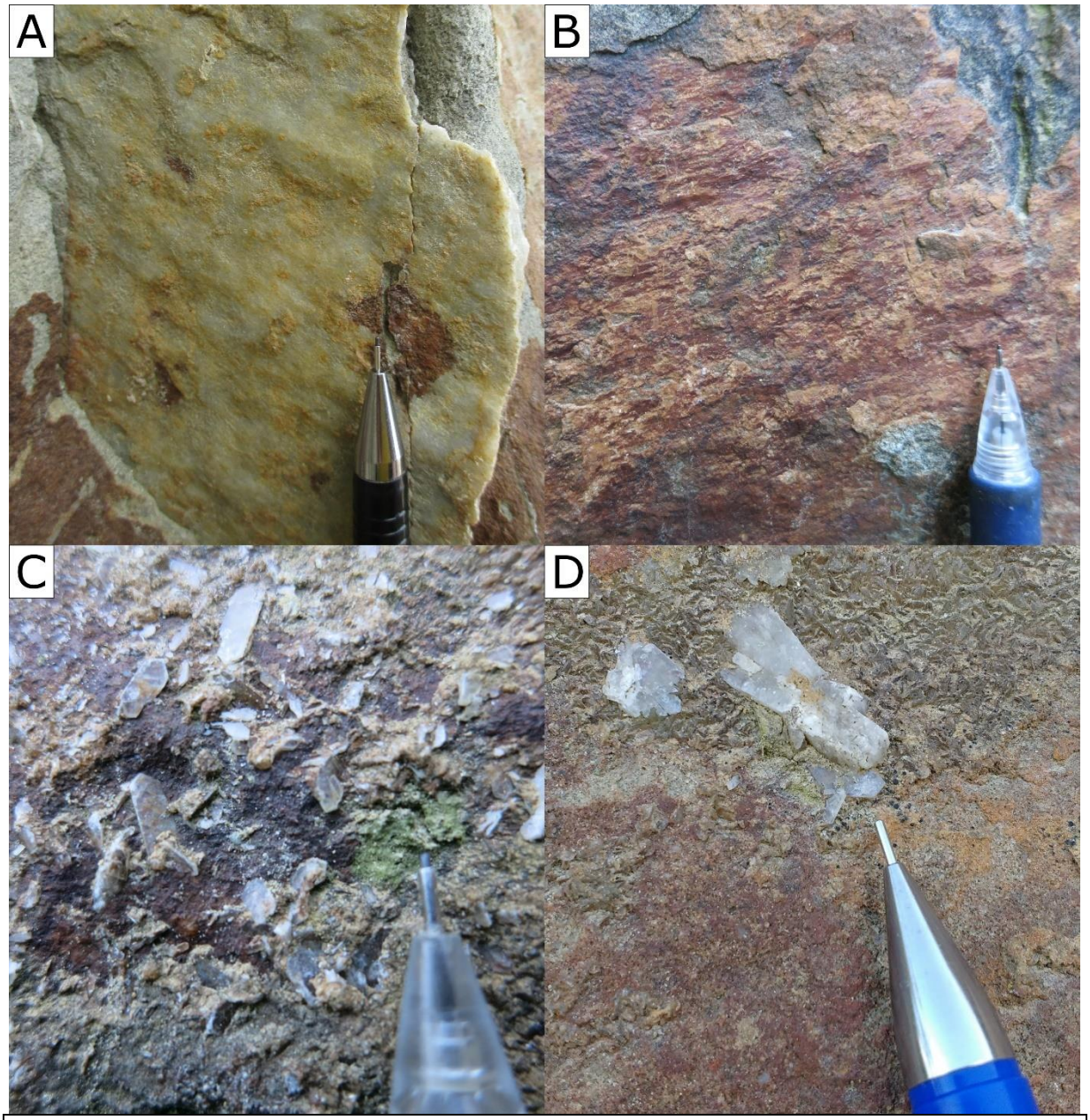

Fig. 15 **(A):** Fibrous Calcite growing on a partially-encrusted fracture plane. **(B):** The iron crust shows a striation. **(C):** Idiomorphic calcite crystals growing on the fracture plane. **(D):** Quartz crystals growing on the fracture plane.

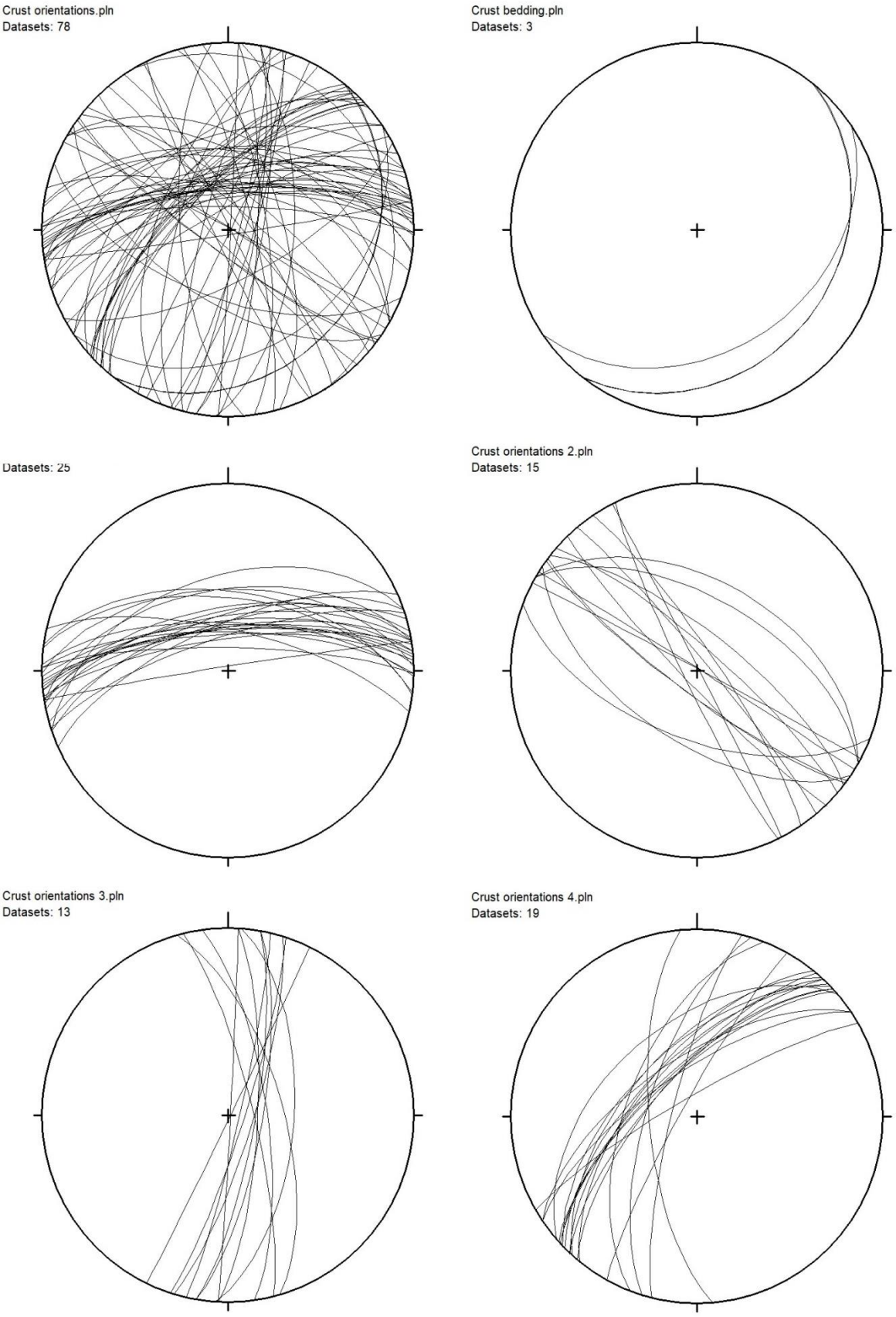

Fig. 16 All fractures with crusts were plotted in the top left circle. Fractures were then matched to a fracture set. 5 fracture sets were identified, including the bedding. All fractures evidence dips at steep angles. Set 1 dips towards N, Set 2 is a conjugated fault set dipping towards SW-NE, set 3 dips towards E and set 4 towards (W)NW. Set 3 and 4 could be matched as fractures of conjugated faults.

4.1.2. Outcrop 1

This outcrop is situated on the eastern edge of the south wall (Fig. 10). Two massive sandstone beds are interbedded by thin, strongly-weathered sandy to clayey layers (Fig. 17). They show conjugated normal faults. Iron crusts occur on all fracture planes. The clays and sands are stained orange to red.

Fig. 17 Outcrop 1: has to two sandstone beds interbedded by strongly weathered layers. Each bed was examined in detail, cf. Fig. 20 & Fig. 21.

Fe-encrusted fractures in Outcrop 1 comprise a set of steeply N-dipping fractures and a younger, crosscutting set of E- and W-dipping conjugated normal faults. All fractures are devoid of synkinematic mineralizations. Iron crusts are often slicken-sided and overgrown by idiomorphic quartz/calcite or fibrous calcite.

The conjugated normal faults in the lower bed (Fig. 18, Fig. 20) are delimited by fine-layered material on the top and the bottom, which is clayey and contains iron and carbonate. The conjugated normal faults are tilted with the bedding. Some fractures with iron crusts evidence 1-2mm openings, with the iron crusts appearing on both sides of the open fracture. The conjugated faults dip towards the east and the west indicating E-W-directed extension and cut fractures of the prevalent steeply north-dipping joint set (Fig. 18, Fig. 19). At some parts, the sandstone adjacent to the fault appears laminated or banded parallel to the faults. These *“pseudo-laminated”* sands attain thicknesses of up to several centimetres (Fig. 20).

The upper bed of Outcrop 1 (Fig. 21) was logged separately on a subsequent day and shows features similar to the lower bed. Steeply N-dipping fractures are cut by normal faults. The sandstone also has these pseudo-laminations parallel to the normal faults. Measurements confirm a conjugated fault set consisting of ENE-dipping and WNW-dipping faults that cut a set of steeply N-dipping fractures (Fig. 22, Fig. 23).

Samples M2, M3, M5, M6 and M7 were taken at this outcrop. When correlated with Besada’s profile (Fig. 4), Outcrop 1 is the lowest part of the top of the profile (101 -104 m).

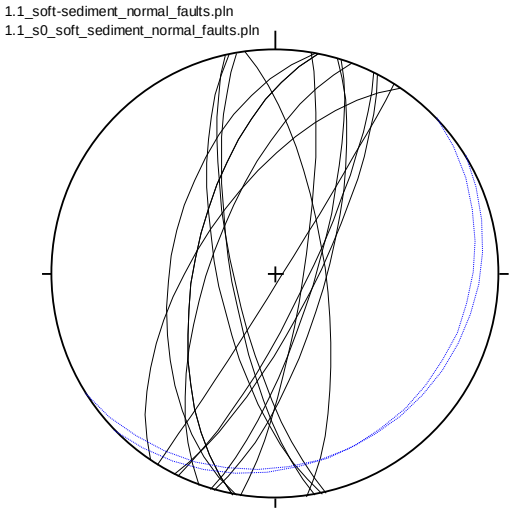

Fig. 18 Conjugated soft-sediment, steep, east-west trending normal faults (black great circles) and bedding planes (blue).

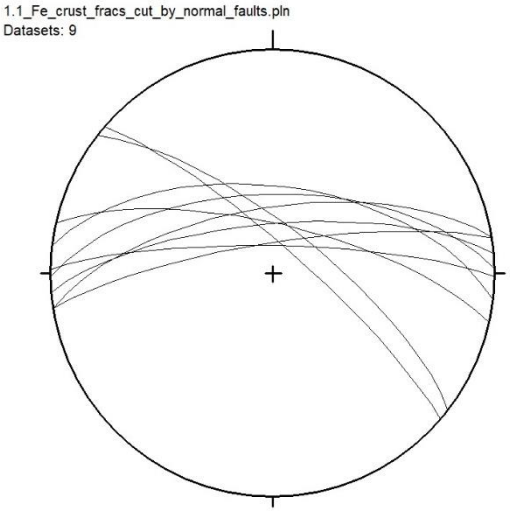

Fig. 19 These steep north/northwest dipping fractures with iron crust are cut by the normal faults of Fig. 18.

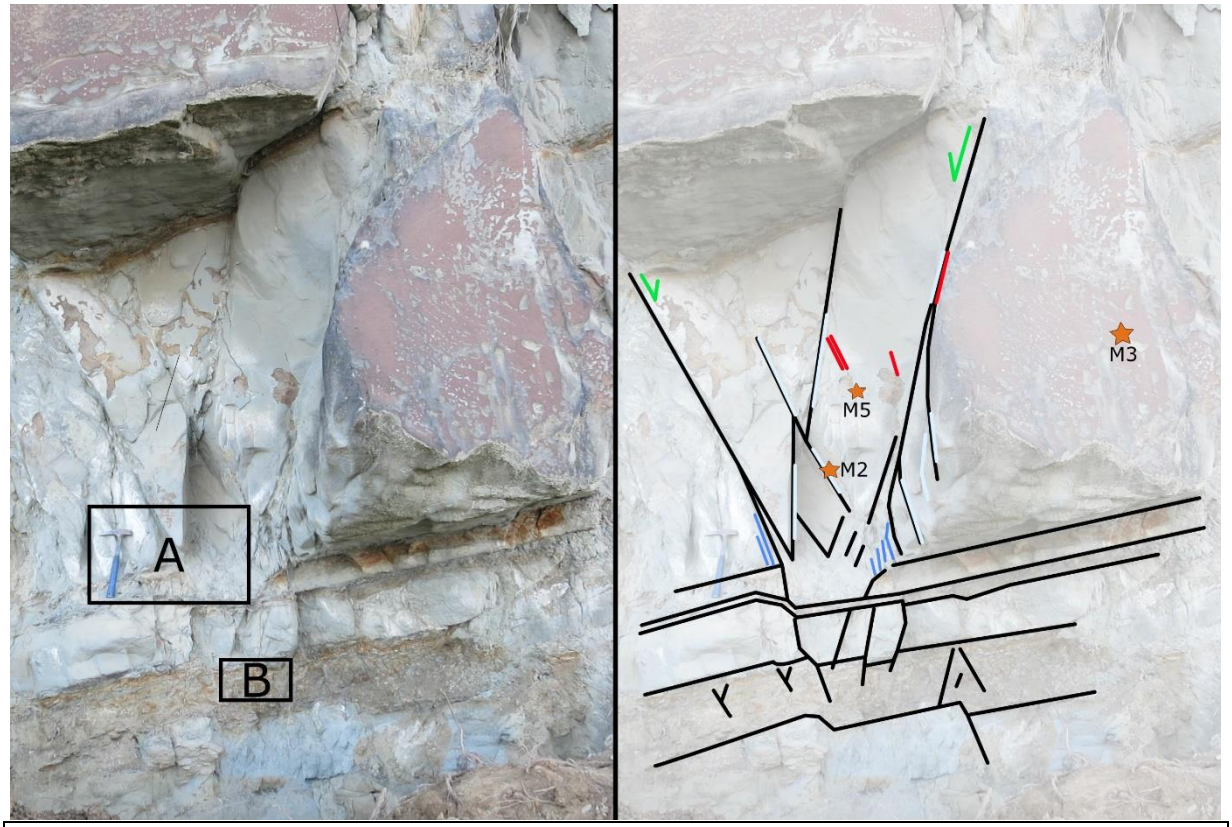

Fig. 20 The lower bed of structure one: E- and W-dipping conjugated normal faults with sandstone showing fault-parallel pseudo-laminations (blue, right of hammer). Detail of Fig. 17. View is towards S. Iron crusts and calcite overgrowths parallel to the normal faults are marked red and white. Samples that were taken are marked with orange stars. Frames with letters A and B are shown in detail in Fig. 24A and B.

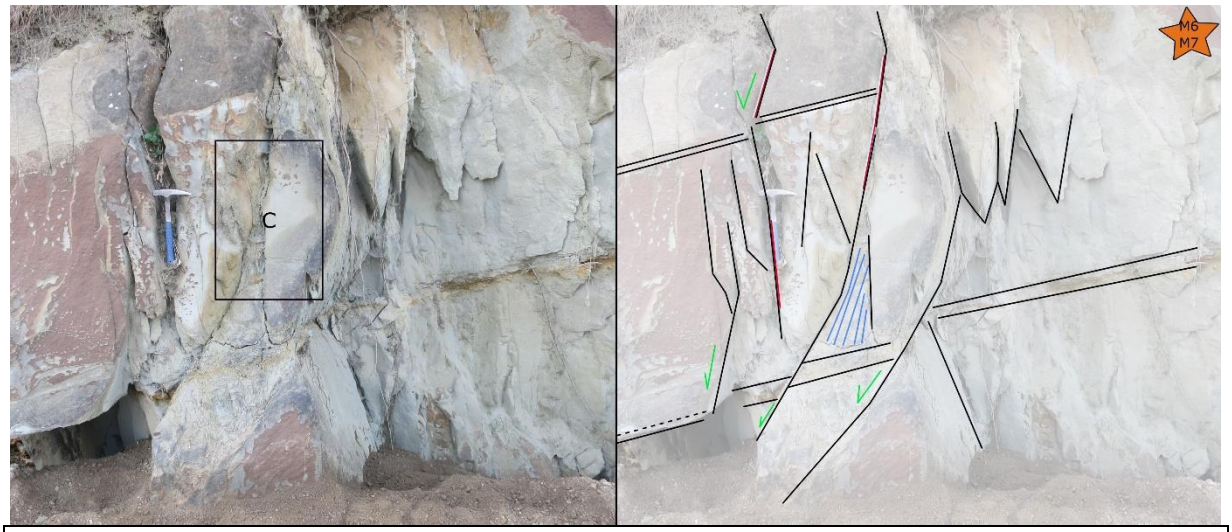

Fig. 21 Upper bed of Structure 1: E-W-dipping faults cutting Fe-encrusted, steeply N-dipping fractures (left of hammer, facing towards camera). Samples that were taken are marked with orange stars. View is towards S. Frame with letter C is shown in detail in Fig. 24C.

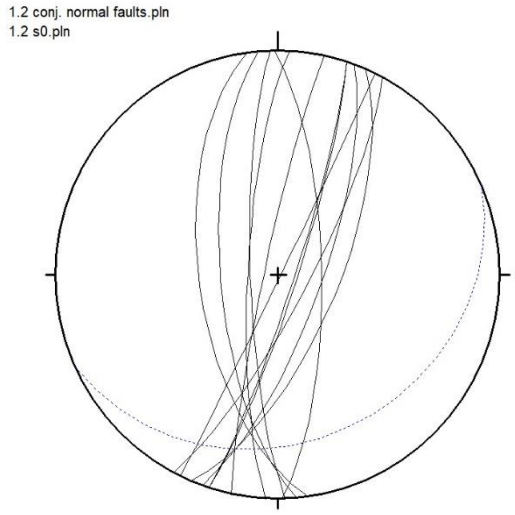

Fig. 22 As in the case of the lower bed, the upper bed of Structure 1 also shows conjugated soft-sediment, steep, east-west trending normal faults (black great circles) and bedding planes (blue).

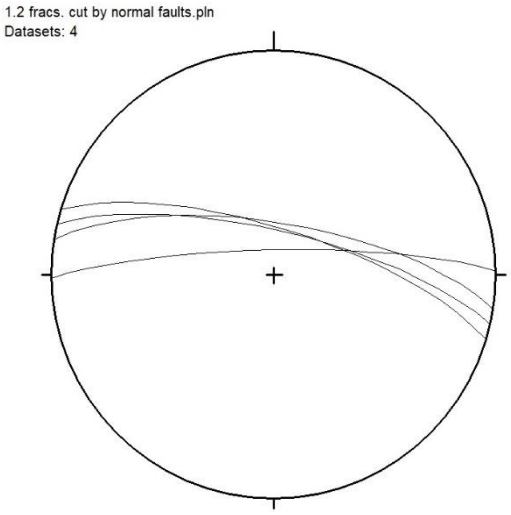

Fig. 23 These steeply north-dipping fractures with iron crust are cut by the normal faults of Fig. 22.

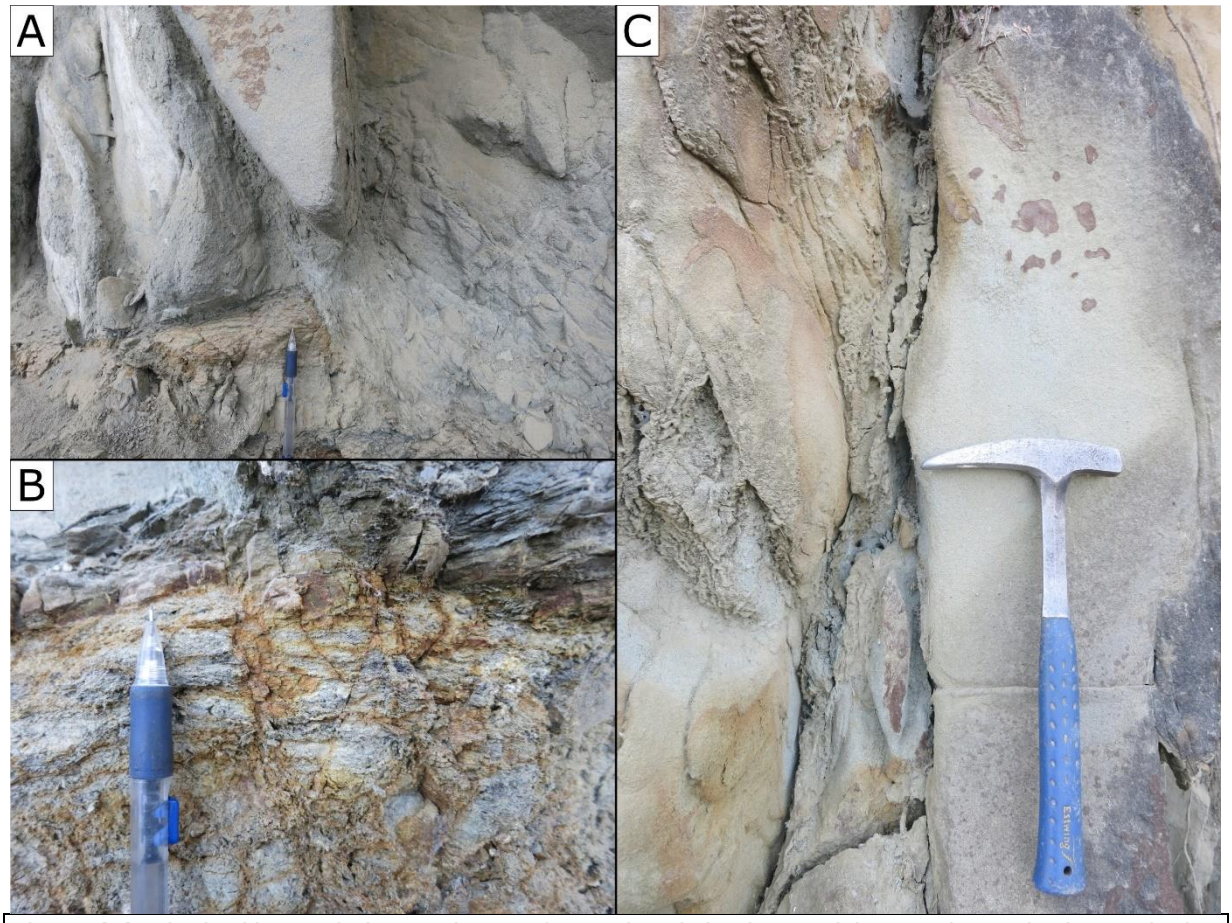

Fig. 24 **(A):** The bed beneath the sandstones is cut sharply by the overlying sandstone bed, constituting an erosive base. The massive sandstone bed is laminated subparallel to the fractures. **(B):** Strongly-weathered, iron rich, pseudo-faulted layers of sandy to clayey material are interbedded between the massive sandstone beds. **(C):** (Pseudo-)laminations parallel to the normal faults.

4.1.3. Outcrop 2

Outcrop 2 (Fig. 26) is situated in the middle of the main south wall and exposes a massive conglomerate bed. The sandy conglomerates are finely-grained with components of 5-7mm, consisting mainly of quartz. Fe-encrusted fracture planes show a mean dip angle and direction of 318/70 (Fig. 25). The rock shows laminations/striations adjacent to the faults, a feature that aligns with the pseudo-laminations of Outcrop 1 (Fig. 20). The iron crust of this structure is diffused several centimetres into the rock. Samples M9 and M10 were taken here. This bed aligns with metre 80 in Besada's profile.

Fig. 25 Fe-encrusted fractures of Outcrop 2 dip steeply to the NW. They are cut by a steeply SW dipping fracture.

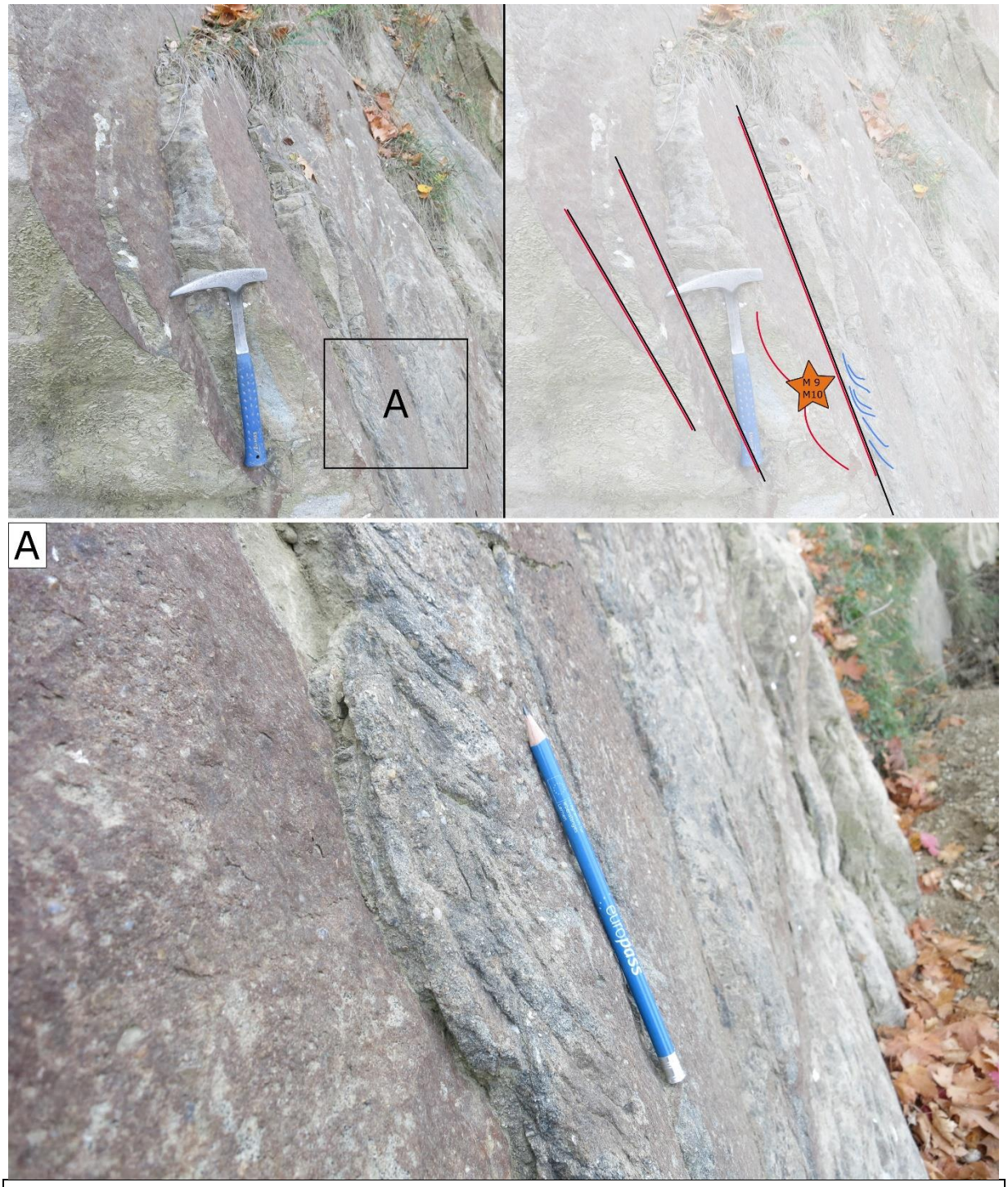

Fig. 26 The finely-grained conglomerates in the middle of the south wall have abundant iron crusts on strongly NW-dipping fractures. There are laminations extending from the fractures. The iron shows diffusion patterns further into the sandstone at one fracture (sample M9/M10!).
(A): A detailed picture of the laminations extending from the fracture surface. The location of (A) is framed in the upper picture.

4.1.4. Outcrop 3

This outcrop is situated at the southwest wall. It consists of poorly-sorted, medium-grained conglomerates (Fig. 28, Fig. 29) with components 1-10cm in size. There are abundant rip-up

clasts with red rims in this bed. It shows complex, less systematic faulting/fracture systems than the outcrops at the south wall, with fractures dipping to the W and cut by N-dipping fractures (Fig. 27).

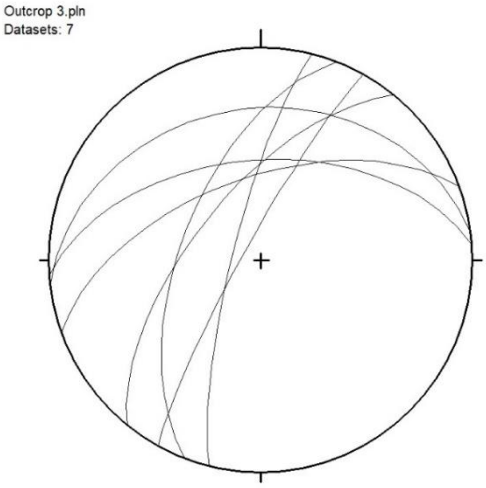

Fig. 27 Fractures of outcrop 3 are dipping to the NE and N

A finely-grained, but poorly-sorted intercalation of a grey-greenish silty to clayey conglomerate is interbedded in between the conglomerates on the west side of this outcrop (Fig. 28A). It is about 20cm thick and 70cm wide. The grain size of the layer is coarser in the middle, whilst on the rim it is just clay. Its most significant feature is its thick red brown limonitic rim. At some points along the edge, there are even thicker iron concretions and very iron-rich clays (Fig. 28B,D) They are more consolidated than the rest of the lithologies of this area. The layer is surrounded by sub-rounded rip-up clasts of greenish sandstone, which have an iron-red rim. Rip-up clasts are abundant in this part of the section at the southwest wall. Veins/fractures that extend away from the intercalation are stained by an iron crust (Fig. 28C).

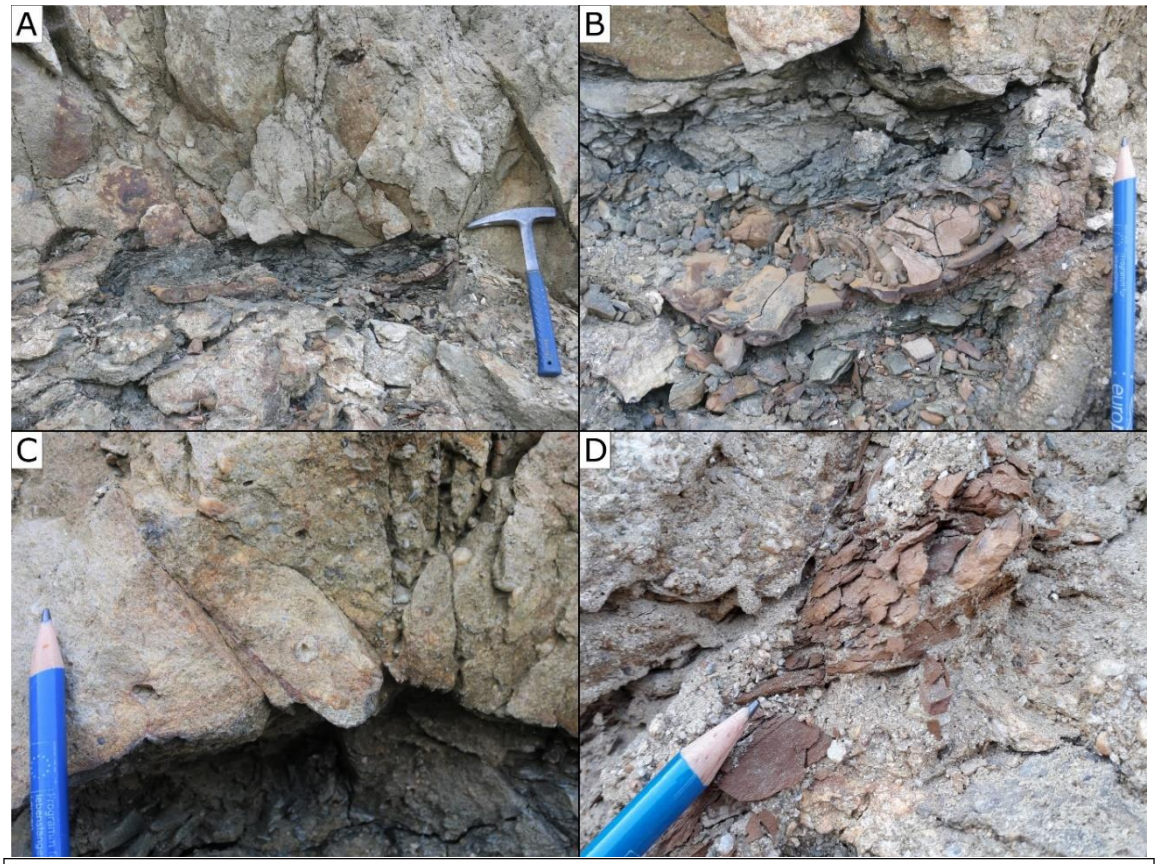

Fig. 28 **(A):** An approximately 20 cm thin layer of a weathered, greenish, poorly-sorted clayey and sandy rock is surrounded by orange to red clayey iron concretions. It is about 70 cm wide and cut by the overlying and underlying conglomerates. Rip-up clasts surround this layer. **(B):** Detailed picture of one of the iron concretions within this layer. It is finely-grained and more solid than the rest of the layer. **(C):** Fractures originating from the layer show iron crusts. **(D):** An iron concretion near the layer.

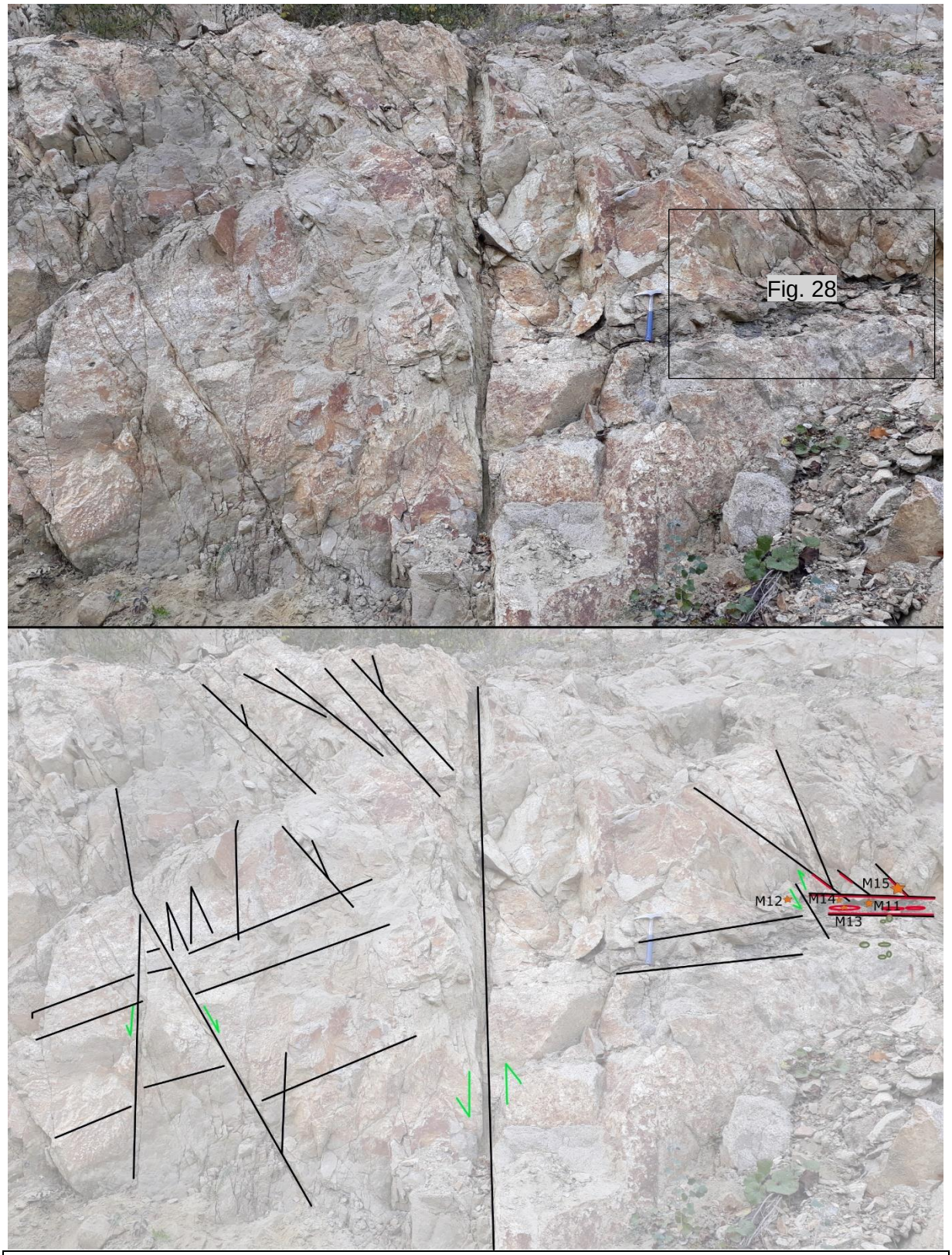

Fig. 29 The conglomerate bed of Outcrop 3 is complexly fractured. The layer described before is situated at the right edge of the picture, where samples are marked with stars.

4.1.5. Outcrop 4

Outcrop 4 (Fig. 31) is located below Outcrop 3 and consists of one bed of highly-weathered conglomeratic sandstone with abundant rip-up clasts of a greenish sandstone. This is similar to outcrop 3. A number of large rip-up clasts measuring up to a few decimetres in diameter were found. A layer of greenish sandstone is within this area and is cut by conjugated faults sharply on its right and left side, while factures parallel to the right fracture begin above the layer. The conglomerate shows pseudo-laminations subparallel to the faults.

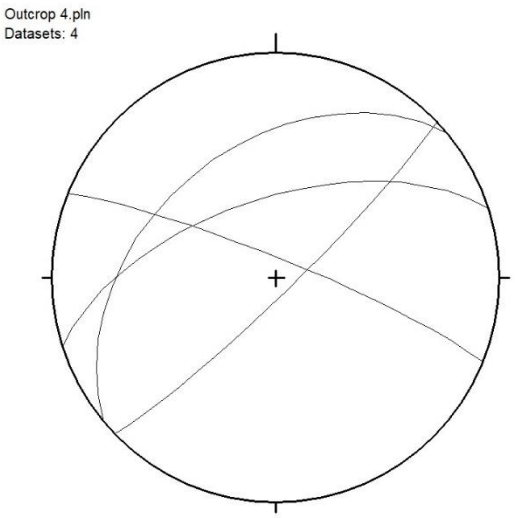

Fig. 30 The conjugated faults of Outcrop 4 dip towards NW and SE and are cut by NE-dipping fractures.

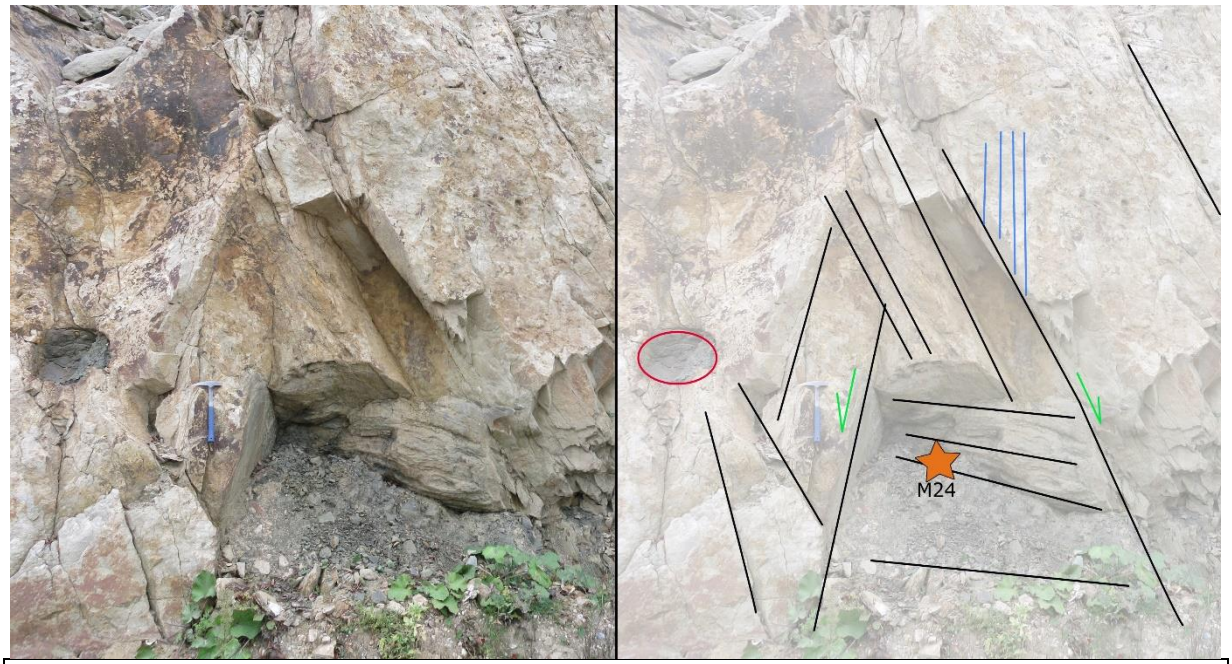

Fig. 31 A conjugated fault cuts a layer of greenish sandstone (sample M24). Pseudo-laminations are coloured blue; a big rip-up clast is marked red.

4.2. Sample description and rock petrography

4.2.1. Macroscopic description of the samples

Hand samples were labelled with an M plus an ordinal number, with M denoting *"master's thesis".* Thin sections were designated according to the hand samples they were derived from, with the exception of thin sections from sample M1, which were called GR1a_I to GR1c_II, with GR standing for Greifenstein, the locality of the quarry.

The samples are numbered in the order of collection and, with a few exceptions, largely from top to bottom. As far as possible, correlation with Besada's profile was attempted (Fig. 4).

A list of all samples with associated pictures can be found in the Appendix.

4.2.2. Sandstone classification

The sandstones in the quarry contain abundant quartz and have been classified by Besada (1996) and Löffler (2013) using triangle plots after Pettijohn, Potter & Siever (1987)/Folk (1968). Löffler classified all samples as quartz arenites, whereas Besada found most of them to be sublitharenites and only some quartz arenites. In any case, it can be concluded that these rocks are abundant in quartz and contain some feldspar. As they are quite rich in glauconite (up to 35%), they can also be referred to as glauconite-bearing quartz arenites (Löffler, 2013).

4.2.3. Sandstone petrography

Thin sections of the sandstones, most of them with an iron crust, show the differences and similarities between the sandstone beds. The main component of all sandstones is quartz, with other abundant minerals being glauconite, K-feldspars (microcline), chlorites and mica (muscovite and biotite, glauconite) – cf. chapter 4.2.5. Calcite is present in the form of various fossils like foraminifers (Fig. 32) and as cement. Zircon, rutile, chlorite and pyrite are found as accessories in all samples (Fig. 35). Rutile is more present in M8 as opposed to other samples. Abundant amounts of very small brown idiomorphic grains of an iron mineral are found in M1, M4 and M10 (Fig. 33); they are also present in the other samples, but are not abundant.

Samples M1 and M4 evidence abundant calcite cement, whereas samples M2, M3 and M8 have little to almost no calcite cement. Sample M10 shows moderate amounts of calcite cement (cf. Fig. 34, Fig. 36). M8 and M10 are also cemented with clay intraclasts (Fig. 36A-C). These include partially-dissolved quartz and feldspar grains that show secondary intragranular porosity. Secondary quartz replaces feldspar and other minerals or grows on grains and forms quartz cement/overgrowths (Fig. 34). Micas are often bent due to compaction and form secondary pores (e.g. in Fig. 33C&D).

Grain sorting in all samples is poor. Grains of samples M1, M3, M8 and M10 are angular to subrounded, while M2 and M4 are subrounded. They all have mostly concave-convex contacts. M1, M4 and M10 are not as closely-packed as the other samples, as they also have point contacts, and their pore space is filled with calcite cement (Fig. 38). The frequency of point contacts in M1 and M4 is almost as high as the one of concave-convex, while M10 rarely shows point contacts.

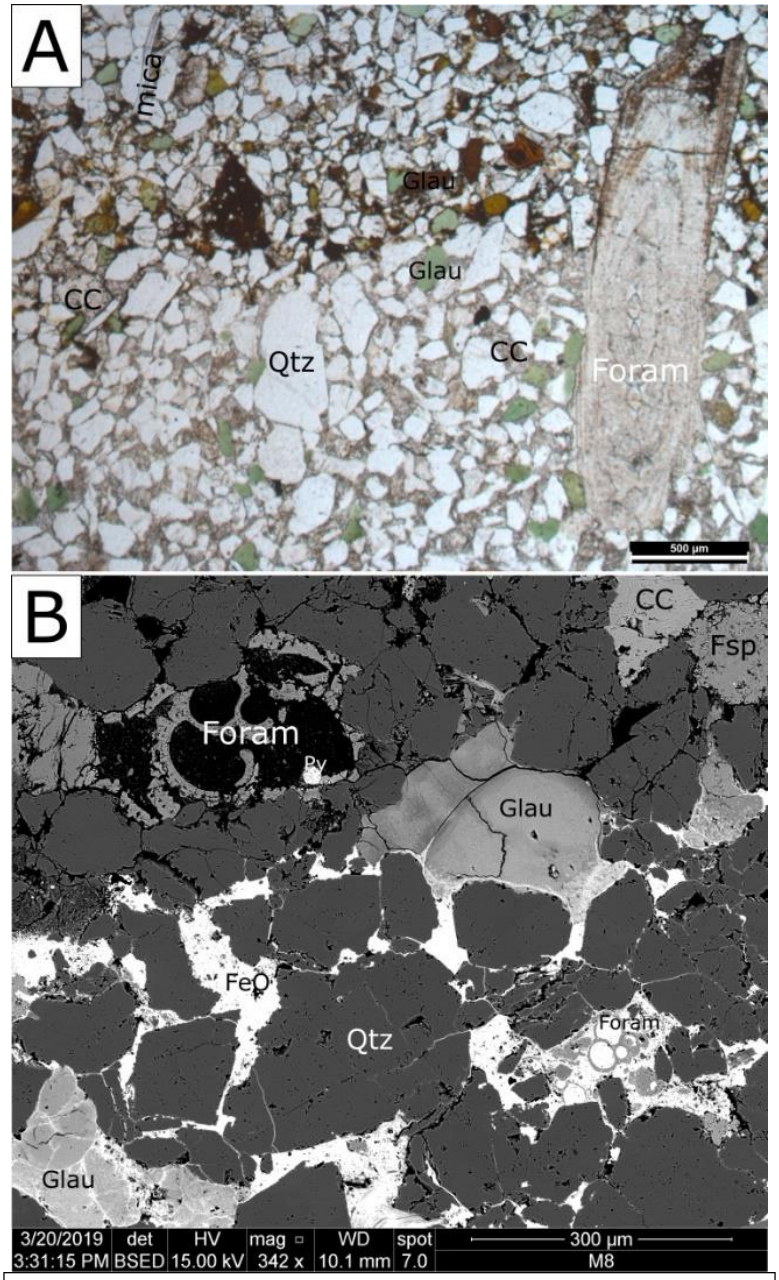

Fig. 32 **(A)**: Photomicrograph (PPL) of sample GR1a_II showing a large (benthic?) foraminifer on the right side. **(B)**: BSEM-picture with two fossils (foraminifers). The foraminifers were not identified any further.

Grains are often fractured and re-cemented without or with little translation, so their pieces fit in a jug-saw puzzle pattern. On the edge of a rock with joints opened by deformation, fractured grains are a very common feature (Fig. 36E-F). BSEM identifies weathering/alteration of glauconite grains. Some glauconite grains have darker and lighter areas (labelled glauconites in Fig. 37A-C), others show lamellar structures (labelled glauconites in Fig. 37D) and some have strange more lightly-striped grain boundaries (labelled glauconites in Fig. 37E-F).

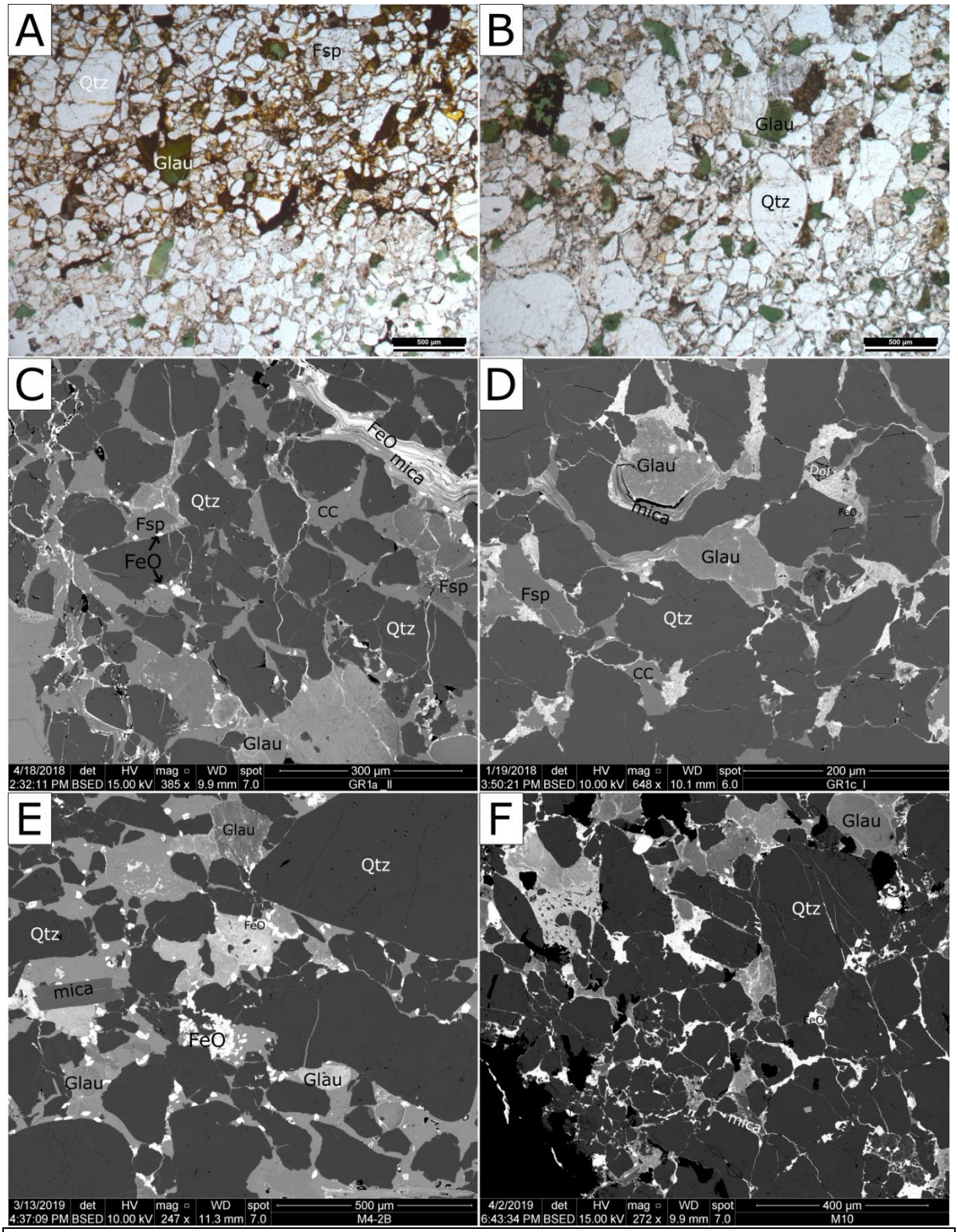

Fig. 33 **(A-B)**: Photomicrographs (PPL) of samples GR1a_II and M4-2B. Very small brown to green grains in between larger grains are present in these samples. **(C-F)**: These grains in BSEM are the small white grains. When measured with EDAX, it is Fe and O. **(C-D)** have bent micas (medium to light grey); the one in (C) is partially-filled with iron precipitates.

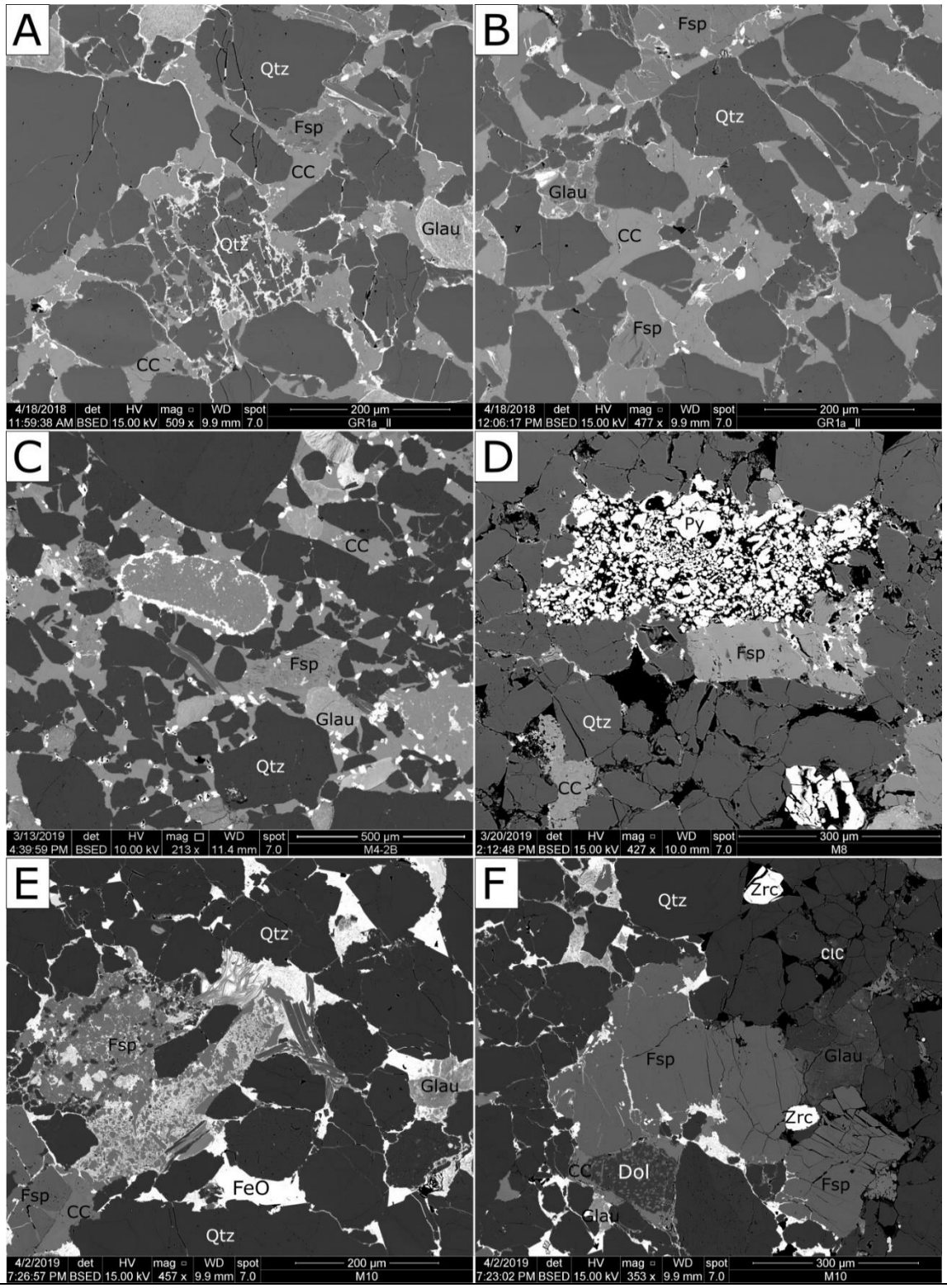

Fig. 34 Grain dissolution and replacement in different samples. Many grains in several samples are fractured. Even rims of quartz grains are a sign of quartz overgrowth (quartz cement) **(A):** The quartz in the lower middle of this picture is broken, partially dissolved, fragmented and cemented with calcite and *"iron crust"*. **(B):** The feldspar in the lower part of this picture shows dissolution *"veins"* at the bottom, which are filled with quartz. A quartz grain on the right is partially dissolved and largely replaced by calcite. **(C):** The remains of a dissolved, yet unidentifiable well-rounded grain are surrounded by iron precipitates. **(D):** Pyrite nodules. Quartz is growing in the feldspar in the middle. **(E):** Disintegrated grain with feldspar, quartz and clay, maybe a lithic fragment, feldspar is quite weathered, whereas few quartz grains remain stable. The micas above it are bent. Pore space is filled by iron precipitates and calcite cement. **(F):** Dolomite is partially dissolved and replaced by calcite. Clay cement (ClC) fills the pores in the upper middle-right part of the picture.

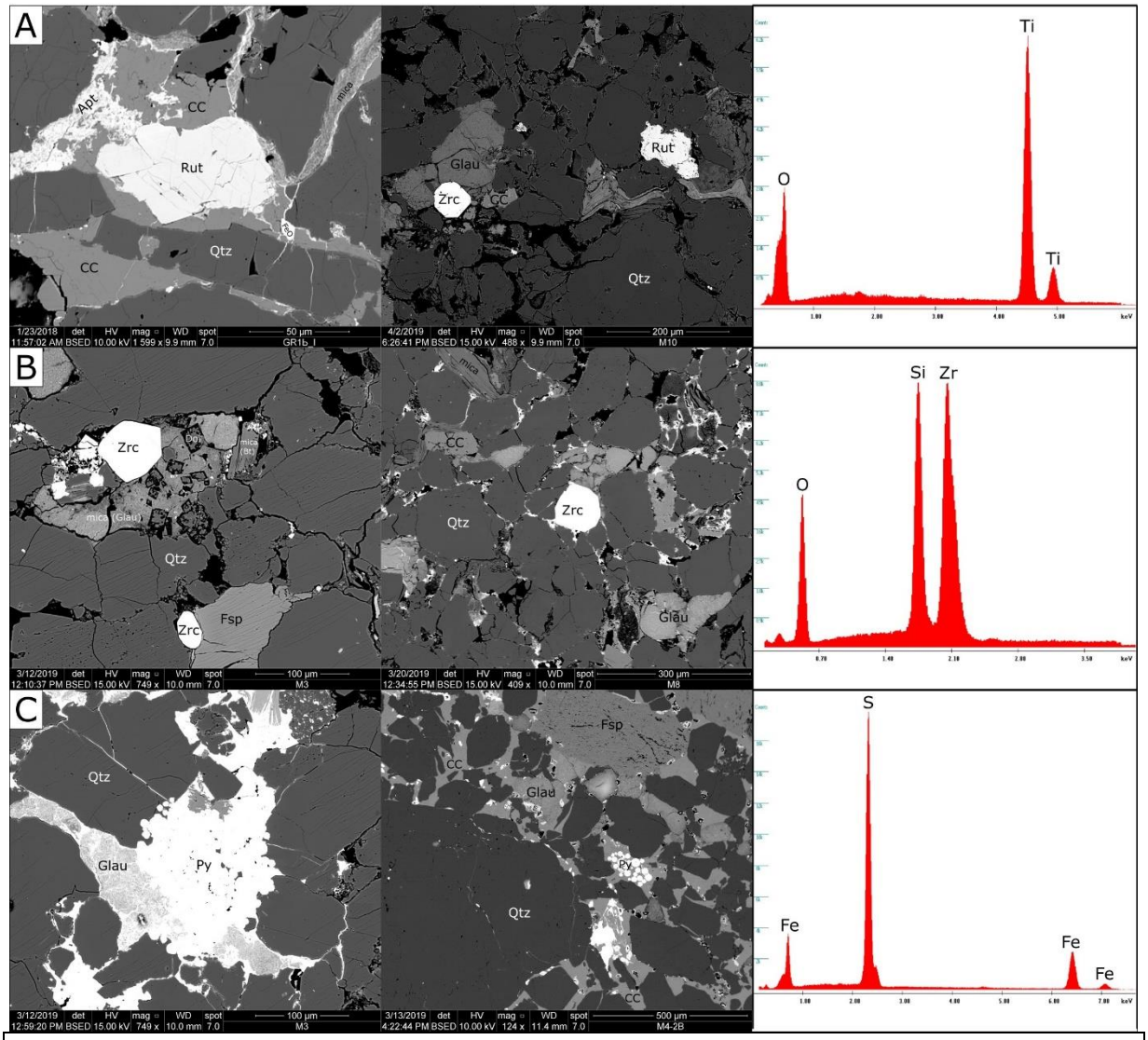

Fig. 35 Heavy minerals found in different samples. **(A):** rutile (Rut) in samples GR1b_I and M10. The left two pictures were produced with BSEM, and the right picture is the corresponding EDX measurement of the rutile grain in sample M10. **(B):** zircon (Zrc) in samples M3 and M8 and an EDX measurement of a zircon in sample M10 **(C):** pyrite (Py) in samples M3 and M4-2B EDX measurement of sample M3.

4.2.4. Microscopic description of the iron crust

It can be clearly seen in the thin sections that the crusts are enriched in iron minerals. The iron does not form a distinct layer of iron minerals in the crust area, but stains the pore space of the host rock in the outer 0.5 to 2.6 mm of the section close to the joint. The iron precipitates were never detected farther than about 2.6 mm into the rock.

When calcite cement is present, like in sample M1, the iron phase forms a kind of *"grain coating"* and fills the tiny spaces between cement and grains or between pieces of broken pores, whereas calcite fills the majority of the pores. In samples lacking calcite cement, iron minerals often fill the entire pore space (Fig. 39, Fig. 40).

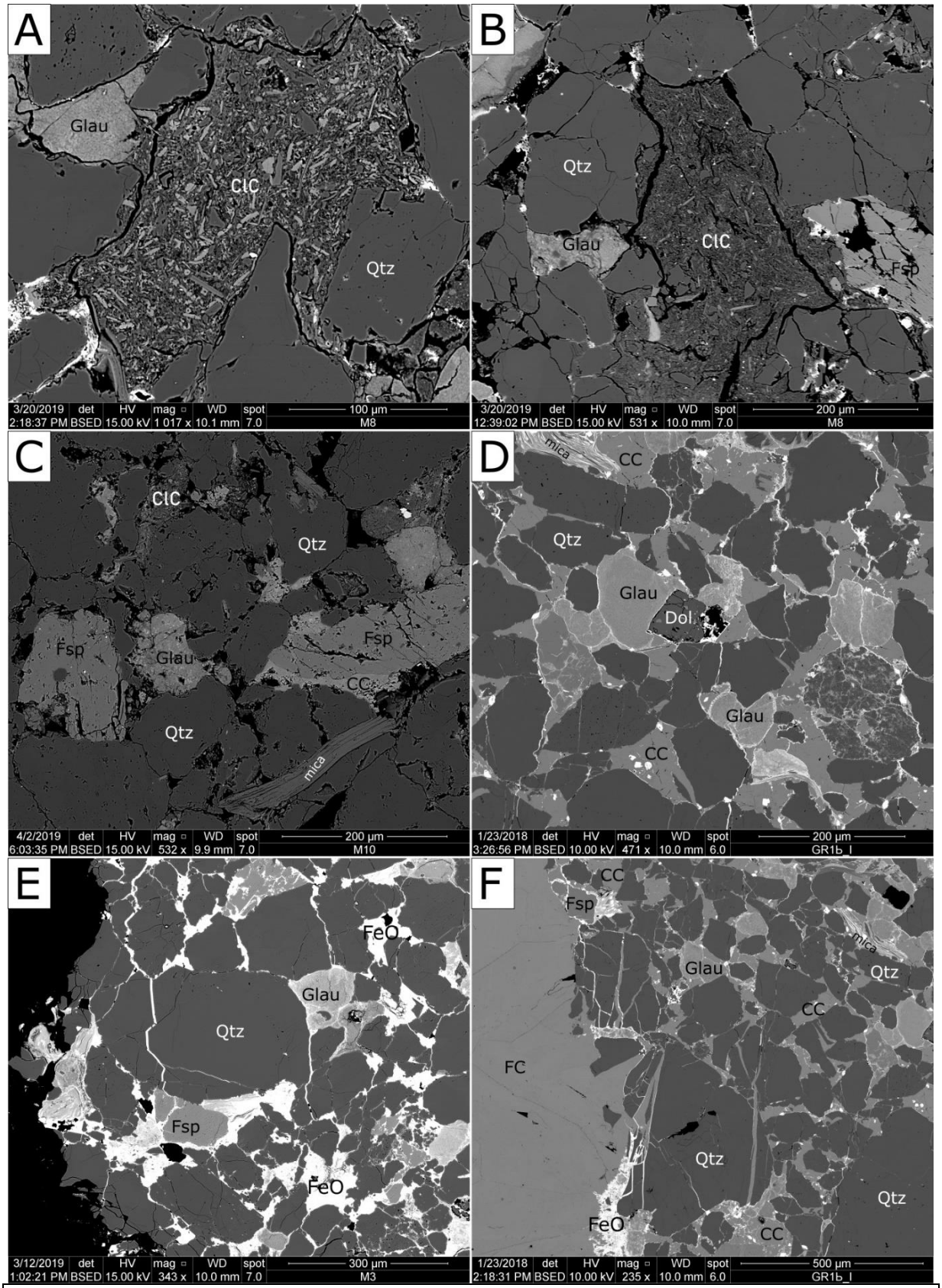

Fig. 36 **(A)-(C)**: Examples of clay intraclasts (CIC) in thin sections M8 and M10 (in the upper half of the picture C). **(D):** A dolomite grain in the centre of this picture of sample GR1b_I. **(E-F)**: Broken recemented grains. The iron oxide fills all the pores of M3, whereas GR1b_I is cemented by calcite cement (CC) and the iron oxide phase.

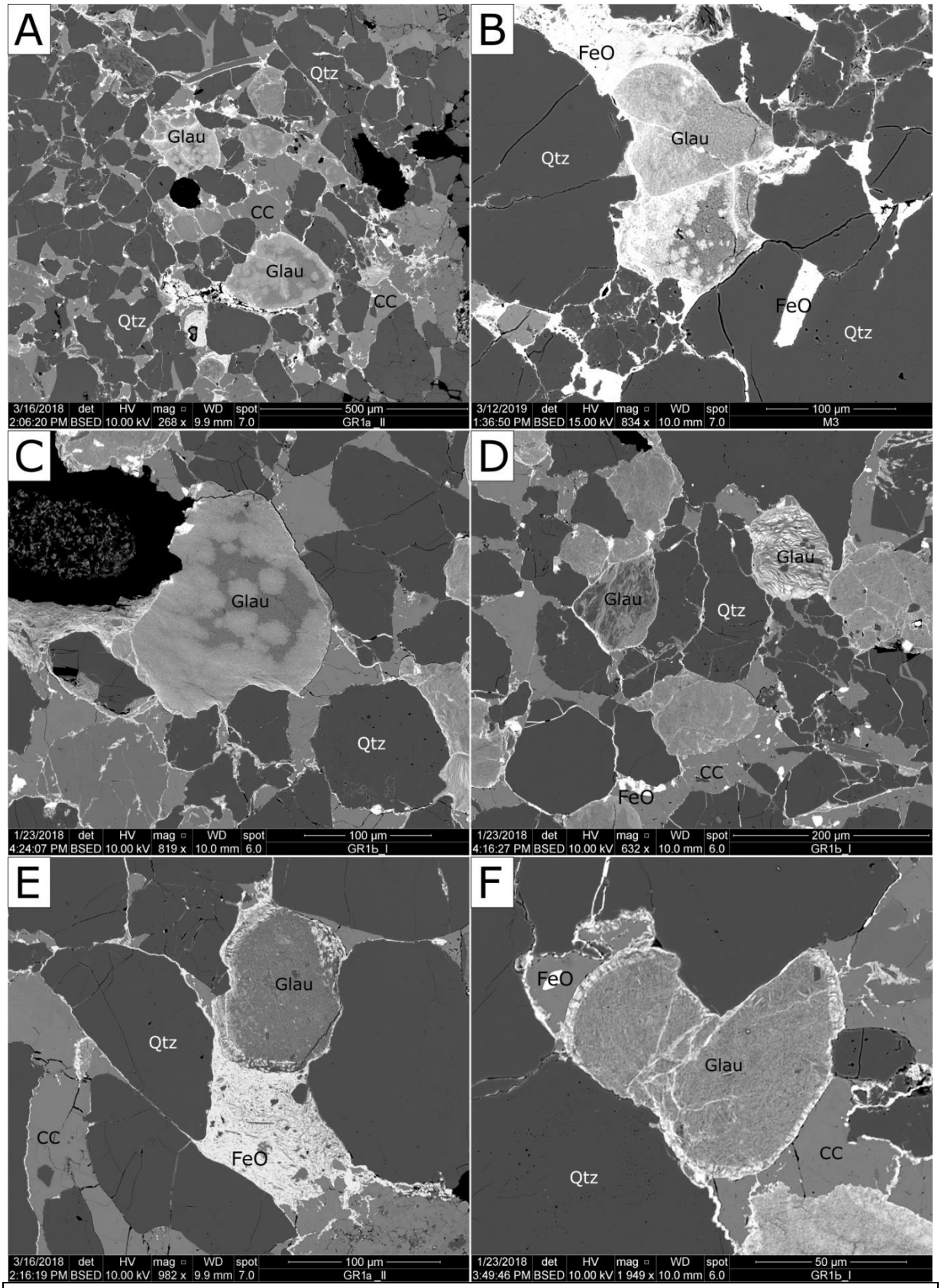

Fig. 37 Varieties of glauconite and altered glauconite. **(A-C):** patchy glauconites: darker and lighter zones, with lighter grey tones corresponding to heavier elements; EDX measurements identified a higher iron content in these areas, while the darker areas have less iron. **(D):** two fibrous glauconites in the middle contain two distinct phases. The left one has dark grey and light grey lamellar structures, whereas the right one has middle grey lamellas filled with a white phase and a few dark grey grains. **(E-F):** zoned glauconites in these two pictures contain concentric white-grey striped rims.

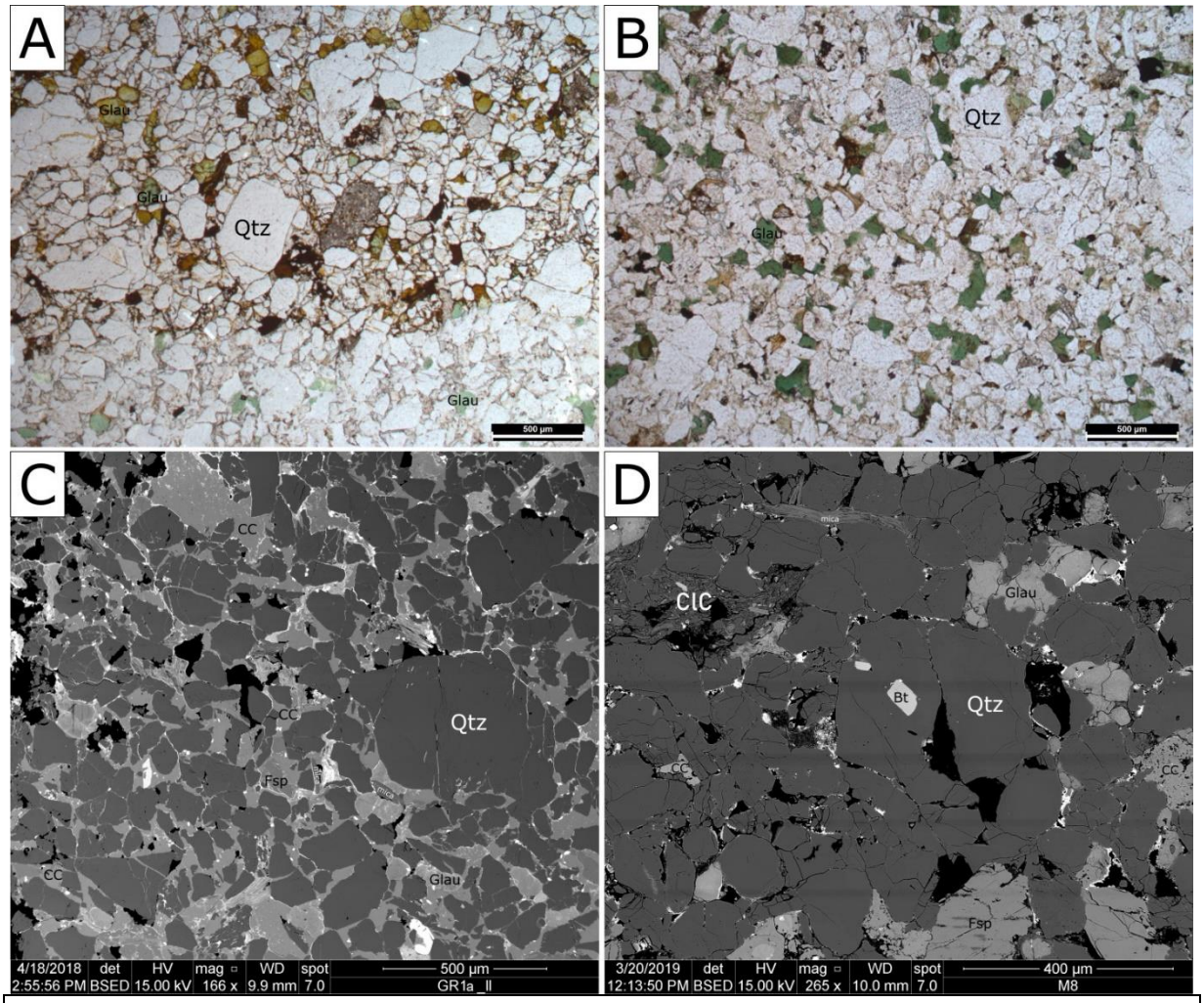

Fig. 38 Comparison of grain contacts and packing **(A-B)**: Photomicrographs of samples GR1a_II (A) and M3 (B), plane polarized light (PPL). **(C-D)**: BSEM picture of sample GR1a_II (part of sample M1, C) and M8 (D). When comparing the textural features, it can be seen that samples M3 and M8 are more closely packed, whereas sample M1 also has point contacts, and the pore space is cemented with calcite (see Fig. C, light grey on BSEM, quartz is dark grey).

In some samples (e.g. GR1a_II), the iron phase increases in density toward the outer rim of the crust containing fine quartz, calcite and feldspar grains (Fig. 40C). Macroscopically, M4 does not look different from the other samples. Microscopically, sample M4 differs from the other samples, as it has abundant fine brown grains with average sizes of about 50 µm. In thin sections, these little grains are damaged and partly dissolved in the host rock, whereas they completely consist of iron minerals in the crust area (Fig. 39E-F). The rock and crust are often overgrown with structural calcite fibres (e.g., Fig. 36F, Fig. 39A&E, Fig. 40C&D). Sample Gr1a_II (M1) reveals two distinct directions of grain fracturing; and iron precipitates only fill cracks and little spaces between calcite cement and grains in this sample (Fig. 41). A visual estimate of the iron content suggests up to 1% iron in samples with calcite cement and up to 15% (e.g., sample M3) in rocks without calcite cement.

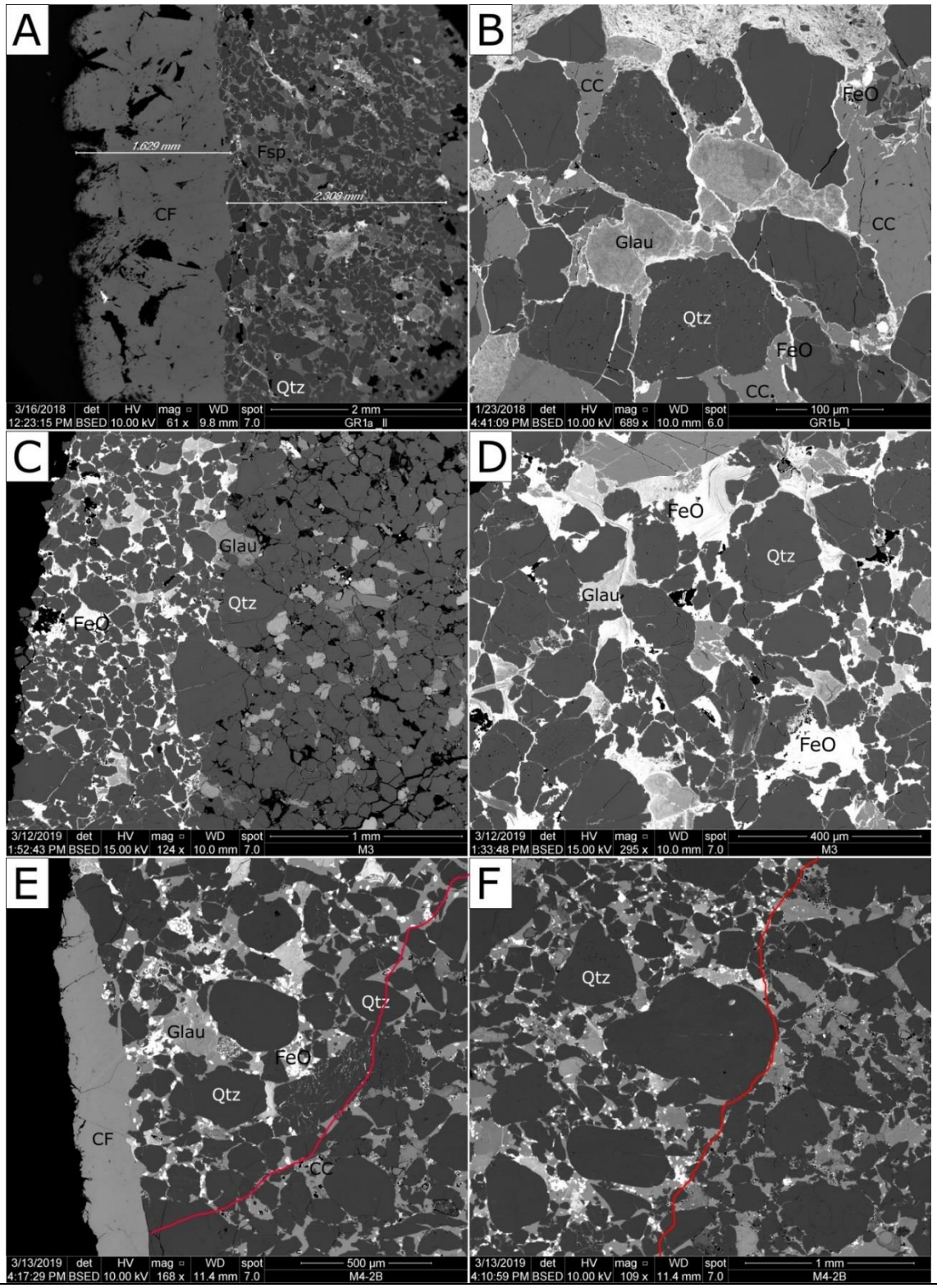

Fig. 39 Dimensions and appearance of the iron crusts from the BSEM of 3 different samples. **(A-B):** The iron crust in sample M1 (GR1a_II and GR1b_I). GR1a_II shows the thickness of one iron crust (2.3 mm) covered by structural calcite fibres (CF, 1.6 mm) growing in the fractures. **(B):** (GR1b_I) is a closeup of the crust, showing it fills all grain boundaries including the calcite cement, as well as cracks within the grains, and additionally forms small idiomorphic iron oxide grains (little white grains) **(C-D):** The iron minerals in sample M3 fill the whole pore space of the roughly 1mm of the fracture edge (left). **(E-F):** The iron crust in sample M4 is shown as only a very few, small idiomorphic white iron oxide grains (Left halves of both pictures). These grains continue on the right half, but are not filled with iron; rather, they are half empty, dissolved, unidentifiable grains containing magnesium and iron (cf. EDX Fig. 53). The calcite crust at the left of figure E consists of small calcite fibres that grew on the rock surface and lack iron oxide minerals.

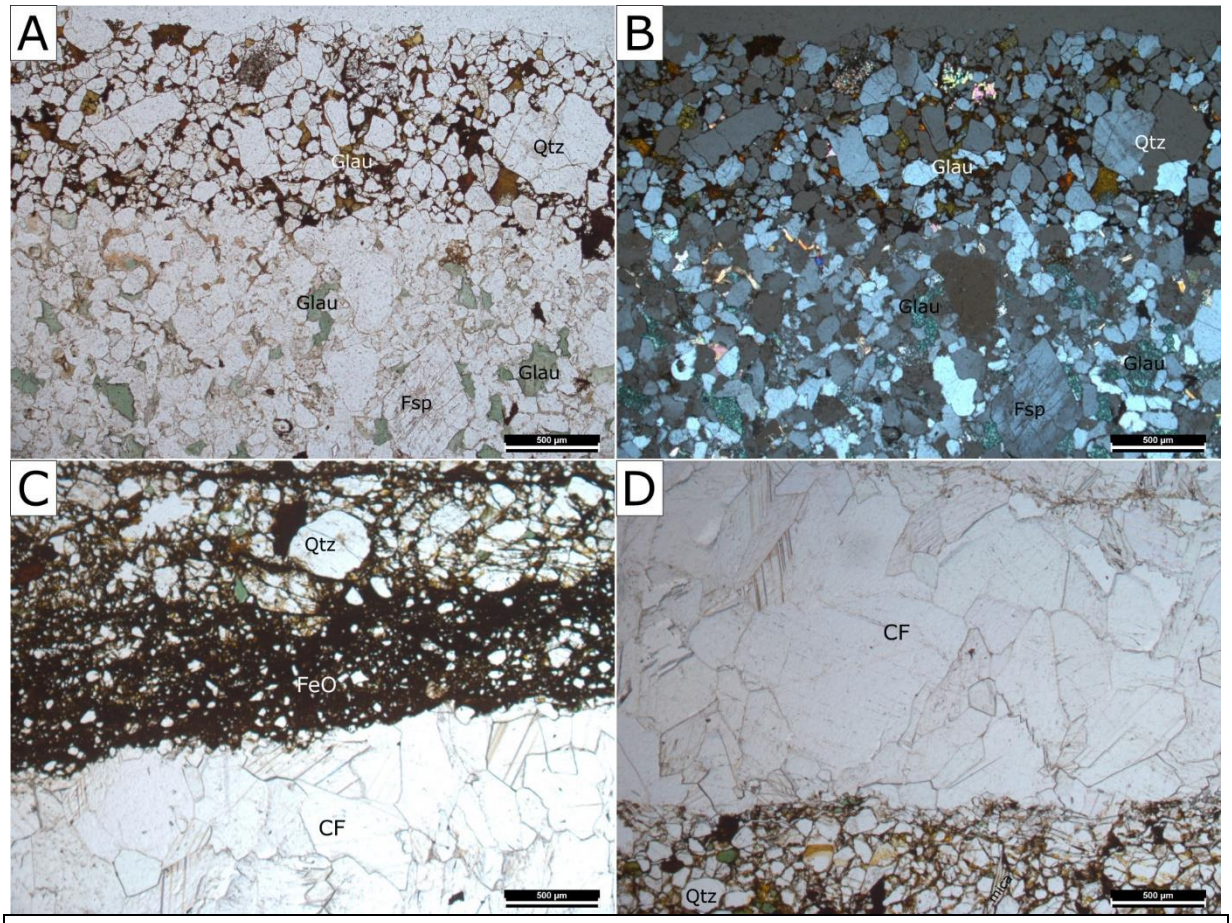

Fig. 40 **(A-B):** Photomicrograph of the iron crust of sample M3 (PPL), B with crossed polars (XPL). **(C):** On the upper edge of sample GR1a_II (the calcite fibre), a dense crust is preserved, with little grains of quartz and other minerals *"swimming"* in it, but without a trace of iron oxide minerals **(D):** sample GR1a_II: below this calcite fibre, the rock is encrusted with iron. The dimensions of it can be seen in Fig 13A. Here the joint was filled with fibrous calcite, preserving the dense iron crust.

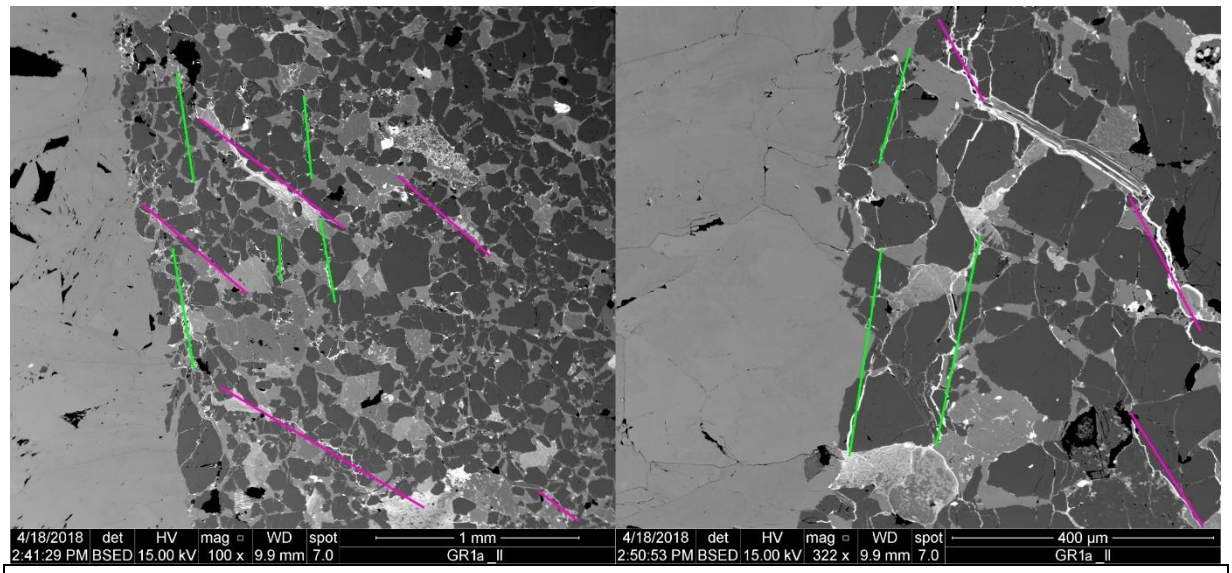

Fig. 41 The iron crust and grain fractures have at least two directions in sample GR1a_II (marked green and purple).

4.2.5. XRD

XRD analyses of eleven samples confirmed the mineralogical composition identified in thin sections and gave further information about the mineralogy of the conglomerates, finely-grained clay minerals and the iron crust. Bulk mineralogy is similar in all samples, both in the sandstones and in the conglomerates.

A comparison of the mineralogy of the host rock and the corresponding iron crust is shown in Fig. 42 to Fig. 44. Minerals which are present in all samples except M13 are quartz (with the highest intensity), muscovite/glauconite (mica group!), microcline (=K-feldspar, $KAlSi_3O_8$) and calcite ($CaCO_3$). The red crust, which was separated from the host rock, contains traces of goethite (FeO(OH)), whereas the host rock shows traces of chlorite and/or kaolinite (Fig. 42-Fig. 44). The greenish sandstones without crust, M22 and M24, show similar mineralogy to the host rocks M26, M8 and M10. M22 contains more calcite (CC). They also contain chlorite and kaolinite (Fig. 45). Sample M16 (Fig. 46), which is a conglomerate, contains no chlorite/kaolinite (chlorite group $(Fe,Mg,Al)_6(Si,Al)_4O_{10}(OH)_8$; Kaolinite $Al_2Si_2O_5(OH)_4$). Some samples, like M8 or M25 and M26, have lower calcite peaks, this can be explained by less calcite cementation as seen in thin sections of M8 (Fig. 42, Fig. 44, Fig. 45). Sample M13, which consists of a thick red coating around a clayey to silty sediment layer within the conglomerate beds, has abundant quartz, rhodochrosite and goethite. It also shows traces of glauconite/muscovite and siderite (Fig. 47). Glauconite and muscovite, as well as chlorite and kaolinite, have a quite similar Θ-value; and thus, the peaks at about an angle of 8.8° (2Θ) can be either muscovite or glauconite, and at about 12.4° (2Θ) can be either a chlorite minerals or kaolinite, as they both occur in the samples. In some samples, chlorite is confirmed by a low-intensity peak at 6.3° (2Θ).

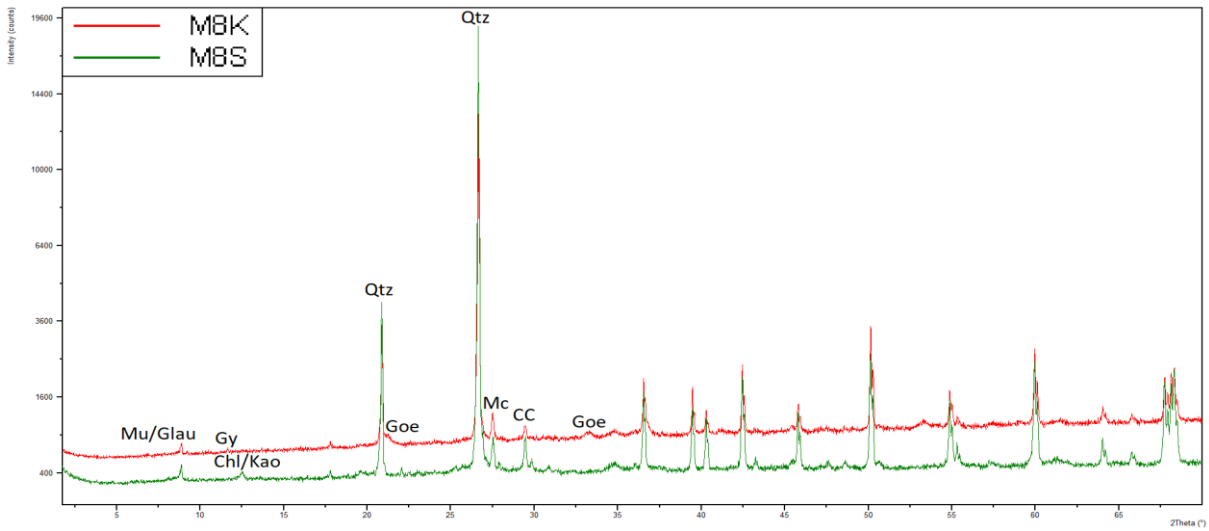

Fig. 42 The mineralogy of the host rock (M8S, green x-ray diffraction pattern) and crust (M8K, red pattern) of sample M8. Both contain quartz (Qtz), calcite (cement) (CC), muscovite or glauconite (Mu/Glau) and microcline (Mc). Minerals only found in the crust are traces of goethite (Goe) and gypsum (Gy), the host rock chlorite or kaolinite (Chl/Kao).

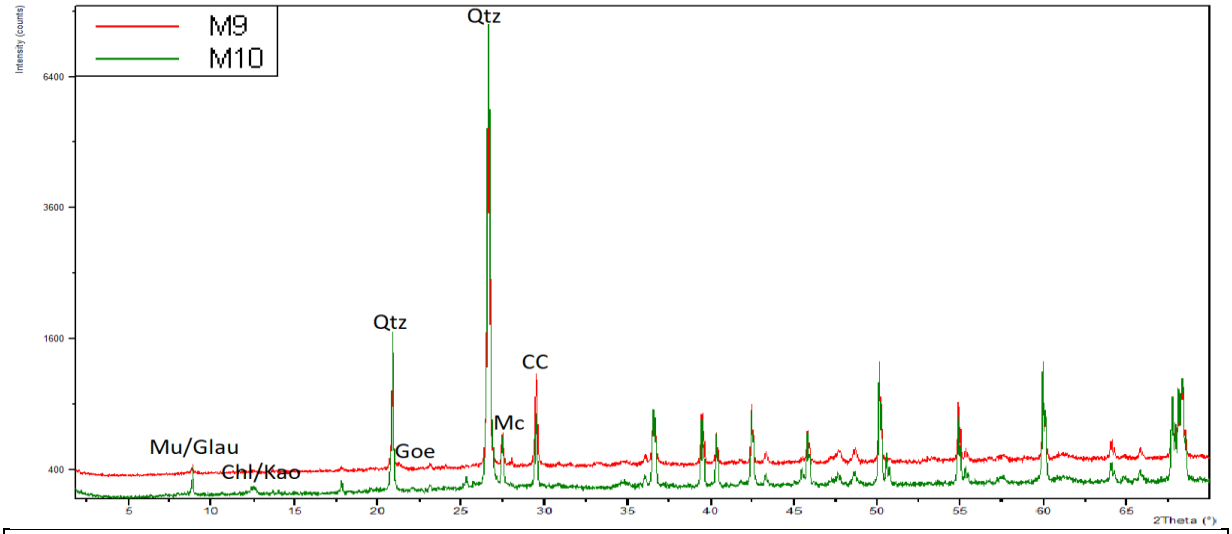

Fig. 43 The mineralogy of sample M9 (crust) and sample M10 (corresponding host rock). Goethite (Goe) is found in the crust and chlorite/kaolinite (Chl/Kao) in the host rock.

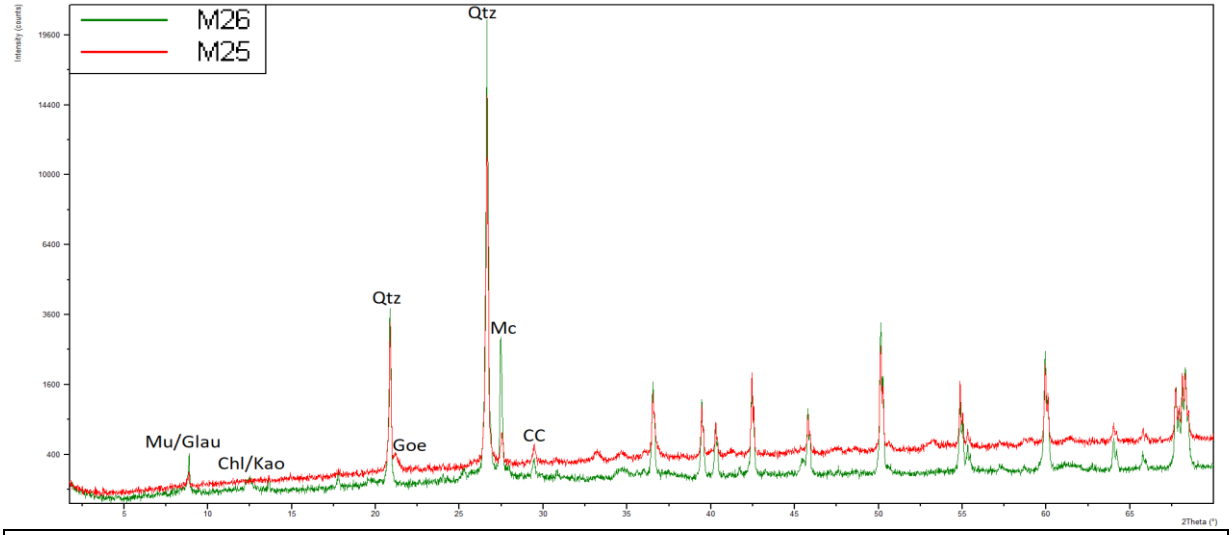

Fig. 44 A comparison of sample M25 (crust) and M26 (host) shows that the iron crust additionally contains goethite (Goe) next to quartz (Qtz), muscovite/glauconite (Mu/Glau), microcline (Mc) and calcite (CC), whereas the host rock has chlorite/kaolinite (Chl/Kao).

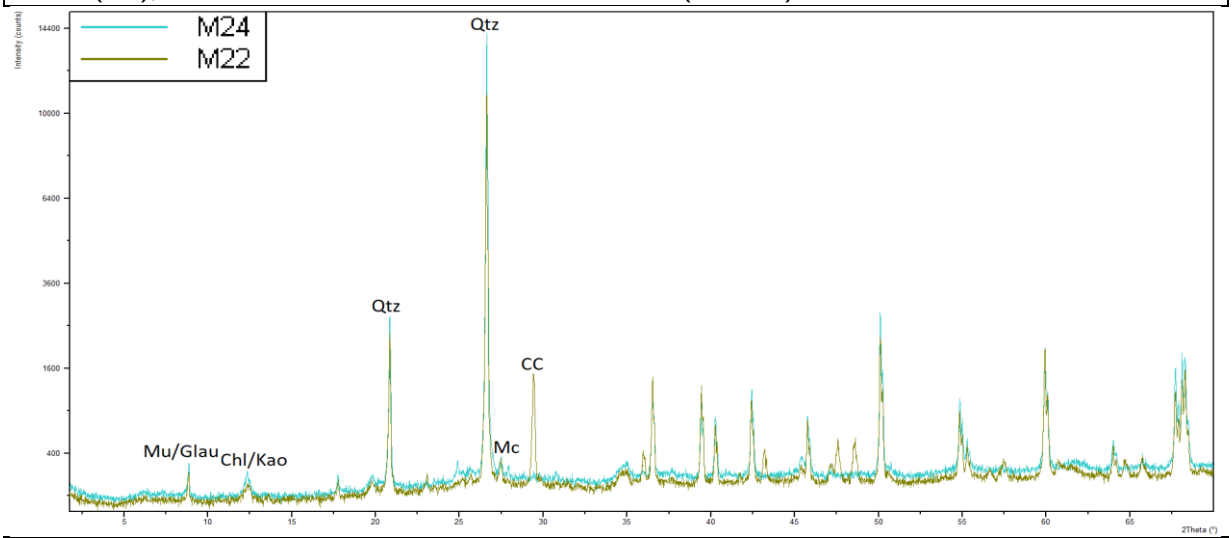

Fig. 45 The greenish sandstones M22 and M24 consist of quartz (Qtz), calcite (CC), muscovite/glauconite (Mu/Glau), chlorite/kaolinite (Chl/Kao) and microcline (Mc).

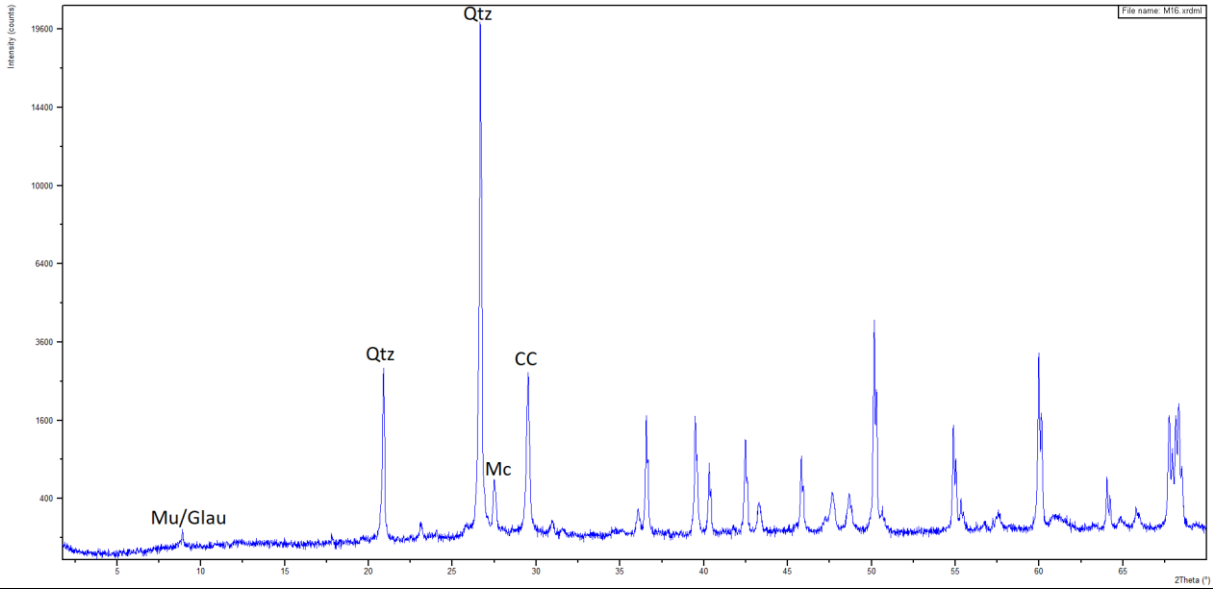

Fig. 46 Sample M16 contains abundant quartz (Qtz) and calcite (CC), some microcline (Mc) and muscovite or glauconite (Mu/Glau).

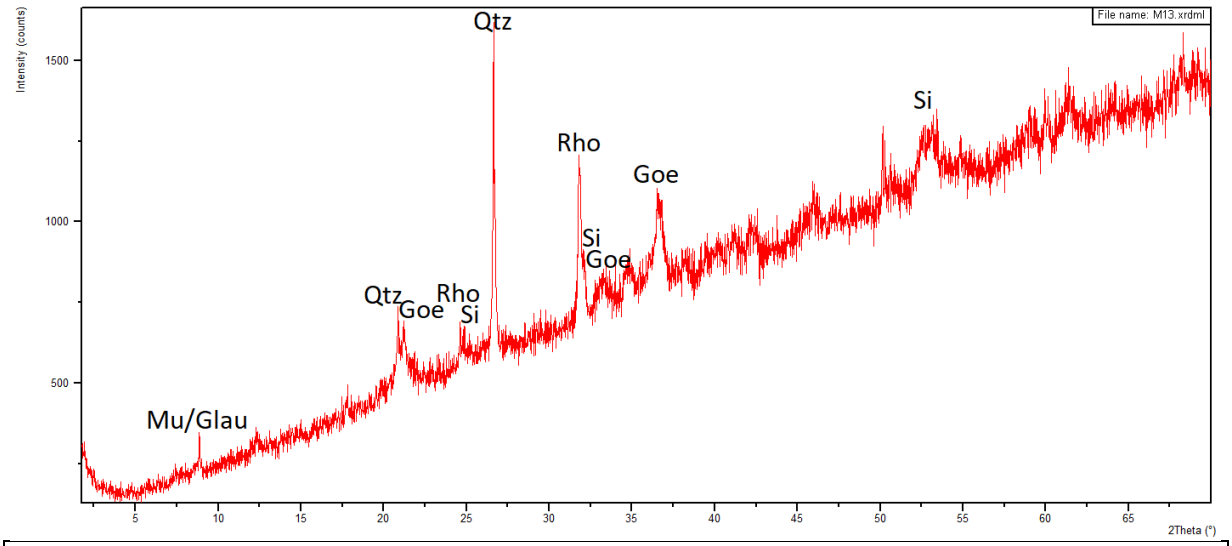

Fig. 47 M13 consists of quartz (Qtz), muscovite/glauconite (Mu/Glau), goethite (Goe), rhodochrosite (Rho; Mn[CO3]) and siderite (Si).

4.3. CL

Thin sections GR1c_I and GR1c_II from sample M1 were analysed. Colours emitted in CL are a bright blue to violet from one mineral and a copper orange from another. Neon green dots are scattered all over the thin sections. Sometimes other colours appear. The rest of the analysed area remains black (Fig. 48). With transmitted light microscope imaging, the blue minerals can be identified as feldspars, the copper orange

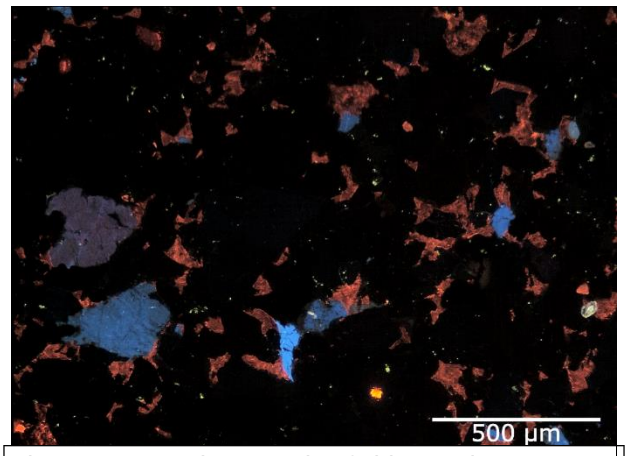

Fig. 48 A CL photograph of thin section GR1c_I. Feldspars are blue; calcite cement is copper orange.

are calcite cement and non-luminescent minerals are quartz.

Copper orange calcite cement in areas with iron crust looks similar to calcite cement in the host rock. This orange varies from lighter to darker shades, and rims of the calcite cement in between the iron crust seem to be more diffuse and darker (Fig. 49). Some cements show a zonation (Fig. 50A). The rims of the cement are either sharp or terminate diffusely by getting darker. Feldspars sometimes show concave-convex and rather blurred contacts to the calcite cement (Fig. 50B).

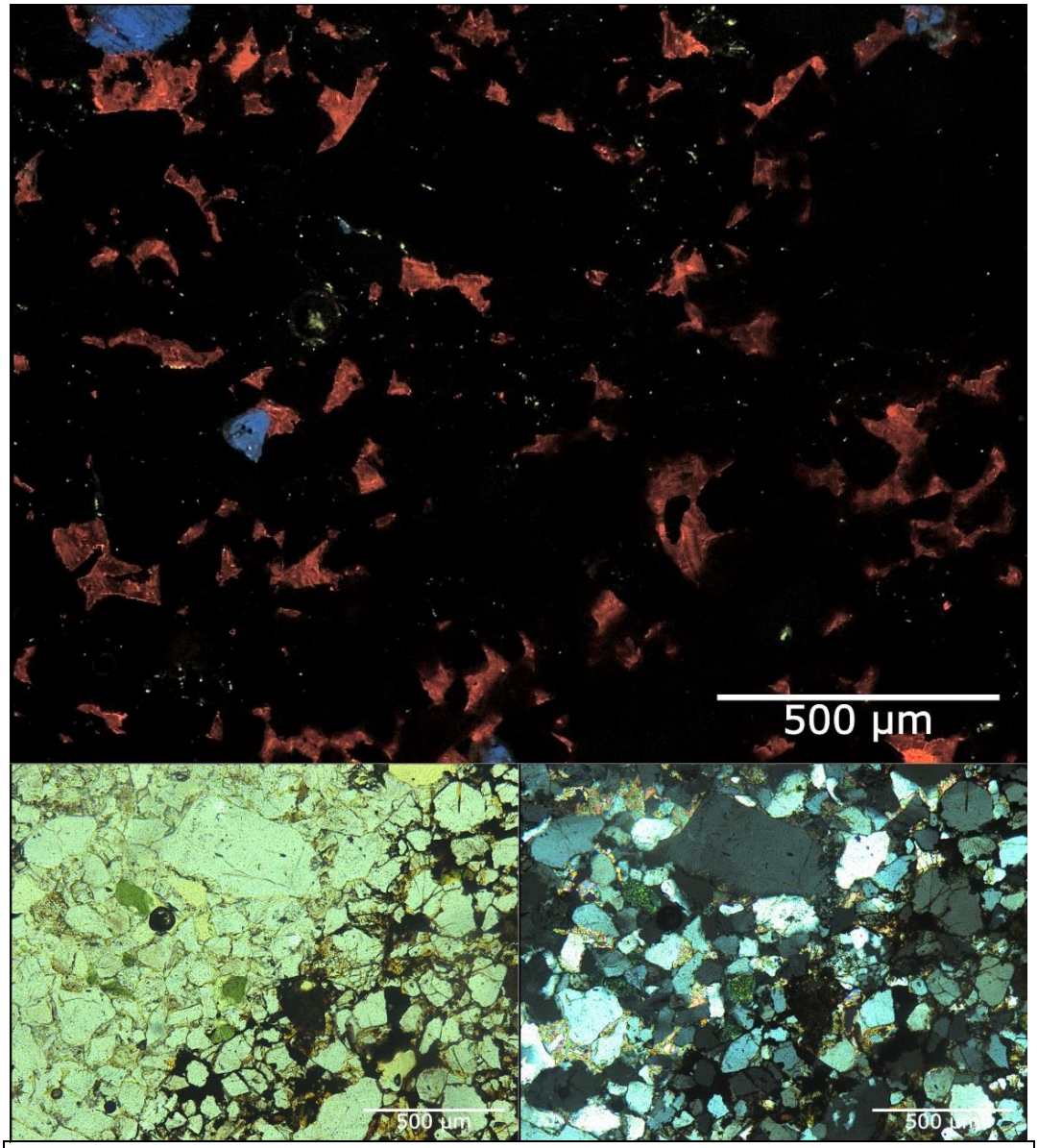

Fig. 49 Thin section GR1c_II; The iron crust (clearly seen in the left lower transmitted light picture, on the bottom right half) has no real effect on the CL of calcite. The colour remains the same, while the rims may be a little more diffuse.

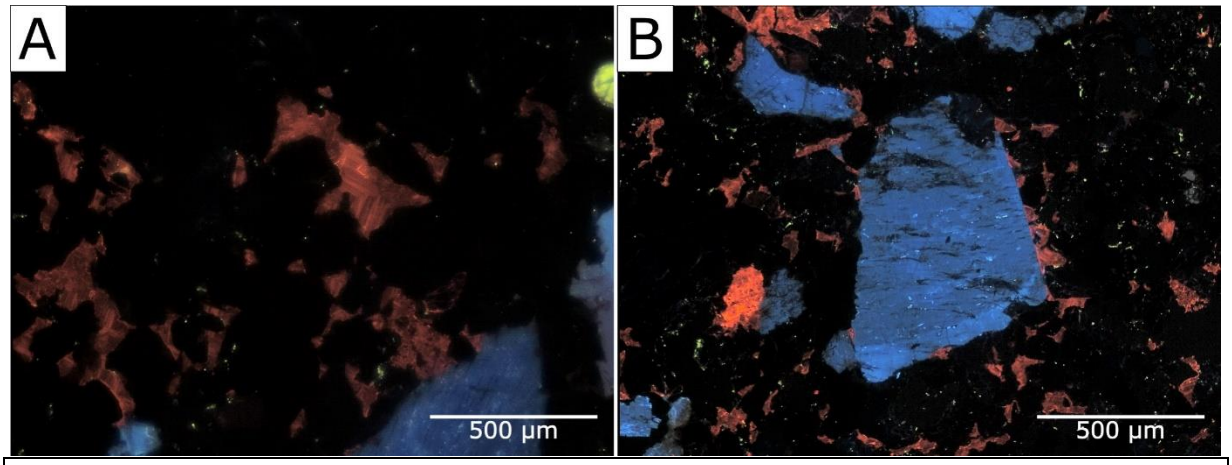

Fig. 50 **(A):** The calcite cement (copper orange) almost in the centre of the picture shows a clear zonation. Other calcites also seem to be zoned, but their CL is more diffuse. **(B):** In CL, the rims of feldspars can be seen clearly: the one in the middle has a sharp, clear, well-crystallized rim on the right side, while it is uneven on the other sides.

4.4. Element analysis

4.4.1. Energy dispersive X-ray spectroscopy (EDX)

EDX was used either to identify minerals using BSEM or to generate element maps of interesting areas of a sample.

In BSEM, minerals are shown in greyscale: the heavier the element composition (i.e., the higher the atomic mass of the elements), the brighter the colour of the mineral. Thus, heavy minerals and the iron crust are white in BSEM pictures. The iron crust was identified as an iron oxide mineral in EDX (Fig. 51). Other *"white minerals"* that were found regularly were identified as titanium oxide (rutile), pyrite and zircon.

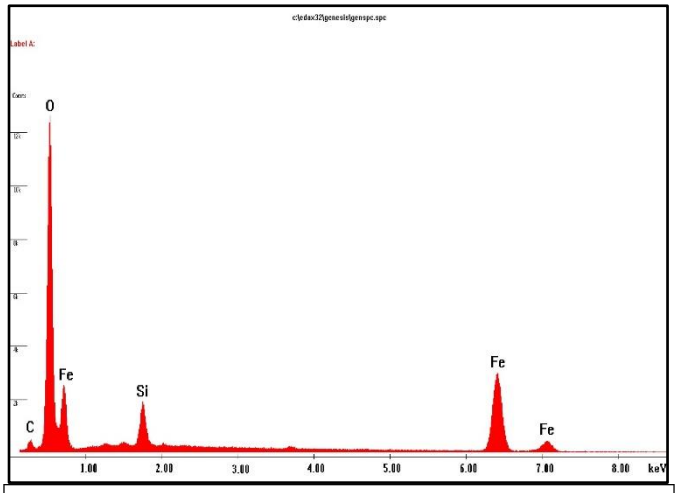

Fig. 51 The iron *"cement"* shows signal of oxygen, iron, silicon and carbon. As the concretion is very thin, the silicon can be a signal from the surrounding quartz, and the carbon from calcite.

The element distribution of K, Al, Na, Mg, Ba, Fe, Ca, Mn, Si, S and Zr showed differences following grain boundaries when being mapped. K, Al and Na are high in minerals like muscovite, feldspar and glauconite. Ba is enriched at the rims of feldspars. Mn, S and Zr are higher in the area of the iron impregnation (Fig. 52), which could provide important information about the origin of the crust. Interestingly, Mg is enriched in sample M4 in the corroded idiomorphic grains of the host rock, whereas it is depleted in the idiomorphic grains in the region of the iron crust. There, the grains show just a signal of Fe (Fig. 53).

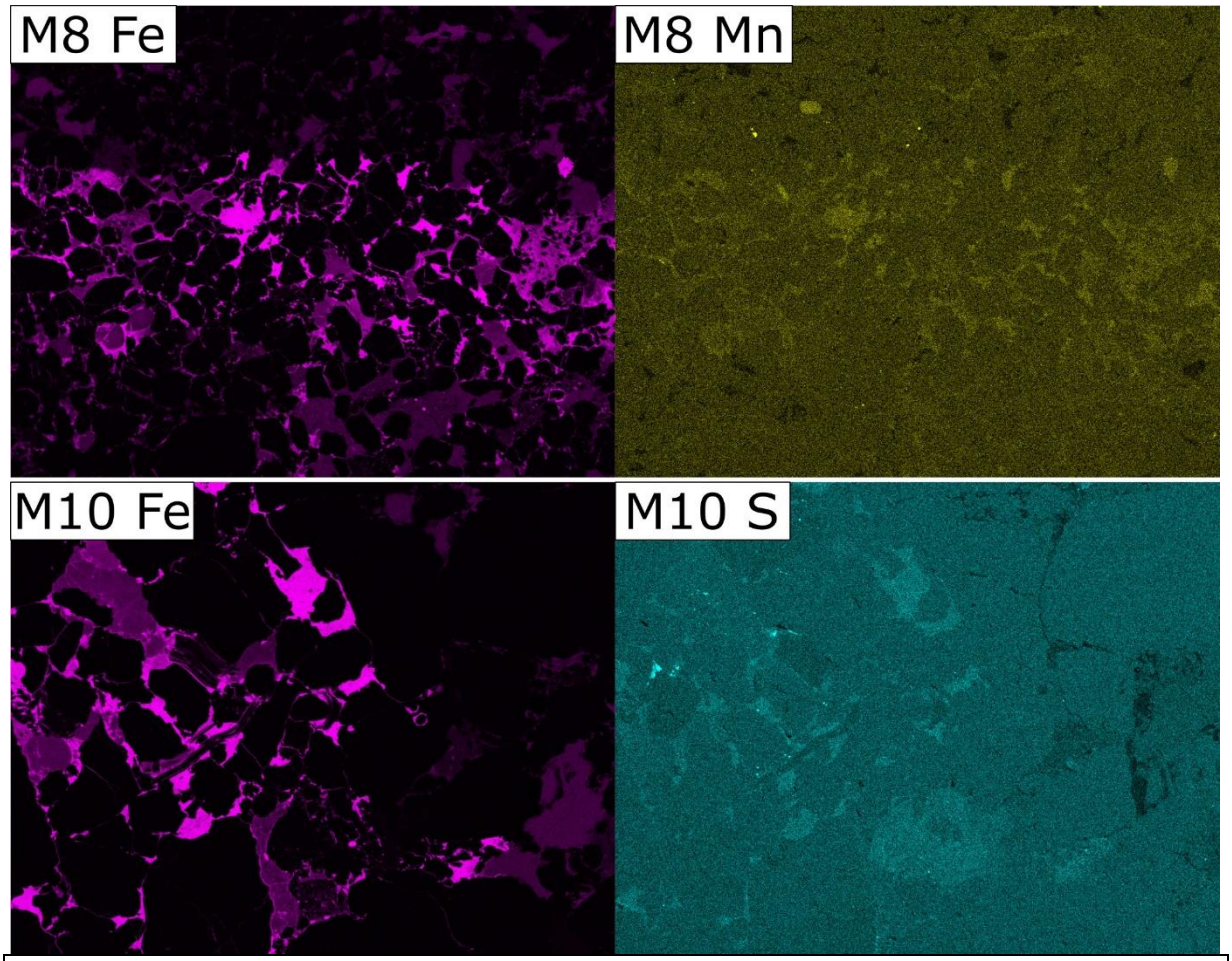

Fig. 52 Element maps by EDX of iron, manganese, and sulphur of a selected area with iron crust of thin sections M8 and M10. Shading is derived from variable element concentrations. There is a significant signal of manganese (yellow) and sulphur (cyan) at the area of the iron crust (iron = purple). This figure shows it is generic in samples M8 (upper two pictures) and M10 (lower two pictures).

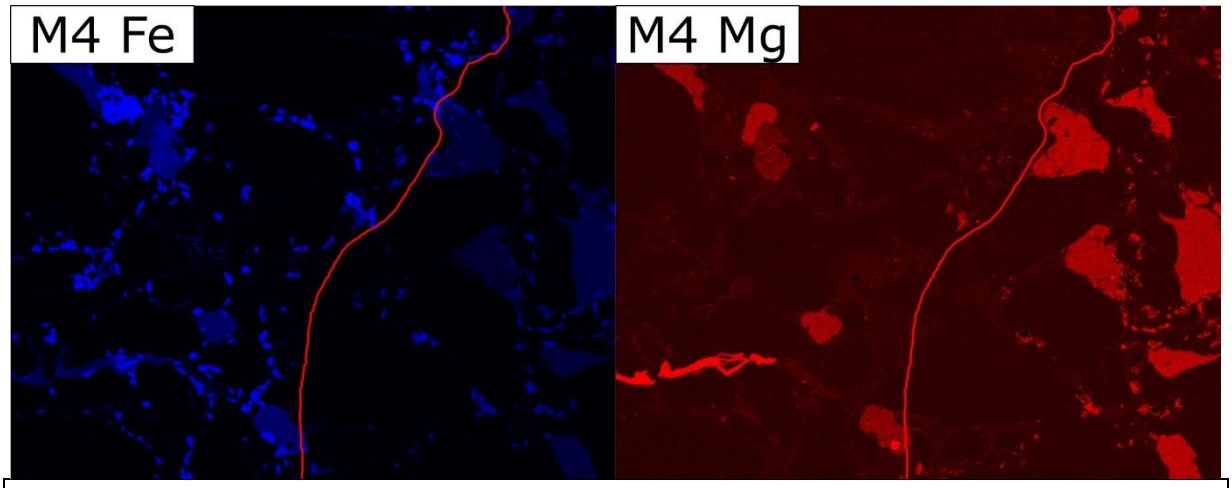

Fig. 53 Element maps of iron and magnesium in the transition area between the iron crust and host rock of sample M4. Emphasis is on the little blue and red grains in the pore space. These grains are whole in the crust area (left of the red line) but seem *"damaged"* and very porous in the host rock area (right of the red line). The signal of magnesium (red) is intensified in the small *"damaged"*, very porous grains outside of the iron crust. They show a bright signal of iron (blue) in the area of the iron crust (left of the red line) and also in the damaged grains, but there the colour is subdued.

4.4.2. Electron micro probe (EMP)

Samples Gr1a_II, M2 and M4 were investigated by point measurements using the EMP.

In sample Gr1a_II, the differences in the chemical composition of calcite cement and calcite fibres were measured. Compared to cement, calcite fibres are low in magnesium, iron and manganese and higher in strontium and barium (Fig. 54). The concentration of iron in the iron cement was about 70% and about 4% Si (Fig. 55). The composition of a glauconite grain in the host rock vs. a glauconite grain in the region of the iron crust is similar.

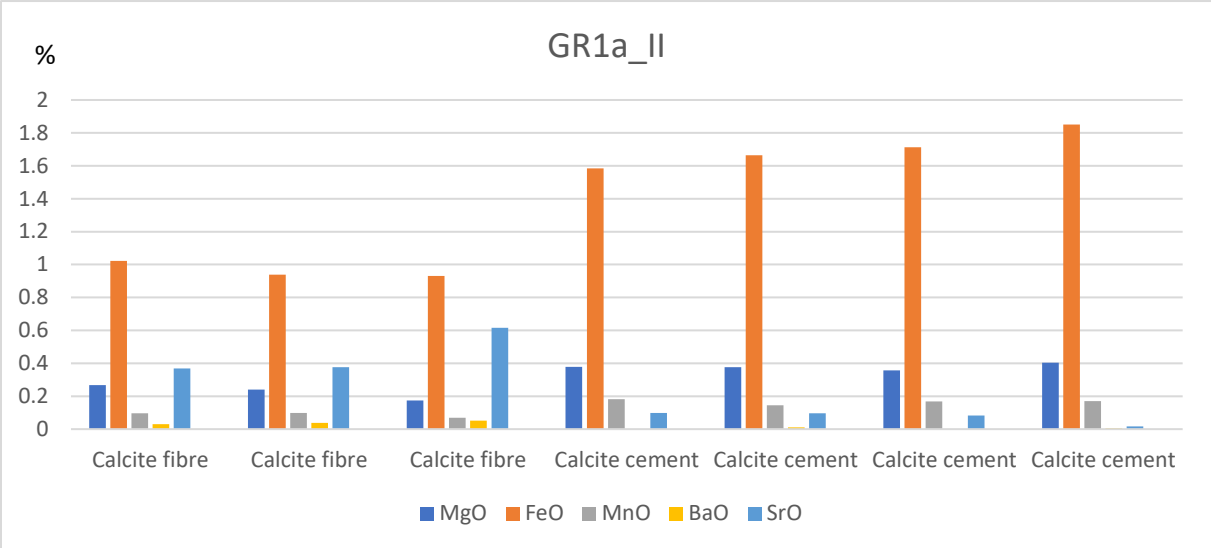

Fig. 54 The composition of calcite fibres versus calcite cement shows distinct differences. The content of strontium and barium is higher in the fibres, whereas the content of magnesium, iron and manganese is higher in the cements. Iron is almost double in the cements compared to the fibres.

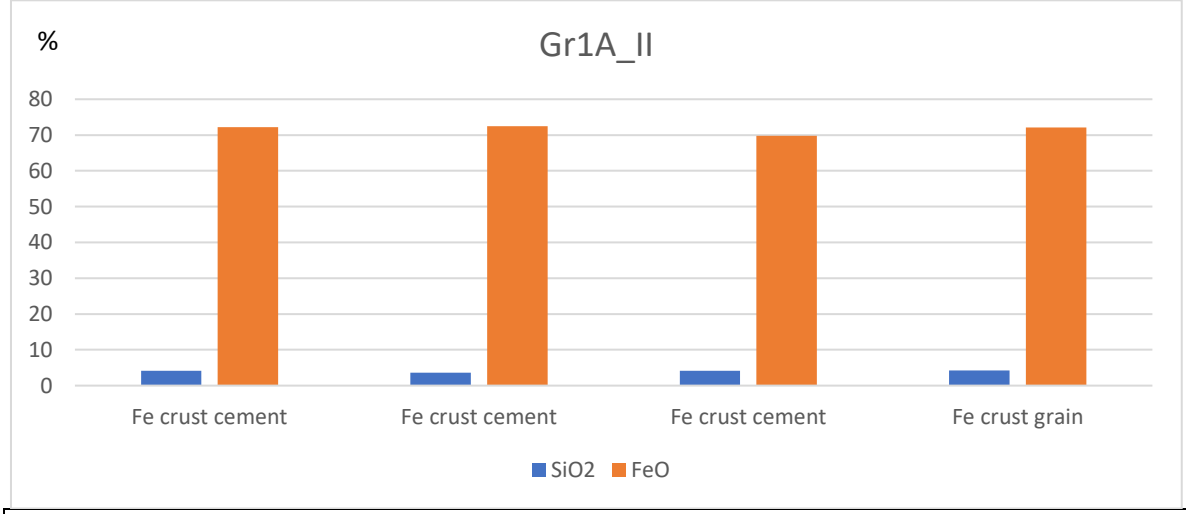

Fig. 55 The iron crust consists of about 70% FeO. There is also a significant signal of silicon, which could come from the surrounding quartz.

A comparison of the composition of calcite fibres and calcite cements in sample M2 is similar to the results of Gr1a_II, although some measurements were not as clear in this sample. Four points in a line from the outer rim of the calcite fibre to its contact with the rock were measured

in two traces close to each other. The iron content decreases to the middle and then increases again, with the highest concentration at the inner edge (Fig. 56).

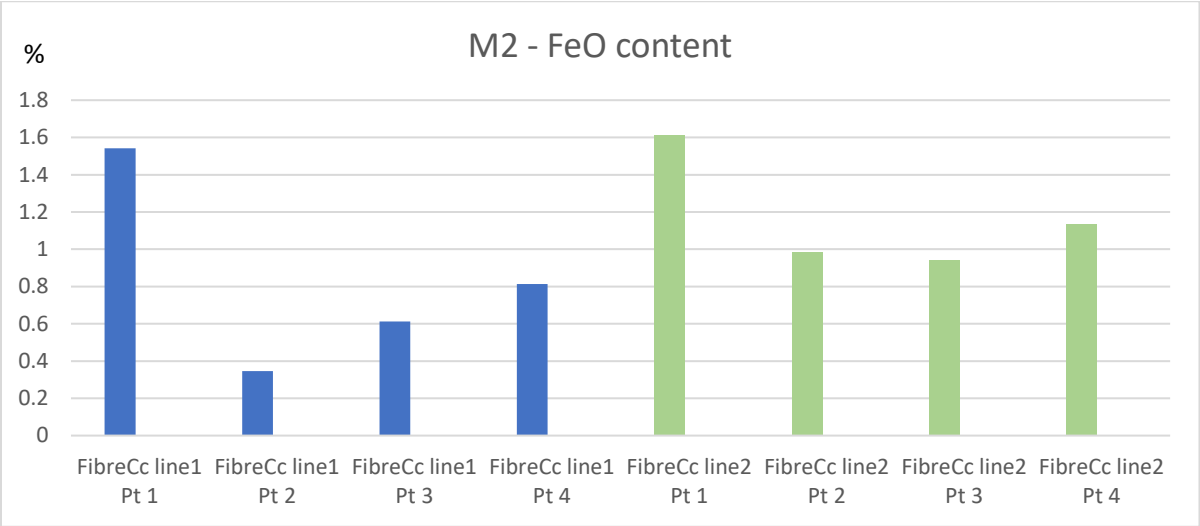

Fig. 56 The iron content of the calcite fibres increases from the centre to the edges, with the highest iron content where the fibre meets the rock.

In thin section M4_2B and M4_1 the concentration of elements in the regions of the iron crust and the host rock were measured. Additionally, M4_1 has a region of *"crust diffusion"*, where the rock is stained in a lighter iron red 2 cm further into the rock. This region was also measured. Three to four measurements were made in each region to detect potential variability, but each showed similar results. There are distinct differences in the concentrations of Mg, Ca and Fe when comparing the host rock to the iron crust with higher iron in the crust, and higher Mg and Ca in the host rock. (Fig. 57)

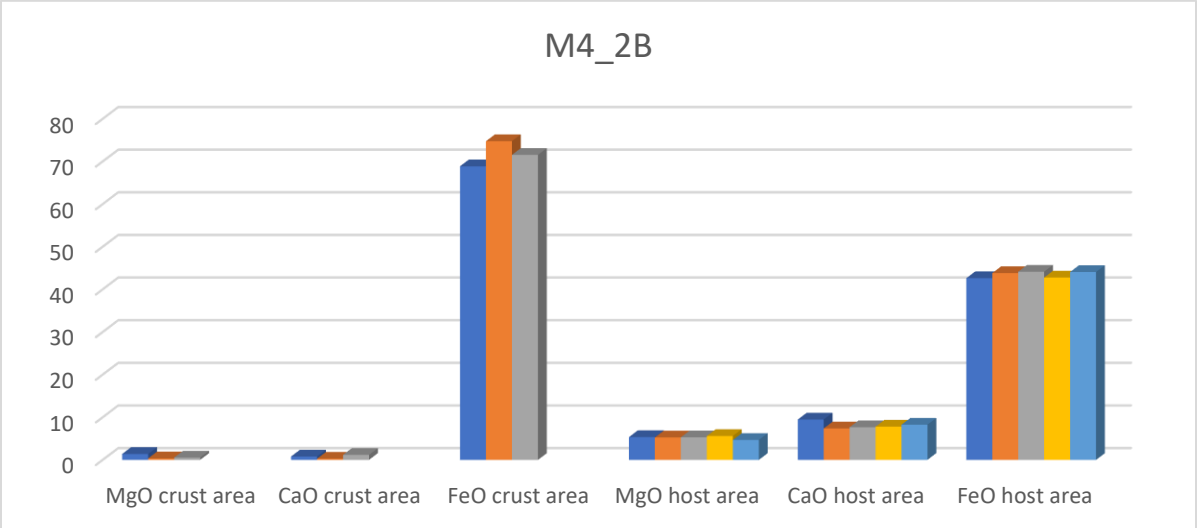

Fig. 57 Three points were measured in the crust area (left) and four in the host area (right). The content of magnesium and calcium was lower in the crust area, whereas the iron content was lower in the host area.

As these are the only measurements that were made with EMP, and more data would be needed for a valid scientific result, further investigations are certainly warranted.

4.5. Porosity and Permeability

Measurements with the Coreval 700 device derive an initial porosity (φ_o) of about 5% (Table 1). Furthermore, permeabilities and porosities of the samples at different confining pressures were measured. Measurements at 400 Psi, 500 Psi and 1000 Psi, with 400 Psi corresponding to an overburden of about 100m rock, are shown in Table 2. Permeabilities at 400 Psi vary between 0.01 and 0.03mD. At 400 Psi, sample GS1, which has an iron crust in the middle, has a 10% higher porosity than sample GS3, whereas initial porosity is 25% higher. Permeability at 400 Psi of GS1 is 25% lower than in sample GS3. The Coreval7 only provided values of 1000 Psi for sample GS2. By gradually increasing the pressure to a maximum of 6500 Psi and then lowering it again, it can be determined whether permeability and porosity of a rock is sustainably altered after burial and subsequent uplift. Permeabilities as well as porosities of the samples did not reach their initial values after applying a maximum pressure (Fig. 58, Fig. 59).

Table 1 Initial Porosities:

Sample No.		GS1	GS2	GS3
φ_o(%)		5.7348	4.1998	4.3223

Table 2 Measurements of the Coreval 700 at distinct pressures from 400 to 1000 psi:

Sample No.	Pc(psi)	≈p (bar)	Kg (mD)	φ(%)
GS1	400	30	0.027941	3.9479
GS1	500	35	0.022210	3.8760
GS1	1000	70	0.011591	3.7303
GS2	1000	70	0.018677	3.5157
GS3	400	30	0.034925	3.6108
GS3	500	35	0.031594	3.5414
GS3	1000	70	0.023799	3.2718

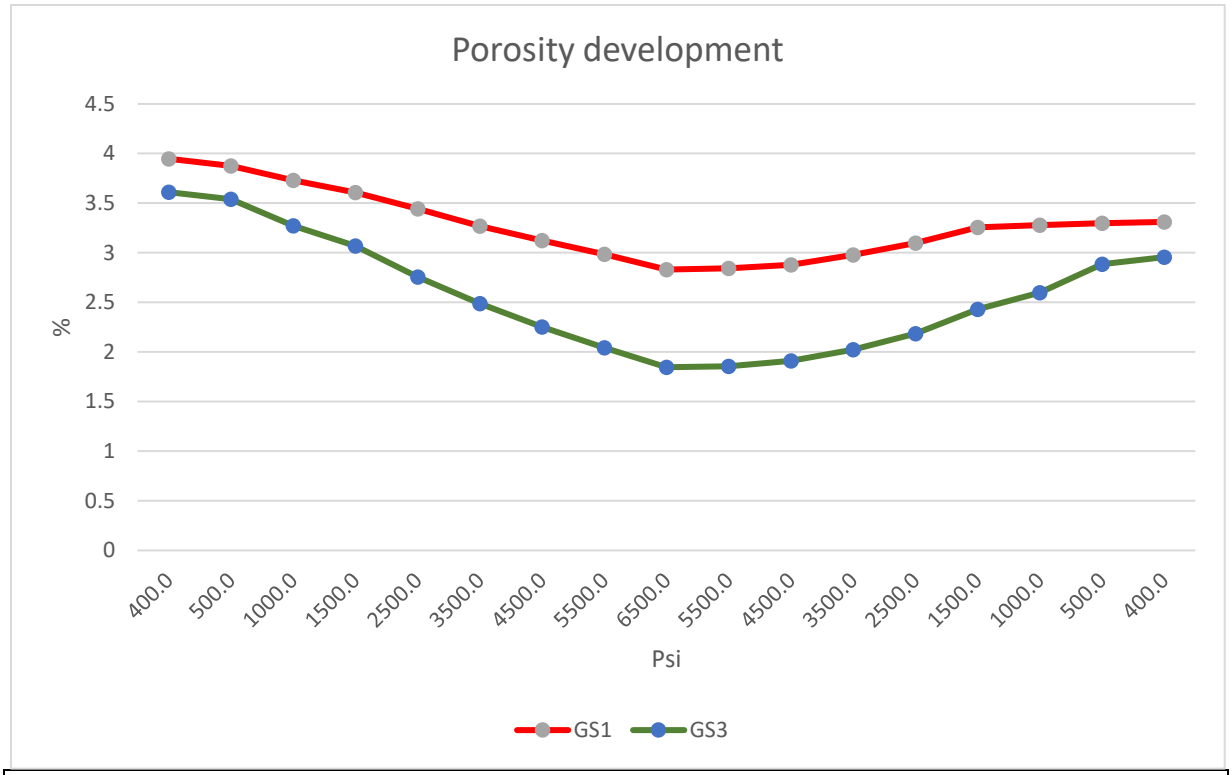

Fig. 58 Porosity development of samples GS1 and GS3 when pressure is increased to a maximum of 650 Psi and decreased to 400 again. Porosities increase when pressure is lowered again, but do not reach their initial value.

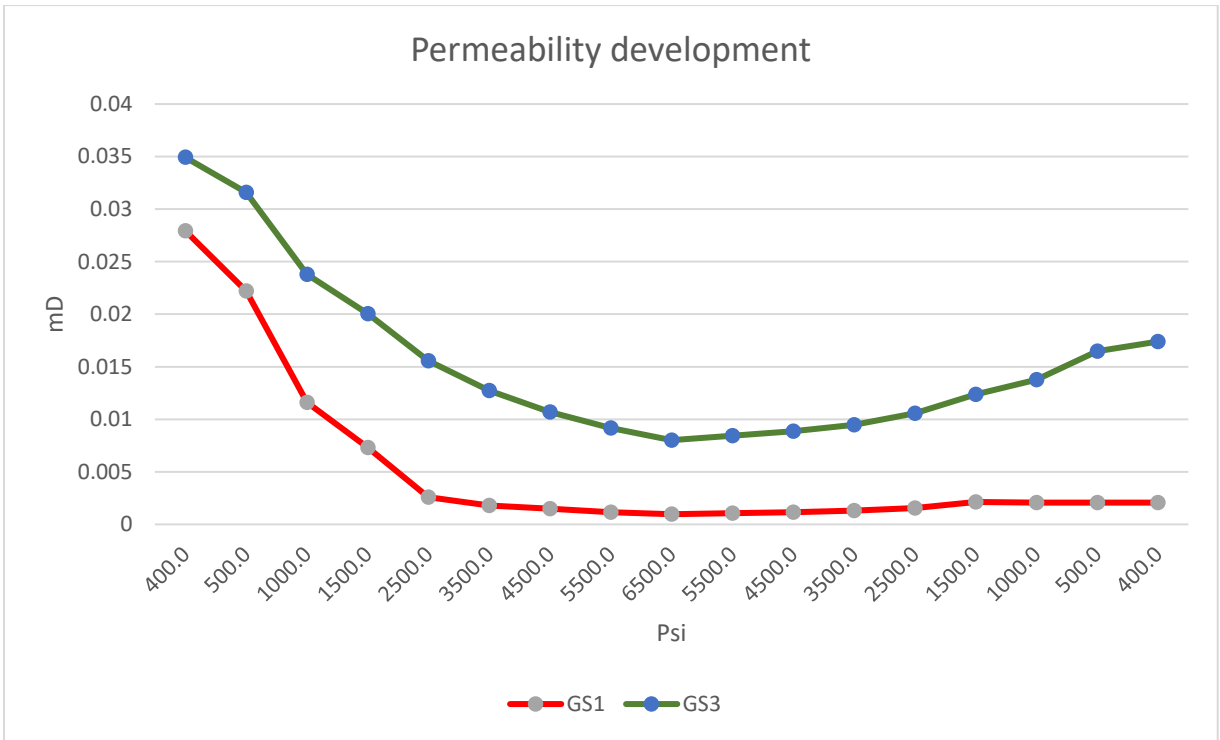

Fig. 59 Permeability development of samples GS1 and GS3 when pressure is increased to a maximum of 650 Psi and decreased to 400 again. Permeabilities are more sustainably altered than porosities: the permeability of sample GS3 increases when pressure is lowered again, but only reaches ½ of its initial value, whereas permeability of GS1 almost does not increase anymore.

5. Discussion

5.1. Structural interpretation

The presence of the iron crust on all four fracture sets (Fig. 16) shows that the iron was precipitated after the sandstone was fully fractured.

In all investigated outcrops (1-4), at least some structures can be linked to deformation in unconsolidated sediment. Pseudo-laminations (sub-)parallel to faults or fractures in Outcrop 1, 2 and 4, occurring in the sandstone beds as well as in the lower conglomerate beds, either originate from deformation bands or can result from the escape of pore water during faulting. Deformation bands are restricted to highly porous granular media, notably porous sandstones (Fossen, 2016). Mass flow sediments of deep marine basins are also prone to soft sediment deformation.

In Outcrop 1, the weathered, relatively unconsolidated layer of clay, silt and sand in between the beds is interrupted by the massive sandstones with a seemingly erosive basis (Fig. 20, Fig. 24). The thin intercalations of greenish, glauconitic sandstones found in Outcrop 3 and 4 could either be big rip-up clasts or the remnant of a sediment layer impacted and eroded by a turbidite flow. (Fig. 28, Fig. 31). Abundant amalgamations are described by Besada (1996). These amalgamations, although not immediately obvious, were also found at the described outcrops. There are remnants of these intercalation-sediments in between the turbidites just next to the intercalations (Fig. 28). Due to these and the amalgamations, the intercalations are interpreted to be autochthonous. The abundant rip-up clasts are possibly from autochthonous Bouma E or from the turbidite (Bouma D) and amalgamated sedimented clay-rich layers of Bouma E. Bouma D and E represent the final and slowest stage in the Bouma sequence and have undergone such frequent erosion following turbiditic currents that they are preserved only as rip-ups. Lithologically, the rip-ups and autochthonous layers are often very greenish, glauconite-rich green rocks. The fine-grained clasts in contact with coarser clastics frequently develop iron-red rims (Fig. 14). The hanging conglomerate beds formed load structures eroding the glauconitic sandstones. Fractures originate from the greenish layer in Outcrop 3, suggesting their formation in unconsolidated sediment.

The evidence of either deformation bands or water escape structures and fractures originating at bedding planes are indicators of deformation and formation of fractures in unconsolidated sediment. Calcite fibres and striations on fractures are a sign of brittle deformation, which may have happened in the course of the alpine orogeny, when the rock was fractured another time.

5.2. Petrographic interpretation

The composition of the samples, as well as the petrographic and textural features, provide a good insight into the diagenetic and sedimentary history of the rocks of the Greifenstein Formation.

Bent micas and brittle grain fracturing are a sign of mechanical compaction. While chemical compaction happens during mesodiagenesis, mechanical compaction can happen anytime, with ductile compaction of soft grains normally shallower than brittle compaction of harder grains (Worden & Burley, 2003). Microscopically-fractured grains are more abundant at the sandstone rims (macroscopically: close to a discontinuity), which is a feature of deformation bands and indicates solid correlation with the structural interpretation before.

Clay cements/clasts in sample M8 or M10 are interpreted as a result of chemical compaction. Clay-rich rock fragments are deformed and smeared into pores as a result of compaction. Detrital mud clasts transformed into intraclasts during mesodiagenesis are typical for turbidites (Worden & Morad, 2003). Calcite cements can develop during eodiagenesis as well as burial diagenesis when dissolved and reprecipitated.

During mesodiagenesis, the porosity of arkosic sandstones with some clay is reduced to less than 10% according to Worden and Burley (2003). This is in good accordance with porosity values of our samples (φ_o=4-6%, cf. chapter 4.5). Deformed grains, like bent micas and quartz overgrowths, play an important role in reducing porosity and permeability (Worden, et al., 2000). Porosity values, as well as the grade of compaction of the sediment, fit well with the burial depth data of Trautwein et al. (2001). Porosities of less than 10 percent and brittle compaction are typical for burial to depths shallower than 5km (Worden, et al., 2000). The impact of the iron crust on porosity seems to be negligible, whereas permeability was reduced more significantly (by 25%) (0.035 mD at GS3 without crust, 0.027 at GS1 with crust) (cf. chapter 4.5). Earlier, (unpublished) measurements also showed a reduction of permeability by 50% (Neuhuber, 2013). This reduction of permeability may have a negative impact on the reservoir quality of the sandstones of the Greifenstein Formation. As only 3 measurement series of one sample were made here, further investigations on the impact of the iron crust on porosity and permeability and the resulting reservoir quality of the sediments are suggested at this point.

Zircon is the most abundant heavy mineral, followed by tourmaline and rutile (Hösch, 1985; Besada, 1996). Comparing the heavy minerals found in the samples with transmitted light microscopy and SEM with these earlier investigations, zircon and rutile can be confirmed, whereas tourmaline was not found in the samples of this study. Another abundant heavy mineral found in the samples of this study is pyrite. Zircon and rutile are both stable minerals,

which indicates that the source area lacks unstable minerals, or the unstable minerals were dissolved during diagenesis. Besada (1996) concluded from this fact that the sediment was very likely derived from a continental platform. Together with paleocurrent analysis, which revealed a provenance from the north-west, the source of the Greifenstein sediments was interpreted to be the Bohemian Massif. They were first deposited as shelf sediments in the Penninic Ocean and then redeposited by turbidity currents. Pyrite probably formed in a diagenetic, synsedimentary fashion, so it is presumed to be authigenic.

5.3. Features of the iron crust

The iron crust does not continuously cover all fracture planes, possibly because exposed planes are weathered, and parts of the crusts are exfoliated by weathering. The iron also may not have reached every single spot of a fracture. The iron crust is mainly restricted to the massive sandstone beds in the middle section, while crusts neither occur on the thinner bedded finely-grained sandstones in the hanging section nor form real crusts in the conglomerates. This grain-size dependent appearance may be explained by the fluid not being able to permeate into the finer-grained sandstones, whilst it may have just rushed through the quite permeable conglomerates and hence was unable to precipitate any iron oxides.

Sample M4 contains small, enigmatic brown idiomorphic grains which are rich in Mg and Fe. These are quite porous and fragmented in the host rock area, but are structurally sound in the crust area and only contain Fe (cf. element maps chapter 4.4.1). The signal of Mg in the host rock area was also detected with a microprobe (Fig. 57). In this sample, the small iron grains are responsible for the red colour of the iron crust. The grains in the host rock could be the remains of ankerite, which was partially dissolved during diagenesis or the result of subsequent weathering. In the crust area, the iron-rich fluid may have precipitated at the position of the small grains, resulting in particles of siderite or goethite. EDX measurements of other idiomorphic grains in sample GR1b_I and M4-2B show all siderite-building elements, so these grains are possibly siderite.

In contrast to the calcite cements, the calcite fibres are enriched in Sr (Fig. 54). Sr is known to stay in solution, whereas Ca and Mg build minerals faster. Due to this slower mineral-building rate, Sr was incorporated at a much later stage and was hence enriched in the calcite fibres, which formed significantly later than the calcite cement.

The iron crust does not only occur as a crust measuring as much as 3-5mm, but also shows diffusion patterns and ring-shaped patterns. This can be interpreted as a result of weathering and thus Liesegang diffusion.

5.4. Goethite formation

The iron precipitates are present as poorly-crystallized goethite in the form of a pore-filling cement. Goethite formation was studied intensely in several works by Schwertmann and his colleagues in the second half of the 20th century.

Iron occurs naturally in two oxidation states: Fe^{2+} and Fe^{3+}. Iron in red sediment is normally oxidized and present as Fe^{3+} (immobile) and must be reduced to Fe^{2+} or complexed for transport, then oxidized to precipitate as Fe^{3+} minerals (Chan, et al., 2000). In other studied examples of iron precipitates in the form of crusts, concretions and impregnations from all over the world, the actual mineral formed is either goethite (α-$Fe^{3+}O(OH)$) or hematite (Fe_2O_3) (e.g., Chan, et al., 2000; Eichhubl, et al., 2004; Afify, et al., 2014). Hematite is always described as the more reddish phase, whereas goethite has yellow and brown colours (e.g., Beitler, et al., 2005; Cornell and Schwertmann 1996). Macroscopically, the iron crust in the Greifenstein Formation has a pronounced reddish hue, so it is assumed that these samples contain hematite rather than goethite. Whether goethite or hematite precipitation is favoured depends on different conditions:

Both phases are formed from an amorphous precursor phase, ferrihydrite. Whilst hematite is formed by 'internal dehydration' (removal of OH groups), goethite is produced stepwise by a reconstructive transformation involving dissolution and reprecipitation. Both mechanisms operate competitively (e.g. Fischer & Schwertmann, 1975, Cornell & Schwertmann, 1979). In addition, Schwertmann and Taylor (1989) noted that goethite can precipitate directly from solution, whereas hematite requires ferrihydrite as a precursor phase.

Goethite and hematite are stable under different P/T-conditions in the Fe_2O_3-H_2O-system, with goethite being stabilized by increasing pressure and hematite by elevated temperatures (Fig. 60, Majzlan, et al., 2003). The precipitation of goethite is also favored

- at low temperatures
- at high Al and H_2O activities
- at low pH of about 4 and high pH of about 12 and at conditions resutling in lower/changing pH such as
    - at higher organic content (lowering the pH)

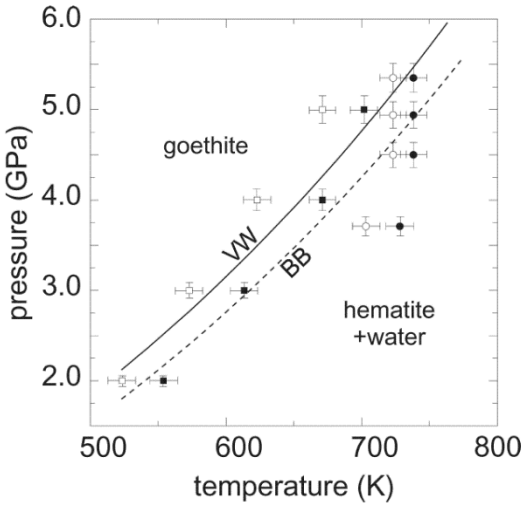

Fig. 60 Stability diagram of Majzlan, et al. (2003) derived by combining data of two authors (VW-Voigt and Will (1981) and BB-Baneyeva and Bendeliani (1973)). Goethite is stable at elevated pressures, while hematite is stable at elevated temperatures.

- in soils (in the B-horizon as a result of changing pH)

(Schwertmann & Taylor, 1989)

To enrich iron oxides, iron needs to be reduced to Fe^{2+} either by reactions lowering the pH or by high pH and resulting in transport. In a second step, it is oxidized for mineral precipitation. Iron phases have a very high adsorption capacity for cations; and, once precipitated, they also adsorb Fe^{2+} from the solution, which is then oxidized, resulting in a positive feedback loop. Goethite requires one of the above-mentioned conditions for its precipitation to be favoured vs. that of hematite. Reducing fluids could dissolve and transport the iron. When they come into contact with oxidizing meteoric water, goethite is then precipitated (cf. Chan, et al., 2000). In CL, the border of calcite and iron minerals in sample M1 were diffuse (Fig. 49). The iron seems to have dissolved or superseded the calcite to some extent. This could indicate that iron-rich low pH fluids were intruding into the fractures and dissolved the calcite cement. The dissolution of calcite would work as a buffer and raise pH, which could result in iron oxide precipitation.

The source of iron could either be internal (from the deep-sea mass flow sediment of the quarry itself) or external (from another rock source, e.g., the underlying formations, such as the Altlengbach Formation, formations of the Molasse Zone or the Hauptklippenzone). An internal source would indicate that no significant transport (via fractures) has occurred. Possible internal sources of iron could be:

(A) Glauconites
(B) Pyrites
(C) Ankerite, syndepositional iron oxides

Possible external sources of iron could be:

(D) Iron-bearing minerals of other, non-mass-flow sediments of the quarry
(E) Iron-bearing minerals of other rocks (e.g., from an underlying formation)
(F) Iron-rich groundwater

Below is a more in-depth discussion of each of these six possible sources of iron.

(A): Glauconite is formed on marine outer shelves and slopes with reduced oxygen availability, either biogenetically from faecal pellets (colloids) or by glauconitization of Fe-bearing mica or biotite. Its formation starts with the precipitation of Fe-Al smectites, which are gradually enriched in K. (e.g. Odin & Matter, 1981; Zhang, et al., 2017). As the rocks in the study area are quite rich in glauconites, they constitute ideal candidates for a source mineral of iron. When analysed with SEM, glauconites within the host rock mostly do not have an appearance

different from the ones in the rim, but transmitted light microscopy reveals that they are brown and oxidised in the crust area. The chemical and mineralogical composition of glauconites in the host rock does not differ from the glauconites in the crust area. Glauconite will oxidize to kaolinite and goethite in shallow marine, fluvial or paleosoil environments (Huggett, 2013). The oxidation of glauconites could have resulted in goethite formation. Kaolinite was also detected by XRD in most host rock samples. Nevertheless, although not dominant as a percentage, feldspars are ubiquitous in the Greifenstein sandstones, so the presence of kaolinites may also be explained by feldspar weathering during sandstone diagenesis. A significant amount of iron must have been dissolved from the glauconites to form all the iron crusts. This amount would have been removed from the *"host"* rocks and would have changed the overall rock composition. Bleached rocks, rocks lacking glauconite or containing much less of it would be evidence for the mineral as an internal source of iron. For all these reasons, internal glauconite is not considered a good candidate as the source of iron.

(B): Pyrite is the most widespread sulfide mineral in the earth's crust. It can be formed in sedimentary processes during anoxic diagenesis, e. g. in the deep sea (e.g., Berner, 1970; Howarth, 1979). Sulphate reducing bacteria form H_2S, which produces a reducing milieu that favours pyrite formation. It also forms from reactions involving hydrothermal fluids. When pyrite is oxidized in the presence of water, H^+ is released, lowering the pH and simultaneously dissolving carbonates. Pyrites appear at times in the samples (e.g., M1, M3, M4, M8) and constitute another possible candidate for the supply of iron. Pyrite can be oxidized by oxygen and water in two stages. This often happens in paleo-soils and also during acid mine drainage. Many thin sections and samples lack carbonate cement (cf. chapter 4.2.3, e.g., Fig. 36), and it is possible that the cement was dissolved by this H^+. Other iron-encrusted sandstones are indeed well-cemented with calcite. On the other hand, rocks without calcite cement may have been cemented by quartz or clay cements, and not by calcite at all. The EDX signals of Mn and S within the iron crust can be explained by the fact that Mn, S and iron are a group of elements that are mobile under suboxic and anoxic conditions. Pyrite being a source mineral for the iron crust is therefore not very likely, but also not impossible.

(C): As mentioned before, sample M4 differs from other samples due to its abundant idiomorphic Fe-grains. Other samples also have a small number of these grains, at least in the area of the iron crust. Maybe ankerite or another iron mineral was more abundant when the sediment was deposited. This iron mineral was perhaps easily dissolved during diagenesis; then the iron was subsequently enriched in the pore fluids and led to goethite precipitation when the fluids attained oxidizing conditions. A study of turbidites in the Black Sea showed that burial of non-sulfidized Fe phases like goethite is quite common and that its reactivity towards dissolved HS^- is lower than expected (Kraal, et al., 2019). Assuming that goethite is

deposited with deep sea sediments, it may be dissolved by reducing pore waters during burial diagenesis and is reprecipitated when these waters come into contact with oxidizing meteoric water.

(D): The rip-up clasts and autochthonous intercalations of the conglomerates are generally surrounded by iron-red rims. These reaction rims are an indication that the greenish sandstones could be a supply of iron. One of the layers containing more coarsely-grained material surrounded by clay, an iron red rim and iron concretions (c.f. chapter 4.1.4) was investigated in more detail. XRD identified abundant quartz, goethite, rhodochrosite and siderite. The presence of siderite and rhodochrosite indicates meso- to epithermal conditions, which either could have been present in the deep-sea at hydrothermal springs or could have occurred in a syndiagenetic process. The iron-red rim around the rip-ups could have formed in two possible ways: (1) The rip-up itself contained a lot of iron, possibly in the form of glauconite, which was dissolved and reprecipitated as goethite at its rims. (2) The rip-ups worked as a barrier for the iron-rich fluid, and goethite crystallized at the contact surface between the conglomerate and the rip-up. If these fine-grained sandstones and pelites supplied the iron, there should be additional rocks like these deposited somewhere else serving as the source of the entire iron supply. The sediments of Bouma E and D may have contained quite a lot of iron-bearing minerals like the siderite and goethite that were found with XRD in sample M13 (Fig. 47) and glauconites that were found in samples M22 and M24 (Fig. 45). If these iron minerals were dissolved in the early diagenetic history and trapped in pores and discontinuities, they could easily be the supply for the iron crusts. As mentioned above, assuming that goethite was deposited with deep sea sediments, it may be dissolved by reducing pore waters during burial diagenesis and reprecipitated when these waters come into contact with oxidizing meteoric water. These sandstones are considered to be a very likely source of iron.

(E): Iron from rocks in underlying formations could have been dissolved, transported to the sandstones of the Greifenstein Formation and reprecipitated there. Transport of up to several km is quite common and therefore not unlikely. For this hypothesis to be verified, such source rocks must be linked to the quarry by way of chemical analysis; and for this type of analysis, isotope measurements are recommended. Possible source minerals would be the above-mentioned glauconite, siderite, pyrite or goethite, but also hematite. Hematite is known to form iron oxide coatings around sedimentary grains, which are either thought to be the result of early syndepositional diagenetic processes (e.g., Walker, 1975; Eichhubl, et al., 2004; Chan, et al., 2000 (Walker, 1975)) or a product of the weathering of Fe-bearing carbonates, where the Fe-oxide is insoluble and gets left behind.

(F): Groundwater data from the area around the quarry show high iron concentrations (20-100 µg/l] in the Greifenstein Formation. Some values even exceed the admissible concentrations

of the Austrian regulations for drinking water quality (approx. 400 µg/l). Mean values do not show a dependence of these values on lithology (Heinrich, et al., 2007). Iron concentrations of groundwater in Quaternary deposits in this region are even higher (50-500 µg/l) (Heinrich, et al., 2008). In summary, groundwater in this area currently has a high concentration of iron. If this iron is oxidized by a change in water chemistry or through mixing with other ascendant fluids, it can be precipitated as the iron crusts observed in the Greifenstein Formation. Groundwater needs to have a reducing character for this to occur. The iron crusts are often overgrown by calcite fibres and idiomorphic calcite and quartz crystals, so the crusts can't be recent precipitations from groundwaters. Ancient, reducing iron-rich groundwaters, nevertheless, could have been the source of the iron.

5.5. Fluid flow and diagenetic history

The aforementioned features of the rock and iron crust (cf. chapters 5.1 to 5.4) imply the following sequence of events (Fig. 61):

(1) deposition at the shelf and remobilization by slope instability
(2) Sedimentation in the deep sea and thereby the creation of rip-up clasts and erosive (amalgamated) bases
(3) Formation of soft sediment fractures, water escape structures and deformation features like deformation bands
(4) Early diagenetic partial calcite cementation
(5) Burial of the sandstone to a depth of about 5-6 km (Trautwein, et al., 2001), compaction and subsequent bending of micas, fracturing of grains and quartz overgrowths
(6) Uplift, opening of fractures and fluid flow, permeation of fluids into the sandstone and precipitation of iron in residual pore space when the reducing, iron-rich fluids came into contact with oxidizing, probably meteoric water
(7) A probable second phase or multiple phases of shearing, fluid flow and iron precipitation, which explains the different directions of grain fracturing and iron cements
(8) Change of fluid composition, growth of calcite fibres and idiomorphic calcite and quartz on fracture planes.

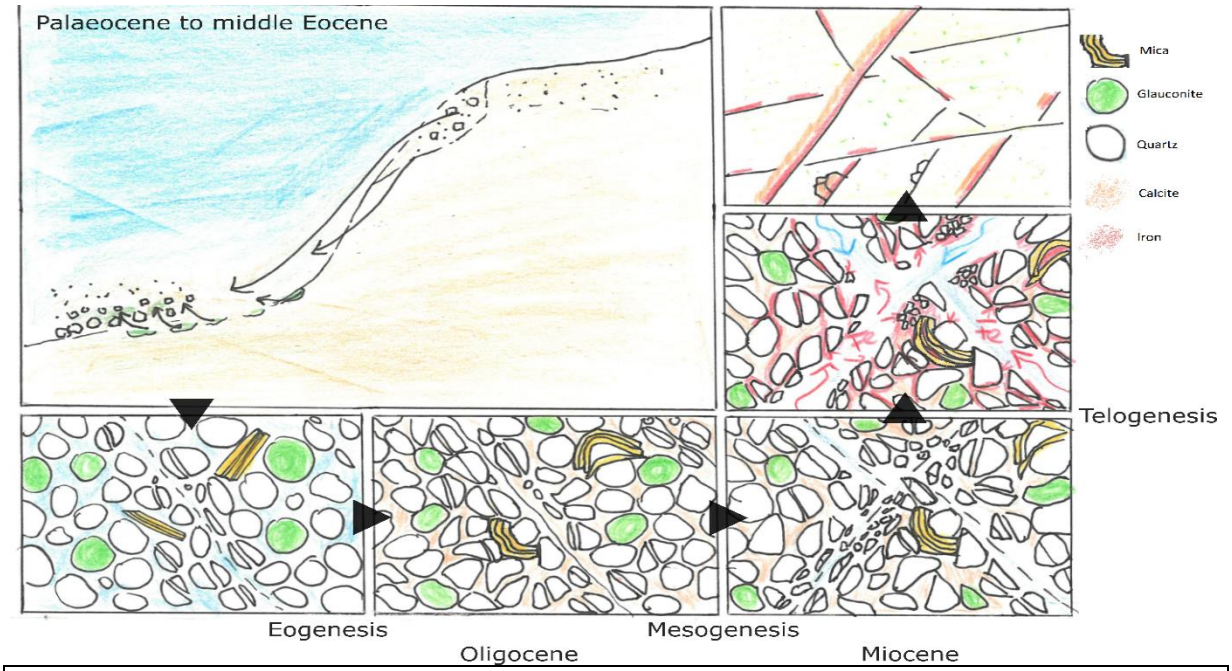

Fig. 61 Sequence of events in the sedimentation of the Greifenstein Sandstone. After burial, calcite cement developed and compaction caused bending of mica grains. Deformation led to fracturing of grains. During uplift, opening of fractures allowed fluid flow. The fluids enriched in iron came into contact with oxidizing conditions, and goethite was precipitated. Finally, calcite fibres and calcite/quartz crystals grew on fracture planes.

6. Conclusion and Prospects

The iron-red crusts on fracture surfaces within the sandstones of the quarry of the "*Strombauamt"* are poorly-crystallized, amorphous precipitates of goethite. They fill the pore space like a cement and generally reach about two millimetres into the rock.

Structural features of the sandstones and conglomerates in the quarry like deformation bands imply soft sediment deformation. Together with grain fracturing and the calcite/quartz minerals growing on fracture plains, the diagenetic and deformation history of the rock can be summarized as follows: Deposition, a first stage of soft sediment deformation, followed by burial and partial calcite cementation, uplift and aperture of fractures, permeation of iron-rich fluids coming into contact with oxidizing water. This led to goethite precipitation. Finally, calcite and quartz minerals grew on fracture planes. Internal and external sources of iron are discussed. While internal sources like glauconite and pyrite are quite unlikely because of missing evidence in the host rocks, iron-bearing minerals in the more slowly-deposited Bouma D and E sediments are considered to be good candidates for iron supply. Iron concretions around intercalations and iron-red rims around rip-ups of these sediments are a good indicator for these sediments as an iron source. It is also quite possible that the iron underwent more extensive transport from an underlying formation, but a suitable rock source linked to this phenomenon is yet to be found.

Further confirmation of this theory will require geochemical ICP-MS data to be evaluated in follow-up studies.

Permeability is reduced by the iron crust by at least 25% (from 0,035 to 0,027mD), indicating that the iron precipitates may reduce the reservoir quality of the sandstones of the Greifenstein Formation. Further investigations on this topic are definitely warranted.

7. References

Afify, A. M., Sanz-Montero, M. E., Calvo, J. P. & Wanas, H. A., 2014. Diagenetic origin of ironstone crusts in the Lower Cenomanian Bahariya Formation, Bahariya Depression, Western Desert, Egypt. *Journal of African Earth Sciences*, pp. 333-349.

Balsamo, F., Bezerra, F. H. R., Vieira, M. M. & Storti, F., 2013. Structural control on the formation of iron-oxide concretions and Liesegang bands in faulted, poorly lithifield Cenozoic sandstones of the Paraíba Basin, Brazil. *Geological Society of America Bulletin*.

Beitler, B., Parry, W. T. & Chan, M. A., 2005. Fingerprints of Fluid Flow: Chemical Diagenetic History of the Jurassic Navajo Sandstone, Southern Utah, U.S.A.. *Journal of Sedimentary Research*, pp. 547-561.

Berner, R. A., 1970. Sedimentary pyrite formation. *American Journal of Science, 268*, pp. 1-23.

Besada, A. N., 1996. *Sedimentologie der Greifensteiner Schichten im Steinbruch "Strombauamt", Höflein an der Donau (Untereozän, Rhenodanubische Flyschzone, Wienerwald),* University of Vienna: Unpublished thesis.

Boggs, S. J. & Krinsley, D., 2006. *Application of Cathodoluminescence Imaging to the Study of Sedimentary Rocks.* Cambridge: University Press.

Bouma, A. H., 1962. *Sedimentology of Some Flysch Deposits: A Graphic Approach to Facies Interpretation.* s.l.:Elsevier Publishing Company.

Bunaciu, A. A., UdriŞtioiu, E. G. & Aboul-Enein, H. Y., 2015. X-Ray Diffraction: Instrumentation and Applications. *Critical Reviews in Analytical Chemistry*, pp. 289-299.

Chan, M. A., Parry, W. T. & Bowman, J. R., 2000. Diagenetic Hematite and Manganese Oxides and Fault-Related Fluid Flow in Jurassic Sandstones, Southeastern Utah. *The American Association of Petroleum Geologists (AAPG) Bulletin*, pp. 1281-1310.

Cone, M. P. & Kersey, D. G., 1992. Porosity. In: *Development Geology Reference Manual.* Tulsa, Oklahoma, USA: The American Association of Petroleum Geologists, pp. 204-209.

Cornell, R. M. & Schwertmann, U., 1979. Influence of organic anions on the crystallization of ferrihydrite. *Clays and Clay Minerals, Vol. 27, No. 6*, pp. 402-410.

Egger, H., 1995. Die Lithostratigraphie der Altlengbach-Formation und der Anthering-Formation im Rhenodanubischen Flysch (Ostalpen, Penninikum). *Neues Jahrbuch für Geologie und Paläontologie - Abhandlungen*, 196(1), pp. 69-91.

Egger, H., 2013. Neue stratigrafische Ergebnisse aus dem Kahlenberg-Gebiet und ihre Bedeutung für die Interpretation des Deckenbaus im Wienerwald; Project: Mapping the northern rim of the Eastern Alps. *Führer zur Arbeitstagung der Geologischen Bundesanstalt 2013*, pp. 167-174.

Egger, H. et al., 1999. *Geologische Übersichtskarte der Republik Österreich.* Vienna: Geologische Bundesanstalt.

Egger, H. & Schwerd, K., 2008. Stratigraphy and sedimentation rates of Upper Cretaceous deep-water systems of the Rhenodanubian Group (Eastern Alps, Germany). *Cretaceous Research 29(3)*, pp. 405-416.

Eichhubl, P., Davatzes, N. C. & Becker, S. P., 2009. Structural and diagenetic control of fluid migration and cementation along the Moab Fault, Utah. *The American Association of Petroleum Geologists (AAPG) Bulletin*, pp. 653-681.

Eichhubl, P., Lansing Taylor, W., Pollard, D. D. & Aydin, A., 2004. Paleo-fluid flow and deformation in the Aztec Sandstone at the Valley of Fire, Nevada—Evidence for the coupling of hydrogeologic, diagenetic, and tectonic processes. *Geological Society of America Bulletin* , pp. 1120-1136.

Faupl, P., 1996. *Tiefwassersedimente und tektonischer Bau der Flyschzone des Wienerwaldes,* Wien: Exkursionsführer Sediment'96.

Fischer, W. R. & Schwertmann, U., 1975. The formation of hematite from amorphous iron(III)hydroxide. *Clays and Clay Minerals, Vol. 23*, pp. 33-37.

Folk, R. L., 1968. *Petrology of Sedimentary Rocks.* Texas: Hemphill Pub. Co.

Fossen, H., 2016. *Structural Geology.* Second Edition. Norway: Cambridge University Press.

Goldstein, J. et al., 2003. *Scanning electron microscopy and x-ray microanalysis.* Third Edition: Springer, ISBN: 978-0-306-42292-3.

Grill, R., Götzinger, G., Bachmayer, F. & Küpper, H., 1957. *Geologische Karte der Umgebung von Korneuburg und Stockerau.* Vienna: Geologische Bundesanstalt.

Heilinger, E. et al., 2006. Steinbrüche in Greifenstein. In: Marktgemeinde St. Andrä-Wördern, Hrsg. *Heimatbuch Marktgemeinde St. Andrä-Wördern, Band 1 - Geschichte.* St. Andrä-Wördern: s.n., pp. 188-191.

Heinrich, M. et al., 2008. *Ergänzende Erhebung und zusammenfassende Darstellung des geogenen Naturraumpotentials im Bezirk Tulln „Geogenes Naturraumpotential Bezirk Tulln". Bericht über die Arbeiten im 3. Projektjahr (2007-08) ,* Wien: Geologische Bundesanstalt.

Heinrich, M. et al., 2007. *Ergänzende Erhebung und zusammenfassende Darstellung des geogenen Naturraumpotentials im Bezirk Tulln „Geogenes Naturraumpotential Bezirk Tulln". Bericht über die Arbeiten im 2. Projektjahr (2006),* Wien: Geologische Bundesanstalt.

Hösch, K., 1985. *Zur lithofaziellen Entwicklung der Greifensteiner Schichten in der Flyschzone des Wienerwaldes,* University of Vienna: Unpublished thesis.

Howarth, R. W., 1979. Pyrite; its rapid formation in a salt marsh and its importance in ecosystem metabolism. *Science, 203*, pp. 49-51.

Huggett, J. M., 2013. Minerals: Glauconites and Green Clays. In: *Reference Module in Earth Systems and Environmental Sciences.* s.l.:Elsevier, pp. 1-7.

Kraal, P., Yücel, M. & Slomp, C. P., 2019. Turbidite deposition and diagenesis in the southwestern Black Sea: Implications for biogeochemical cycling in an anoxic basin. *Marine Chemistry, https://doi.org/10.1016/j.marchem.2019.01.001*.

Löffler, R., 2013. *Reservoir properties of glauconite sandstones (Greifenstein Formation) in the quarry Strombauamt,* University of Vienna: Master's thesis.

Majzlan, J. et al., 2003. Thermodynamics of Fe oxides: Part I. Entropy at standard temperature and pressure and heat capacity of goethite (a-FeOOH), lepidocrocite (y-FeOOH), and maghemite (y-Fe2O3). *American Mineralogist, Vol. 88*, pp. 846-854.

Moore, D. M. & Reynolds, R. C. J., 1997. *X-ray Diffraction and the Identification and Analysis of Clay Minerals.* New York: Oxford University Press.

Neuhuber, S., 2013. Iron crusts at the quarry Strombauamt. *Flysh Vienna Basin. Final report*.

Odin, G. S. & Matter, A., 1981. De glauconiarum origine. *Sedimentology, 28*, pp. 611-641.

Penz-Wolfmayr, M., 2018. *Comparative Porosity and Permeability Determinations of Carbonate Rocks of the Schneeberg Massif,* University of Vienna, OMV: Master's Thesis.

Pettijohn, F. J., Potter, P. E. & Siever, R., 1987. *Sand and Sandstone.* Second Edition. New York - Heidelberg - Berlin: Springer.

Potter-McIntryre, S. et al., 2013. Iron precipitation in a natural CO2 reservoir: Jurassic Navajo Sandstone in the northern San Rafael Swell, UT, USA. *Geofluids*.

Schuster, R. et al., 2013. Geologische Übersichtskarte der Republik Österreich 1:1 500 000 (ohne Quartär). In: *Rocky Austria – Geologie von Österreich – kurz und bunt.* Vienna: Geologische Bundesanstalt, p. 80.

Schwertmann, U. & Taylor, R. M., 1989. Iron oxides. In: *Minerals in soil environments.* Madison, WI: Soil Science Society of America, pp. 379-438.

Shogenova, A. et al., 2009. Composition and properties of the iron hydroxides-cemented lenses in Estonian sandstone of Middle Devonian age. *Studia Geophysica et Geodaetica*, pp. 111-131.

Trautwein, B., Dunkl, I. & Frisch, W., 2001. Accretionary history of the Rhenodanubian flysh zone in the Eastern Alps - evidence from apatite fission-track geochronology. *International Journal of Earth Sciences*, pp. 703-713.

Walker, R. G., 1978. Deep-Water Sandstone Facies and Ancient Submarine Fans: Models for Exploration for Stratigraphic Traps. *AAPG Bulletin 62(5)*, pp. 239-263.

Walker, T. R., 1975. Red beds in the western interior of the United States. *U.S. Geological Survey Professional Paper No. 853, part II*, pp. 49-56.

Wessely, G., 2006. *Geologie der Österreichischen Bundesländer – Niederösterreich.* ISBN 3-85316-23-9 ed. Vienna: Geologische Bundesanstalt.

Worden, R. H. & Burley, S. D., 2003. Sandstone diagenesis: the evolution of sand to stone. In: *Sandstone Diagenesis: Recent and Ancient. International Association of Sedimentologists Reprint Series.* UK: s.n., pp. 3-44.

Worden, R. H., Mayall, M. & Evans, I. J., 2000. The Effect of Ductile-Lithic Sand Grains and Quartz Cement on Porosity and Permeability in Oligocene and Lower Miocene Clastics, South China Sea: Prediction of Reservoir Quality. *AAPG Bulletin,*, Issue V. 84, No. 3, pp. 345-359.

Worden, R. H. & Morad, S., 2003. Clay minerals in sandstones: controls on formation, distribution and evolution. *Int. Assoc. Sedimentol. Spec. Publ.*, Issue 34, pp. 3-41.

Zhang, X. et al., 2017. An experimental study on transforming montmorillonite to glauconite: implications for the process of glauconitization. *Clays and Clay Minerals*.

ADDENDUM

Addendum/Appendix

Table 3: List of the samples, their position and how they were investigated

[m]…approximate height in profile of Besada (1996) (cf. Fig. 4, Appendix)

Sample No.	Lithology	[m]	Method
M1	Sandstone	100	TLM, SEM, EDX, Poroperm, EMP, CL
M2	Sandstone	103	TLM,
M3	Sandstone	103	TLM, SEM
M4	Sandstone	95	TLM, SEM
M5	Sandstone	103	XRD (white precipitates)
M6	Iron Crust (M7)	103,5	ICP-MS
M7	Sandstone	103,5	ICP-MS
M8	Sandstone	102	TLM; XRD and ICP-MS
M9	Iron Crust (M10)	80	XRD and ICP-MS
M10	Conglomerate	80	TLM, XRD and ICP-MS
M11	Sandstone	25	ICP-MS
M12	Conglomerate	25	-
M13	Iron Concretion	25	XRD and ICP-MS
M14	Clay	25	ICP-MS
M15	Conglomerate	25	-
M16	Conglomerate	25	XRD and ICP-MS
M17	Conglomerate	22	-
M18	Rip-up clast	19	ICP-MS
M19	Conglomerate	no bedrock	-
M20	Conglomerate	20	ICP-MS
M21	Conglomerate	no bedrock	-
M22	Sandstone	no bedrock	XRD and ICP-MS
M23	Sandstone	no bedrock	ICP-MS
M24	Sandstone	18	XRD and ICP-MS
M25	Iron Crust (M26)	no bedrock	XRD and ICP-MS
M26	Sandstone	no bedrock	XRD and ICP-MS

Table 4: Designations of thin sections and plugs

Thin section No.	Plug No.
Gr1a_I & Gr1a_II: (152/68), Gr1b_I & Gr1b_II: (152/68) Gr1c_I, Gr1c_II: (319/49)	GS1, GS2, GS3
M2	-
M3	-
M4-1, M4-2A, M4-2B, M4-2C	-
M8	-
M10	-

Sample pictures and description:

M1

Light to medium grey, finely-grained sandstone with a number of 1-2mm large clasts (clay, glauconite, quartz or glimmer) Iron crusts on 3 (354/71, P 146/35 L 186/33), P 152/68 L 329/25) sides of the sample, with one cutting through the sample (319/49); calcite fibres on two sides (P 152/68 L 329/25, P 260/72 L 186/05) P… Plane, L… Linear	

M2

Light grey to medium grey sandstone, a little bit lighter than M1, finely-grained, very rare clay clasts of up to 4mm size, calcite fibre on side 260/74, iron crust with calcite fibres on the backside	

M3

Light grey to medium grey sandstone, finely-grained, thin iron crust on one side	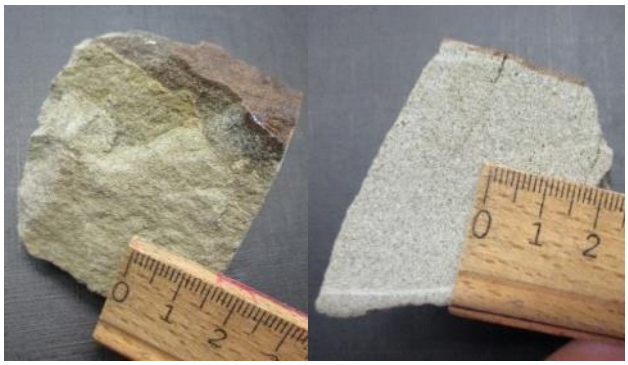

M4

Medium grey, bluish sandstone. Iron crusts on 4 planes	

M5

Light grey to medium grey sandstone, finely-grained, correlates with M3 (same bed), odd white crystalline powder on the surface.	

M6

Iron concretion that was on the sandstone M7, 1-2 mm thick, dark red	

M7

Light grey, finely-grained, iron-crusted sandstone. Iron crust matches sample M6	

M8

Light grey, finely-grained, iron-crusted sandstone. Iron mineral diffuses up to 4.5cm into the sandstone where it ends with a 0.5-1mm thick dark red margin.	

M9

Iron crust from M10, up to 2mm thick.	

M10

Conglomerate, matrix-dominated, clasts of quartz, clay and other minerals 1-4 mm in size, poorly-sorted, iron-crusted.	

M11

Greenish – grey conglomerate/sandstone, 2-3mm clasts, clay on one side. Material from a rip-up clast (whole sediment-layer ripped up) in between the bed at around metre 25	

M12

Ochre to light grey, finely-grained conglomerate, matrix dominated, clasts up to 8 mm, correlates with M15 & M16 (same bed as M11 above: metre 25)	

M13

Iron concretion (clay): light to dark red, smooth surface, core sandier/siltier and light red, margin dark red. Material from a rip-up clast (whole sediment-layer ripped up) in between bed at around metre 25	

M14

Dark grey, reddish, weathered clay Material from a rip-up clast (whole sediment-layer ripped up) in between the bed at around metre 25	

M15

Ochre to light grey, finely-grained conglomerate, matrix dominated, correlates with M12 & M16 (same bed), with iron-oxide vein and bound to sediment layer in between with samples M11, M13, M14	

M16

Ochre to light grey conglomerate, matrix-dominated, clasts up to 12 mm, correlates with M12 & M15 (same bed)	

M17

Ochre to light grey, medium-grained conglomerate, more clast-supported, clasts (mostly quartz) up to 12 mm.	

M18

Clayey, silty material from a rip-up clast, green-grey.	

M19

Conglomerate pieces, clasts with up to 7 mm, with a dark grey crust.	

M20

Conglomerate, more finely-grained, clasts up to 3 mm, some larger rip-up clasts	

M21

Conglomerate, more coarsely-grained, not as matrix-dominated as the others, most clasts around 5mm, but also clasts up to 13 mm, one big rip-up clast with a red crust, second smaller rip-up, only margin is preserved (black), clasts: quartz, clay, mica, carbonate, iron-rich clay; no bedrock	

M22

Sandstone, finely-grained, greenish-grey, trace fossil on the surface, bitumen/clay vein, clay clast, surface brownish-green with aforementioned fossil on it.	

M23

Light grey to greenish sandstone, most finely-grained	

M24

Very green to brownish (iron), weathered sandstone, trace fossils on the surface, finely-grained, From rip-up clast with drainage structures	

M25

Crust that belongs to M26, up to 7 mm thick, no bedrock	

M26

Finely-grained sandstone, light grey, reddish, no bedrock	See M25

Table 5 Microprobe data.

DataSet/Point	Na2O	MgO	SiO2	Al2O3	K2O	CaO	FeO	TiO2	MnO	BaO	SrO	CO2	Cr2O3	V2O3	ZnO	NiO	PbO	Total	X	Y	Z	Comment	Distance (µ)	Date
1 / 1 .	0	0,2667	0,0154	0,0225	0,0152	55,2126	1,0216	0	0,0972	0,0304	0,3697	42,9487						100	-5468	-18397	99	Gr1A_II_FaserCC		25.07.2018 11:35
2 / 1 .	0	0,2408	0,0291	0,0024	0,0051	55,0545	0,9387	0	0,0992	0,0382	0,3766	43,2154						100	-5421	-18410	99	Gr1A_II_FaserCC		25.07.2018 11:38
3 / 1 .	0	0,1749	0,0053	0,0101	0	55,413	0,9313	0	0,0701	0,0526	0,6149	42,7277						100	-9467	-18824	99	Gr1A_II_FaserCC		25.07.2018 11:42
4 / 1 .	0,005	0,3793	0,0029	0	0,0037	56,2365	1,5836	0,0096	0,1811	0	0,0988	41,4994						100	-9414	-28616	99	Gr1A_II_CC_Zement		25.07.2018 11:45
5 / 1 .	0,0282	0,3757	0,0854	0,0054	0,0022	54,8157	1,6642	0,013	0,1459	0,0099	0,0957	42,7587						100	-8613	-28033	99	Gr1A_II_CC_Zement		25.07.2018 11:48
6 / 1 .	0	0,3575	0,0031	0,0172	0,0098	56,5471	1,713	0	0,1691	0	0,0822	41,1011						100	-6562	-28090	99	Gr1A_II_CC_Zement		25.07.2018 11:51
7 / 1 .	0,0167	0,4036	0,008	0	0,0424	54,4456	1,8505	0,0013	0,171	0,0056	0,0163	43,0389						100	-5900	-28427	99	Gr1A_II_CC_Zement		25.07.2018 11:54
8 / 1 .	0,0621	4,0312	50,9354	11,3833	8,4281	0,1964	18,4024	0,085	0				0,0741	0,0575	0,004	0,015	0	93,6476	-6910	-19487	103	Gr1A_II_Glaukonit gruen Kruste		25.07.2018 13:43
9 / 1 .	0,0433	4,5312	52,4682	9,9052	9,1002	0,1428	16,9814	0,0855	0				0,0689	0,0344	0,0032	0	0	93,3436	-7489	-20066	101	Gr1A_II_Glaukonit gruen Kruste		25.07.2018 13:49
10 / 1 .	0,0449	4,1746	50,9007	9,5281	9,1792	0,1244	18,2929	0,0169	0,0035				0,0736	0,0315	0,0123	0,0013	0,0174	92,4013	5103	-18416	104	Gr1A_II_Glaukonit gruen Kruste		25.07.2018 13:54
11 / 1 .	0,0256	4,2468	52,3358	9,7859	8,6032	0,2944	17,7992	0,0298	0				0,074	0,0555	0,004	0	0,0227	93,2531	433	-26354	103	Gr1A_II_Glaukonit gruen host		25.07.2018 13:59
12 / 1 .	0,0314	4,1993	51,3916	7,8225	8,888	0,2126	19,7958	0,02	0				0,0731	0,0239	0,0011	0	0,0087	92,4354	9163	-22896	103	Gr1A_II_Glaukonit gruen host		25.07.2018 14:04
13 / 1 .	0,0408	4,0983	50,7085	9,2739	7,7209	0,364	19,0913	0,2117	0				0,0224	0,0422	0	0	0	91,5341	9539	-29661	98	Gr1A_II_Glaukonit gruen host		25.07.2018 14:10
14 / 1 .	0,0011	0,3848	4,1833	0,7777	0,0108	0,5738	72,2007	0,0164	0,0244				0	0	0,0268	0	0	78,1512	-7764	-20050	103	Gr1A_II_Fe_oxid_zement		25.07.2018 13:04
15 / 1 .	0,0053	0,3939	3,6239	0,1121	0,0068	1,0955	72,4288	0	0,0632				0	0,01	0,057	0,01	0,0204	77,8073	-7716	-19952	103	Gr1A_II_Fe_oxid_zement		25.07.2018 13:14
16 / 1 .	0,0124	0,391	4,1335	0,4678	0,1144	0,6115	69,7501	0	0,0783				0,0007	0,0151	0,0247	0	0,0386	75,5999	-6947	-20009	103	Gr1A_II_Fe_oxid_zement		25.07.2018 13:22
17 / 1 .	0,0385	0,3881	4,1961	0,2241	0,0908	0,4636	72,1319	0,003	0,0244				0	0	0,076	0	0,031	77,6154	-6249	-20422	103	Gr1A_II_Fe_oxid_Korn_Kruste		25.07.2018 13:33
18 / 1 .	0,0511	4,0798	51,5907	11,167	8,4983	0,1742	18,4857	0,0769	0				0,0755	0,0657	0,0145	0,0068	0,0054	94,2913	-6911	-19487	103	Gr1A_II_Glaukonit gruen Kruste_near pt8		25.07.2018 14:25
19 / 1 .	0,0041	0,311	0,0158	0,0004	0	57,8666	1,5415	0	0,1165	0,0434	0,53	39,5706						100	-11488	17893	120	M2_FaserCC (Line) Pt 1		25.07.2018 14:56
20 / 1 .	0,0062	0,0719	0,0281	0,0024	0,0044	58,8398	0,3469	0	0,0251	0,0529	0,5836	40,0388						100	-11490	17544	120	M2_FaserCC (Line) Pt 2		25.07.2018 14:59
21 / 1 .	0,0016	0,1176	0,0152	0,0137	0,0053	57,8338	0,6118	0,001	0,0517	0	0,275	41,0732						100	-11489	17204	120	M2_FaserCC (Line) Pt 3		25.07.2018 15:03
22 / 1 .	0	0,1927	0,0235	0	0,0157	58,8128	0,8136	0	0,067	0,026	0,2797	39,7691						100	-11496	16859	120	M2_FaserCC (Line) Pt 4		25.07.2018 15:06
23 / 1 .	0	0,3071	0,0142	0,0073	0,0044	57,4539	1,6137	0,0251	0,1512	0,1242	0,5698	39,7293						100	5131	17835	95	M2_FaserCC line2 (Line) Pt 1		25.07.2018 15:09
24 / 1 .	0	0,2173	0,0121	0,0056	0,0018	56,6569	0,9865	0,0023	0,0869	0,0171	0,4202	41,5933						100	5131	17446	95	M2_FaserCC line2 (Line) Pt 2		25.07.2018 15:12
25 / 1 .	0,0131	0,2689	0,0164	0,012	0,0142	57,4893	0,9403	0	0,0732	0	0,4477	40,725						100	5143	17048	95	M2_FaserCC line2 (Line) Pt 3		25.07.2018 15:15
26 / 1 .	0	0,2332	0,0202	0	0,0048	54,7993	1,1375	0,0199	0,1124	0,0953	0,5142	43,0632						100	5160	16669	95	M2_FaserCC line2 (Line) Pt 4		25.07.2018 15:19
27 / 1 .	0,0058	0,4346	0,0309	0,0002	0	56,8386	1,3799	0,0161	0,3266	0	0,0912	40,8761						100	3926	24253	106	M2_CC_Zement		25.07.2018 15:22
28 / 1 .	0	0,3017	0,0341	0,0044	0	56,7975	1,3896	0,0075	0,2396	0	0,2593	40,9661						100	6362	23001	102	M2_CC_Zement		25.07.2018 15:25
29 / 1 .	0	0,0784	0,0723	0,0047	0,0321	57,1673	0,529	0	0,0355	0	0,3254	41,7553						100	7113	22764	102	M2_CC_Zement		25.07.2018 15:28
30 / 1 .	0	0,3586	0,0484	0,01	0,0314	57,4494	1,7257	0	0,3219	0,0578	0,2757	39,721						100	7332	22181	100	M2_CC_Zement		25.07.2018 15:32
31 / 1 .	0,0373	0,4674	0,0405	0,0132	0,0115	58,4064	0,1433	0,0025	0,0039	0	0,1067	40,7673						100	6406	21593	100	M2_CC_Zement		25.07.2018 15:35
32 / 1 .	0,0187	0,341	0,0582	0,0096	0,0056	56,7693	1,3375	0	0,1946	0,0334	0,2034	41,0287						100	7798	19146	100	M2_CC_Zement		25.07.2018 15:38

DataSet/Point	Na2O	SiO2	MgO	Al2O3	K2O	CaO	FeO	TiO2	Cr2O3	V2O3	ZnO	NiO	PbO	MnO	P2O5	CO2	Total	X	Y	Z	Comment	Distance (µ)	Date
1 / 1 .	0,012	3,336	1,3867	0,5244	0,022	0,7908	68,8526	0,0344	0,0048	0,0417	0,0573	0	0,0186	0,0671	0,5335		75,6818	3833	15254	89	M4_2B_oxidierter Bereich_Aggregat		25.07.2018 16:38
2 / 1 .	0,0284	2,7844	0,3451	0,4873	0,0114	0,2679	74,7579	0,0251	0,016	0,0624	0,0378	0	0,0511	0,0815	0,2929		79,2492	4101	17299	89	M4_2B_oxidierter Bereich_Aggregat		25.07.2018 16:44
3 / 1 .	0,0554	2,6638	0,5387	0,7395	0,0104	1,1678	71,5324	0,005	0,01	0,1215	0,0499	0	0,0217	0,0808	0,5713		77,5683	5217	17392	89	M4_2B_oxidierter Bereich_Aggregat		25.07.2018 16:53
4 / 1 .	0,0684	0,0533	5,336	0,0076	0,0278	9,4669	42,6309	0	0,001	0,0451	0,0375	0,0131	0,0382	0,0438	0,2885	41,942	100	2509	24397	104	M4_2B_host_Aggregat		25.07.2018 17:08
5 / 1 .	0,0708	0,0963	5,2579	0,0124	0,0457	7,3676	43,8184	0,0142	0	0	0,0211	0,0174	0,0405	1,6209	0,0989	41,5178	100	2456	24483	104	M4_2B_host_Aggregat		25.07.2018 17:13
6 / 1 .	0,0714	0,1395	5,2997	0,0728	0,0439	7,6665	44,1354	0,0136	0	0,0139	0,0193	0,0278	0,0415	1,6347	0,1147	40,705	100	12635	28214	84	M4_2B_host_Aggregat		25.07.2018 17:19
7 / 1 .	0,043	0,1197	5,6059	0,0326	0,0041	7,7959	42,7755	0	0	0	0,0392	0,0114	0,0106	1,5445	0,0787	41,939	100	1893	24302	104	M4_2B_host_Aggregat		25.07.2018 17:32
8 / 1 .	0,0829	0,0249	4,6671	0,0136	0,0082	8,2473	44,075	0,0246	0	0,0043	0,0051	0	0,0071	0,8696	0,1643	41,8059	100	1945	24173	104	M4_2B_host_Aggregat		25.07.2018 17:37
9 / 1 .	0	2,644	0,3934	1,0257	0,014	0,8839	71,915	0,0124	0,0166	0,0709	0,0469	0	0	0,0966	0,319		77,4385	-7026	-28074	108	M4_1_oxidierter Bereich_Aggregat		25.07.2018 17:59
10 / 1 .	0	2,3713	0,4973	1,6361	0,0354	0,4414	70,718	0,0376	0,0351	0,1893	0,0973	0	0,0362	0,084	0,6155		76,7945	-6925	-27801	108	M4_1_oxidierter Bereich_Aggregat		25.07.2018 18:04
11 / 1 .	0	2,3937	0,4237	1,2438	0,0327	0,5889	70,9712	0,0478	0,0318	0,2088	0,0468	0	0,0345	0,0983	0,4431		76,5654	-9650	-30230	108	M4_1_oxidierter Bereich_Aggregat		25.07.2018 18:09
12 / 1 .	0	2,744	0,436	0,3809	0,0106	0,7612	70,8128	0,0103	0,0056	0,0593	0,0547	0	0,0238	0,1688	0,29		75,758	-9905	-30624	108	M4_1_oxidierter Bereich_Aggregat		25.07.2018 18:15
13 / 1 .	0,0219	3,036	0,4529	1,0397	0,0121	0,5267	70,5543	0,0092	0,0167	0,0864	0,0239	0,0126	0,0524	0,1049	0,3613		76,311	-11130	-31800	108	M4_1_oxidierter Bereich_Aggregat		25.07.2018 18:20
14 / 1 .	0,0003	6,6895	1,542	4,3401	0,4932	0,7186	64,2531	0,129	0,0256	0,0584	0,0824	0,0174	0,0233	0,0782	0,216		78,6671	-9173	-23539	108	M4_1_oxidierter Bereich hell_Aggregat		25.07.2018 18:25
15 / 1 .	0	3,1932	1,3872	1,8231	0,0188	1,4363	73,0386	0,0282	0,017	0,0485	0,0943	0	0,0624	0,096	0,2775		81,5213	-9097	-23623	108	M4_1_oxidierter Bereich hell_Aggregat		25.07.2018 18:30
16 / 1 .	0,0099	3,1805	1,4153	1,3163	0,002	1,446	71,8559	0	0,0306	0,0573	0,1129	0	0,0374	0,1765	0,264		79,9046	-9483	-24259	108	M4_1_oxidierter Bereich hell_Aggregat		25.07.2018 18:36
17 / 1 .	0,0367	0,2303	5,8147	0,0887	0,0526	7,6167	43,7016	0,021	0,0104	0,0101	0,0617	0	0	0,3244	0,1559	41,8752	100	-333	-36808	108	M4_1_host_Aggregat		25.07.2018 18:41
18 / 1 .	0,0537	0,0359	5,4923	0,0028	0,0392	7,7871	43,366	0	0	0	0,032	0	0,0301	1,6842	0,0685	41,4083	100	-153	-36629	108	M4_1_host_Aggregat		25.07.2018 18:46
19 / 1 .	0,0476	0,0478	6,2176	0,0129	0,0082	7,7478	44,0176	0	0	0,0092	0,0482	0	0,0226	0,7889	0,1384	40,8932	100	-355	-36177	108	M4_1_host_Aggregat		25.07.2018 18:52
20 / 1 .	0,0482	0,0683	6,0795	0,0212	0,0575	7,0652	43,4036	0,0746	0,0056	0,0174	0,0725	0	0,0365	1,3929	0,0471	41,6098	100	-79	-36309	108	M4_1_host_Aggregat		25.07.2018 18:57

Table 6 Measurements in the field

	Plane	Linear	Comment	Samples
09.07.2017	139/41	174/38	Location in the quarry	M1
09.07.2017	354/71			M1
09.07.2017	146/35	186/33	Normal fault	M1
09.07.2017	152/68	329/25	Cuts through rock	M1, Plug GS3
09.07.2017	319/49			M1, Plug GS1; GS2 normal darauf
09.07.2017	260/72	186/05		M1
13.10.2017	030/58		Joint plane	
13.10.2017	093/90		Joint plane	
13.10.2017	008/55		Joint plane	
13.10.2017	107/79	197/14	With riedel shears	
13.10.2017	107/79	192/10	With riedel shears	
13.10.2017	044/61			
13.10.2017	066/56		Hacklemarks	
13.10.2017	065/57		Hacklemarks	
13.10.2017	001/73	078/24	lin on crust, on top of it idiomorphic qtz	
13.10.2017	356/72			
13.10.2017	103/85	191/12	sin 2R crust linear	
13.10.2017	100/75	188/09		
13.10.2017	082/73			
13.10.2017	074/66		Main plane, splits in Hacklemarks	
13.10.2017	044/61		Hacklemarks	
13.10.2017	066/56		Hacklemarks	
13.10.2017	065/57		Hacklemarks	
13.10.2017	357/74			
13.10.2017	076/79			
13.10.2017	352/76			
13.10.2017	244/84			
13.10.2017	093/77			
13.10.2017	100/78			
13.10.2017	094/61	002/02		
13.10.2017	368/70		Crust very thin	
13.10.2017	244/84		Joint plane	

13.10.2017	351/54		Joint plane	
13.10.2017	359/54		Joint plane	
13.10.2017	059/14	065/11	horizontal	
13.10.2017	063/89		eastern	M4
13.10.2017	143/42		Bedding plane	
13.10.2017	121/34		Bedding plane	
13.10.2017	117/43		Bedding plane	
13.10.2017	115/24		Bedding plane	
13.10.2017	312/57		No crust, joint planes	
13.10.2017	315/58		No crust, joint planes	
13.10.2017	314/53		No crust, joint planes	
13.10.2017	310/60		No crust, joint planes	
13.10.2017	026/74		No crust, joint planes	
13.10.2017	199/79		No crust, joint planes	
13.10.2017	210/78		No crust, joint planes	
13.10.2017	153/21		Bedding plane	
13.10.2017	148/17		Bedding plane	
13.10.2017	091/30		Bedding plane	
13.10.2017	136/18		Bedding plane	
13.10.2017	094/31		Bedding plane	
13.10.2017	351/66		Encrusted plane	
13.10.2017	341/66		Encrusted plane	
13.10.2017	354/68		Fe-Crusts	
13.10.2017	350/62		Fe-Crusts	
13.10.2017	344/69		Fe-Crusts	
13.10.2017	336/70		Fe-Crusts	
13.10.2017	287/68		Fe-Crusts	
13.10.2017	351/71		Fe-Crusts	
13.10.2017	112/19		Bedding plane	
13.10.2017	201/60	261/32	Fe-Crusts, crust cc-overgrown	
13.10.2017	127/24		Bedding plane	
13.10.2017	214/59	259/45	Fe-Crusts	
13.10.2017	113/19		Bedding plane	
13.10.2017	056/81		Fe-Crusts + CC	
13.10.2017	294/78	256/77	hf no crust	
13.10.2017	281/60			
13.10.2017	280/51			
13.10.2017	094/31		Bedding plane	
13.10.2017	122/88			
13.10.2017	099/80			
13.10.2017	258/69			
13.10.2017	260/74			M2
13.10.2017	117/76			
13.10.2017	351/71			M3

13.10.2017	082/72			
13.10.2017	106/22			
13.10.2017	107/76			
13.10.2017	290/66			
13.10.2017	304/61			
13.10.2017	136/18		Bedding plane	
13.10.2017	148/17		Bedding plane	
13.10.2017	257/75		conj. normal fault	
13.10.2017	281/60		conj. normal fault	
13.10.2017	116/79		conj. normal fault	
13.10.2017	007/58		fracs with Fe crust, cut by conj. faults	
13.10.2017	001/80		fracs with Fe crust, cut by conj. faults	
13.10.2017	355/72		fracs with Fe crust, cut by conj. faults	
13.10.2017	038/73		fracs with Fe crust	
13.10.2017	041/80		fracs with Fe crust	
13.10.2017	013/72		fracs with Fe crust	
08.02.2018	260/74		Thin section M2 long line	
08.02.2018	342/90		Thin section M2 short line	
08.02.2018	063/89		Thin section M4-1 long line	
08.02.2018	338/85		Thin section M4-1 short line	
08.02.2018	336/84		Thin section M4-1 short line	
08.02.2018	338/84		Thin section M4-1 short line	
08.02.2018	063/89		Thin section M4-2B long line	
08.02.2018	161/86		Thin section M4-2B short line	
08.02.2018	158/85		Thin section M4-2B short line	
08.02.2018	165/87		Thin section M4-2B short line	
08.02.2018	000/17		Thin section M4-2C long line	
08.02.2018	356/19		Thin section M4-2C long line	
08.02.2018	351/20		Thin section M4-2C long line	
08.02.2018	358/13		Thin section M4-2C long line	
08.02.2018	358/10		Thin section M4-2C long line	
08.02.2018	350/12		Thin section M4-2C long line	
08.02.2018	063/89		Thin section M4-2C short line	
16.02.2018	152/68		plane 3 of sample	
16.02.2018	319/49		plane 4 of sample	
19.06.2018	135/23		Bedding plane	
19.06.2018	135/25		Bedding plane	
19.06.2018	342/75		Joint plane with crust	
19.06.2018	064/80	335/18	Fault plane with CC	
19.06.2018	350/50		Fe-crust	
19.06.2018	171/88		Fe-crust	
19.06.2018	216/80		Joint plane with crust	

19.06.2018	032/89		Joint plane with crust	
19.06.2018	028/90		Joint plane with crust	
19.06.2018	050/85		Joint plane with crust	
19.06.2018	002/69		Joint plane with crust	
19.06.2018	145/17		Bedding plane	
19.06.2018	146/25		Bedding plane	
19.06.2018	342/48		Joint plane with crust	
19.06.2018	226/84		Joint plane with crust and CC	
19.06.2018	129/25		Bedding plane with Fe crust	
19.06.2018	128/25		Bedding plane with Fe crust	
19.10.2018	108/84			
19.10.2018	273/79			
19.10.2018	110/74			
19.10.2018	265/69		Thin crust	
19.10.2018	108/83		Joint plane with crust and CC	
19.10.2018	282/85			
19.10.2018	118/79			
19.10.2018	262/61			
19.10.2018	268/80			
19.10.2018	116/89	024/22	Joint plane with crust and CC	
19.10.2018	089/74			
19.10.2018	113/68			
19.10.2018	359/81			
19.10.2018	009/71			
19.10.2018	013/74			
19.10.2018	017/73			
19.10.2018	156/26		Bedding (at SSD)	
19.10.2018	348/64		Crust	M8
19.10.2018	318/70		Crust	M9, M10
19.10.2018	326/64		Crust	
19.10.2018	315/64		Crust	
19.10.2018	330/81		Crust	
19.10.2018	326/79		Crust	
19.10.2018	316/60		Crust	
19.10.2018	313/71		Crust	
19.10.2018	313/66		Crust	
19.10.2018	317/69		Crust	
19.10.2018	310/71		Crust	
19.10.2018	312/60		Crust	
19.10.2018	317/68		Crust	
19.10.2018	217/80		Joint plane with crust and CC	
19.10.2018	356/51		Conglomerate – faults?	M11-M16
19.10.2018	340/58		Conglomerate – faults?	M11-M16
19.10.2018	353/29		Fe-Vein, that extends from conglomerate	M15

19.10.2018	136/84		Water escape/deformation bands	M24
19.10.2018	342/61		Water escape/deformation bands	
19.10.2018	320/41		Water escape/deformation bands	
20.05.2019	022/83	299/15	Water escape/deformation bands	M24
21.05.2019	330/63		Fault „Mürbsandstein“/Conglomerate	
22.05.2019	299/83		Thin Fe crust on conglomerate	
23.05.2019	284/79		Thin Fe crust on conglomerate	
24.05.2019	309/64		Thin Fe crust on conglomerate	
25.05.2019	291/59		Thin Fe crust on conglomerate	

DEUTSCHER ABSTRACT/ABSTRACT ZUSAMMENFASSUNG

Im Steinbruch „Strombauamt“ in Greifenstein, Niederösterreich, treten „Eisenkrusten“ auf Kluftflächen in den massiven Sandsteinbänken auf. Die Mineralogie, die chemische Zusammensetzung und (Mikro-)Strukturen wurden analysiert, um den Ursprung und den Bildungsmechanismus dieser Krusten zu bestimmen. Bänke mit Eisenkrusten bestehen aus bis zu 10 m mächtigen, massiven Sandsteinen einer Turbiditabfolge. Der Sandstein gehört zur Greifenstein-Formation der Rhenodanubischen Flysch-Zone und wurde während des oberen Paläozäns bis zum unteren Eozän abgelagert. Da diese Sandsteine Aufschlussanaloga von Reservoirgesteinen im Untergrund des Wiener Beckens sind, wurde der Effekt der Eisenkrusten auf die Verringerung ihrer Permeabilität untersucht.

Die Eisenbeläge sind auf der ca. 250 m langen, E-W-verlaufenden Südwand des Steinbruchs zu finden. Dort bedecken die roten bis orangefarbenen Krusten die Kluftflächen der dickbankigen (1 m - 10 m) Sandsteine im Liegenden, setzen sich jedoch nicht in den hangenden, dünnbankigen Sandsteinen fort. Gelegentlich ist die Kruste von synkinematischen Calcitfasern überwachsen, die sich auf Störungsflächen gebildet haben, noch seltener von idiomorphen Calcit- oder Quarz-Kristallen. Soft-Sedimentstrukturen deuten darauf hin, dass zumindest ein Teil der Eisen-Ausfällungen auf Deformationsbändern entstanden ist, die sich erst kurz nach der Sedimentablagerung in noch nicht lithifizierten Ablagerungen bilden. Die Gesteine des Steinbruchs sind stark zerklüftet. Bei Messungen haben sich 4 Kluftscharen herauskristallisiert, von denen alle Eisenkrusten führen.

Die Sandsteine sind als glaukonitreiche Quarzarenite zu klassifizieren, die meist mit Calcit zementiert sind. Röntgendiffraktometrie zur Bestimmung der mineralogischen Zusammensetzung der Kruste identifizierte hauptsächlich Quarz, K-Feldspat, Calcit, Muskovit, Glaukonit und Spuren von Goethit als Beweis für ein Eisenmineral, das eine Kruste bildet. Die Eisenbeschichtung ragt ca. 0,5 mm bis 5 mm in den Sandstein hinein und bildet makroskopisch eine rote Kruste. REM-Mikroskopie in Kombination mit EDX zeigt, dass das Eisenmineral ein Eisenoxid ist, das wie ein Zement die Porenräume des Gesteins füllt. Zerbrochene Körner, die später durch das Eisenoxid zementiert wurden, geben Hinweise auf tektonische Vorgänge.

Mit den vorliegenden Ergebnissen schlagen wir vor, dass eisenreiche Fluide, die durch die Klüfte im Sediment drangen, die Ausfällung von Eisenoxid an Korngrenzen induzierten, möglicherweise zweimal. Einige dieser Klüfte wurden später mit sekundärem Calcit gefüllt, was auf eine Scherung entlang dieser hinweist. Die Eisenquelle kann entweder extern oder intern, also vom Sandstein selbst, sein. Obwohl der Sandstein reichlich Glaukonit und ein wenig Pyrit enthält, ist eine externe Quelle wahrscheinlicher. Im Südwesten des Steinbruchs

sind im Liegenden der Sandsteine Konglomerate aufgeschlossen, die reichlich Rip-Up-Klasten und Reste von großteils erodierten Zwischenlagen von feinkörnigem glaukonit- und eisenreichem Sediment enthalten. Dieses ist meist von einer eisenroten Kruste und teils sogar Eisenkonkretionen begrenzt. Das macht sie zu guten Kandidaten als Eisenquelle. Eine andere externe Quelle, wie eisenhaltige Minerale einer tiefer liegenden Formation, wird jedoch ebenfalls als wahrscheinlich angesehen.